UNIVERSITY OF CALIFORNIA

Santa Barbara

A Comparative Morphologic Analysis of Hydrocarbon Induced Terrains in the Gulf of Mexico and Offshore Southern California

A Thesis submitted in partial satisfaction of the

requirements for the degree Master of Science

in Earth Science

by

Justin Salomon Tran

Committee in charge:

Professor David Valentine, Chair

Professor Kristin Morell

Professor Libe Washburn

September 2018

The thesis of Justin Tran is approved.

_____

Libe Washburn

_____

Kristin Morell

_____

David Valentine, Committee Chair

September 2018

ACKNOWLEDGEMENTS

Dave Valentine and Burch Fisher were valuable mentors throughout this study. Dave Valentine conceived the project and his expertise and resources was extremely beneficial. Burch Fisher provided impactful guidance throughout the analysis.

I would like to thank Libe Washburn and Kristin Morell for agreeing to serve on my committee on short notice. I would also like to thank the Naval Oceanographic Office for sponsoring my education. This work would not have been possible without these parties.

Lastly, my family provided unwavering support and motivation throughout and I would not be in this position if not for them.

ABSTRACT

A Comparative Morphologic Analysis of Hydrocarbon Induced Terrains in the Gulf of Mexico and Offshore Southern California

by

Justin Salomon Tran

Hydrocarbons, such as methane or oil, flow to the seafloor from subsurface reservoirs and can induce elevated or depressed bathymetric terrains. They can harbor poorly understood life and induce mass wasting or slumping. Identification of hydrocarbon source and seepage activity is a nested process, involving a combination of multibeam surveys, seismic surveys, and direct observations. Classification of terrains induced by different hydrocarbon source based on bathymetric signatures has not yet been attempted in the literature. In this study, geomorphic analysis is conducted on high-resolution bathymetric data, collected by the autonomous underwater vehicle (AUV) Sentry, of hydrocarbon induced terrains formed by various sources offshore Southern California and in the Gulf of Mexico. Analyses of elevated hydrocarbon induced terrains sourced from gas hydrate, mud, and oil suggest that different phases of hydrocarbons may produce detectable scale-dependent geomorphic and hypsometric signatures. Actively seeping depressed hydrocarbon induced terrains, or pockmarks, may be characterized by a higher number of large coalesced and small unit pockmarks when compared to dormant terrains. The quantitative classification of hydrocarbon induced terrains by source or activity shown here suggest that bathymetric

signatures may be representative of hydrocarbon seepage properties. These analyses can be easily implemented into existing automated feature detection techniques.

TABLE OF CONTENTS

1. Introduction

Advances in autonomous underwater vehicle (AUV) technology have enabled mapping of the Earth's seafloor at increasingly high resolutions, providing key insights into small-scale seabed processes, such as hydrocarbon fluid flow (Wynn et al., 2014). Mapping of areas where hydrocarbon-rich fluids flow through the seabed is important for understanding the chemosynthetic activity found at these areas (e.g. Foucher et al., 2009), assessing geohazard locations (Hovland and Judd, 2007), formulating environmental impact assessments (Wynn et al., 2014), and understanding local petroleum systems. Areas in which hydrocarbon seepage has deformed the seafloor are referred to here by the term hydrocarbon induced terrains (HITs), per Keller et al., (2007), and more specifically as erosional (formed by methane) or constructional (formed by a mixture of hydrocarbon and sediment) features on the seafloor.

HITs vary widely in their shapes and sizes because the phase and properties of their source hydrocarbon acts to structure their seabed expression. A methodological foundation for objectively identifying and classifying HITs by source provides promise as seafloor surveying capabilities are expanding to encompass more of the ocean floor. This study contributes to building that foundation by comparing geomorphic parameters of HITs formed by gaseous methane, methane hydrate, oil, and mud in the Santa Barbara Basin, Santa Monica Basin, and the Gulf of Mexico. Bathymetric maps were also generated and are included in the appendix to provide visual context for HITs and to facilitate future studies and reports for these sites.

2. Background

Hydrocarbon fluids including methane and petroleum are generated in the marine subsurface. The natural buoyancy of hydrocarbons in combination with pressurization provides the force for vertical migration, which occurs when conduits are present (Hovland and Judd, 2007; Brown, 1990). Evidence of seabed fluid flow has been globally detected: generally resulting in elevated or depressed bathymetric signatures from the accumulation of methane-derived authigenic carbonate, mud, oil, methane, gas hydrate, or a mixture of these constituents. These accumulations are typically associated with high pore fluid pressure, which can cause slope instabilities, and are deep sea oases for aerobic and anaerobic life. Because of their potential to induce mass wasting or slumping, HITs are potential geohazards; they also represent opportunity for scientific advancement. Although they are significant to deep ocean ecosystems and to society, they remain poorly understood. Triggers behind their formation and decomposition processes remain speculative, as they have not yet been actively observed.

2.1 Elevated Hydrocarbon Induced Terrains

Elevated HITs on the seafloor are loosely divided into two categories: those that form from extrusion of material, such as mud or tar volcanoes, and those that form from subsurface expansion of material, such as hydrate mounds (also referred to as pingos or pingoes; Paull et al., 2015; Hovland and Svensen, 2006). Oil and mud seepage have been observed to be expressed on the seafloor as a result of surficial extrusion. Seafloor mud volcanoes are constructed from the accumulation of extruded sediment and are typically positioned over conduits such as faults or fractures (Mazzini and Etiope, 2017). They can

occur in compressional environments where pore fluid is unable to drain, leading to high pore fluid pressure and a density gradient between the fluid and the overlying sediment, ultimately resulting in fluid extrusion (Hovland and Judd, 2007). Volcanoes that extrude fluids containing a mixture of mud, water, brine, and/or oil are termed mud volcanoes (Milkov, 2000; Kopf, 2002). Asphalt volcanoes consist mostly of oil, but methane seepage is typically also present in the vicinity, although at varying intensities (Valentine et al., 2010; Garcia-Pineda et al., 2016). While fewer asphalt volcanoes have been studied, it is likely that they form in similar compressional environments, where asphalt rises to the seafloor via faults or fractures (Valentine et al., 2010; MacDonald et al., 2004).

Gas hydrate is a solid substance consisting of methane or other gases trapped in a water ice lattice. Hydrates have been found to occur in areas of hydrocarbon seepage worldwide (Kvenolden and Lorenson, 2000; Paull et al., 2015; Sahling et al., 2016). They are most commonly observed in the shallow sub-surface, where sufficient pressure, low temperature, and methane supply coincide. Hydrate accumulations in the subsurface can form mounds or pingos where a methane source intersects seawater (Reagan et al., 2008; Paull et al., 2015; Hovland and Svensen, 2006). Because of hydrate dependence on a methane source, methane-derived authigenic carbonates are typically associated with the presence of hydrates. Such authigenic carbonates are formed through anaerobic oxidation of methane, a microbial process. The anaerobic oxidation of methane promotes precipitation of authigenic carbonate through its metabolic end products that include bicarbonate and an increase in alkalinity linked to the reduction of sulfate (Sahling et al., 2002). Hydrate formation in conjunction with precipitation of methane-derived authigenic carbonate can modify methane migration pathways leading to a dynamic state of hydrate dissolution and

formation (Sultan et al., 2014, Loher et al., 2018). Methane hydrates are vulnerable to dissociation through a number of mechanisms, such as temperature and pressure fluctuations, or exposure to methane-poor seawater (Reagan et al., 2008; Paull et al., 2015). Gas hydrate features typically exhibit a distinctive rough topography because they can dissolve and reform in accordance with changes in methane supply or myriad other changes to the local environment.

2.2 Pockmarks

Pockmarks can be formed from the expulsion of methane through the seafloor; their size is influenced by sediment type and overlying pressure (Hovland and Judd, 2007). A simplified conceptual model for their formation is as follows: 1) methane is generated in the subsurface through either biological or thermal processes, 2) it rises and reaches migration barriers near the seabed, 3) this accumulation results in seabed doming, and 4) when sufficient fluid pressure is reached, the sediment dome is scattered from the expulsion of gas and a pockmark is formed (Hovland and Judd, 2007; Loher et al., 2018).

A compilation of 57 studies on pockmarks from around the world, such as the Canadian, central Scottish, Irish, Angolan, and Mediterranean shelves suggests that they are generally 10 – 250 meters in diameter and 1 – 25 meters deep: these studies employed bathymetric, side-scan, and high-resolution seismic surveys for pockmark identification (Pilcher and Argent, 2007). However, pockmarks less than 5 meters in diameter, defined as unit pockmarks, may be more prevalent around areas of active seepage than previously described (Hovland et al., 2010). Pockmarks can also coalesce to form complex features due to scouring by bottom currents and/or natural merging. Giant elongate pockmarks several

kilometers in diameter have also been observed on the edge of the continental shelf of Virginia and North Carolina (Newman et al., 2008). Newman et al. proposed that these elongate features could be a result of pockmarks merging over time from consistent methane seepage on their steeper upslope side.

Pockmarks can exhibit continuous, intermittent, or no seepage. However, signs of past seepage are observed in dormant pockmarks in the form of methane-derived authigenic carbonate and bacterial mats. Numerical simulations of bottom currents have suggested that dormant pockmarks may persist on the seafloor due to local upwelling currents preventing sediment from filling them in (Hammer et al., 2009). Preservation is more likely to occur on the continental slope due to lower sedimentation rates (Yun et al., 1999). The timescale of their formation is not well constrained since seepage varies widely, however, rapid methane release can be triggered by temperature and pressure fluctuations from storm events (Krämer et al., 2017). Episodic methane flow was found to vary at local scales over periods of weeks to months due to cyclic charging and discharge of separate subsurface gas reservoirs (Tryon et al., 1999).

3. Methods

3.1 Study areas and surveys

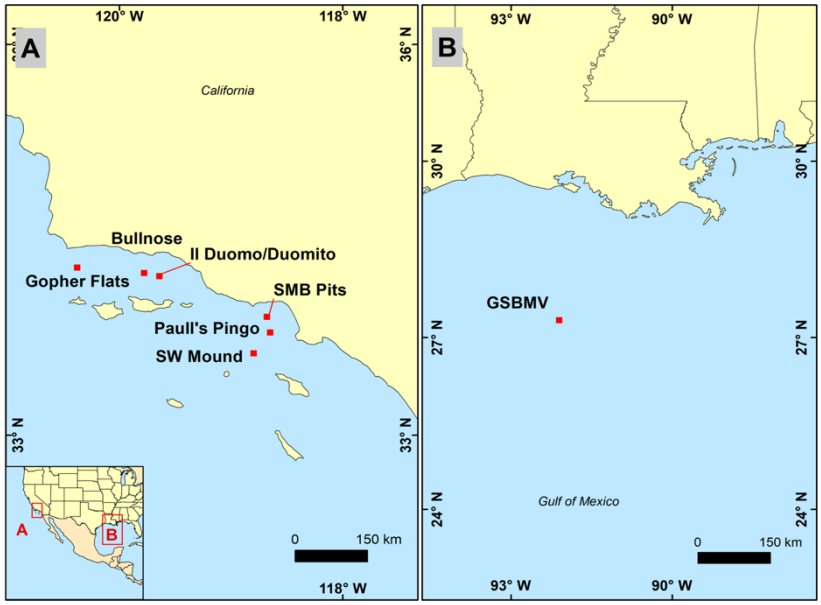

Figure 1: Locations of HIT included in this study. Surrounding bathymetry for sites in the Santa Barbara Basin, Santa Monica Basin, and the Gulf of Mexico are presented in figures 2-4.

For this study we surveyed areas in the Gulf of Mexico and offshore southern California (Figure 1 and Table 1) where oil seepage has been observed (Kvenvolden and Cooper, 2003). In the Santa Barbara and Santa Monica Basins, seepage is controlled by subsurface structures such as faults and faulted anticlines that are associated with the border of the North American and Pacific plates (Eichhubl et al., 2002, Sorlien et al., 2006). Slumping in the Santa Barbara Basin is associated with focused fluid flow due to increased pore fluid pressure (Eichhubl et al., 2000). Pockmarks ranging from 10 – 300 m in diameter were found on the Mid-Channel Anticline: some were characterized by higher backscatter intensities, which probably indicates carbonate slabs (Keller et al., 2007, Eichhubl et al., 2002).

The Gulf of Mexico is dominated by salt tectonics that control offshore faults that act as conduits for hydrocarbon seepage. Salt movement can be triggered by overburden erosion, extension, or uplift: an underlying salt diapir responds by moving towards the direction of least gravitational loading (Hudec and Jackson, 2007). A migrating salt diapir fractures the seafloor along its perimeter, creating planes for underlying hydrocarbons to seep to the surface.

Surveys of six sites of elevated HIT and two pockmark sites were conducted in 2009, 2011, 2013, and 2015 by the AUV Sentry in the Santa Barbara Basin (Figure 2), Santa Monica Basin (Figure 3), and in the Gulf of Mexico (Figure 4). Surveys performed by AUV Sentry were conducted with a Reson 7125, 400 kHz multibeam sonar system (Table 1).

Table 1: The AUV Sentry dives and cruise numbers associated with the sites presented in this study

Site	Date	Cruise Number	Dive Number
Bullnose	09/18/09	AT 15-53	Sentry 030
Il Duomo and Il Duomito	09/19/09	AT 15-53	Sentry 031
Santa Monica Basin Pits	09/25/09	AT 15-53	Sentry 035
Paull's Pingo	09/27/09	AT 15-53	Sentry 036
Gopher Flats	09/19/11	AT 18-11	Sentry 118
Southwest Mound	09/29/13	AT 26-06	Sentry 199
GSBMV	06/24/15 – 06/25/15	AT 29-02	Sentry 319-320

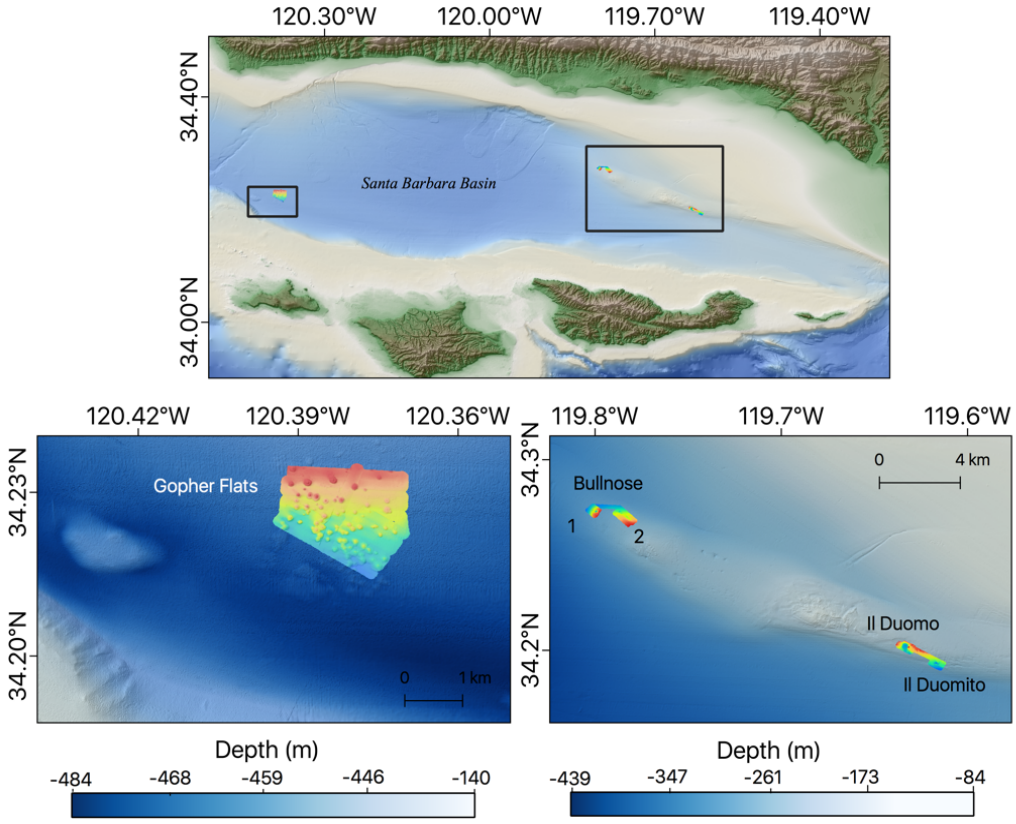

Figure 2: Overview of the Santa Barbara Basin. Coastal Relief Model was obtained from NOAA's National Geophysical Data Center. High-resolution bathymetry and analyses are presented in the results section.

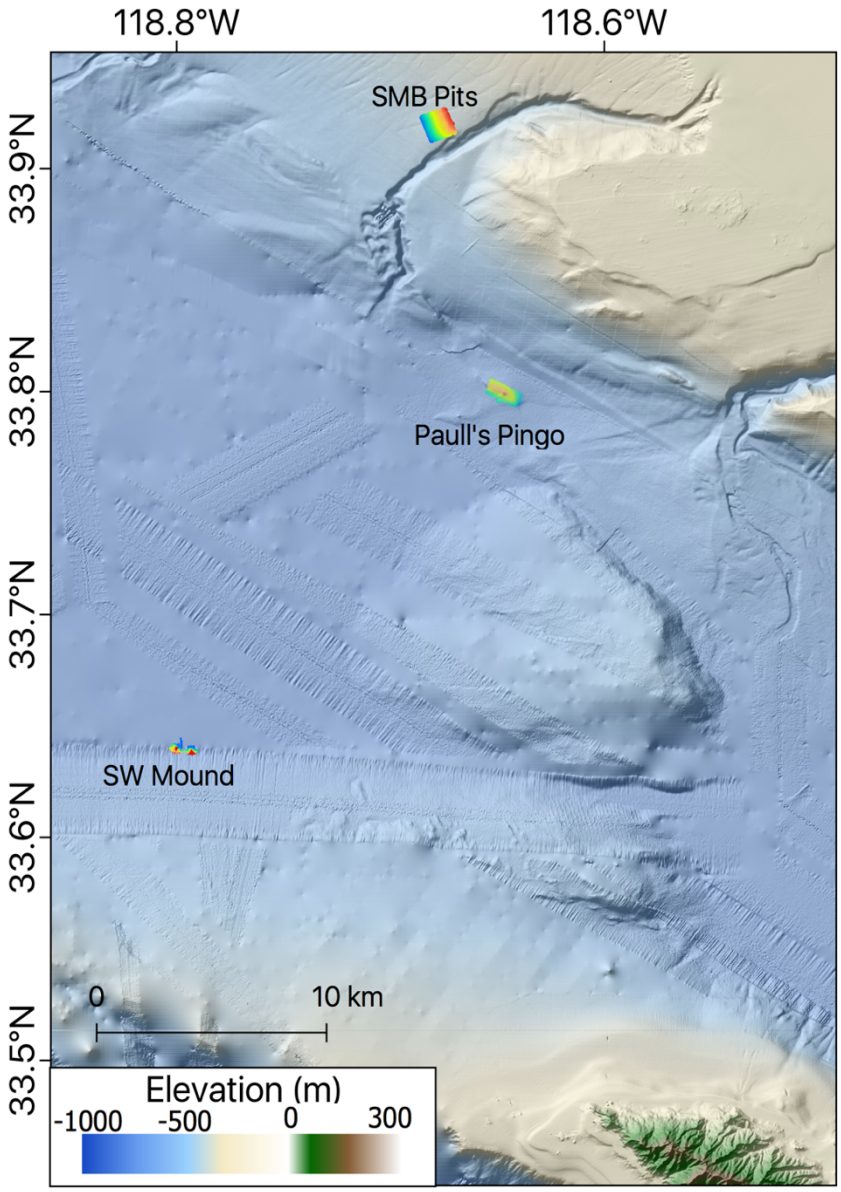

Figure 3: Bathymetry surrounding HIT in the Santa Monica Basin. Coastal Relief Model was obtained from NOAA's National Geophysical Data Center.

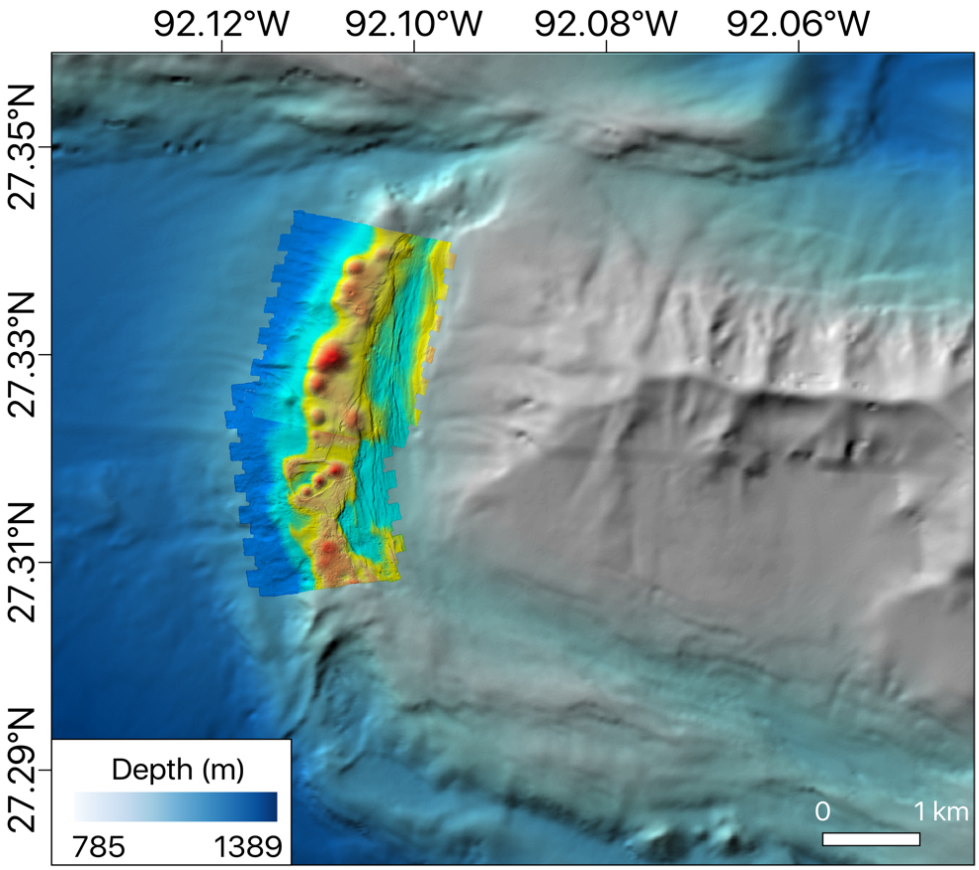

Figure 4: Overview of bathymetry surrounding GSBMV in the Gulf of Mexico. It is adjacent to the salt dome Acadia Mound. Bathymetric data is courtesy of BOEM.

3.2 DEM Generation

Raw bathymetric data was preliminarily processed by the team during each survey at sea, however, further post-processing was required. The open-source software MB-Systems was used to correct inherent errors associated with multibeam surveys such as erroneous sonar soundings, errors associated with the correct positioning of the vehicle, and real-time offsets in its flight path due to currents and errors in its positioning system (Caress et al., 1995; Caress et al., 2008; Kinsey et al., 2011). MB-Systems was also used to generate bathymetric grids for 3D visualization and analysis in ArcGIS 10.5 and the TopoToolbox in MATLAB (Schwanghart, 2015).

3.3 Derivation of terrain attributes

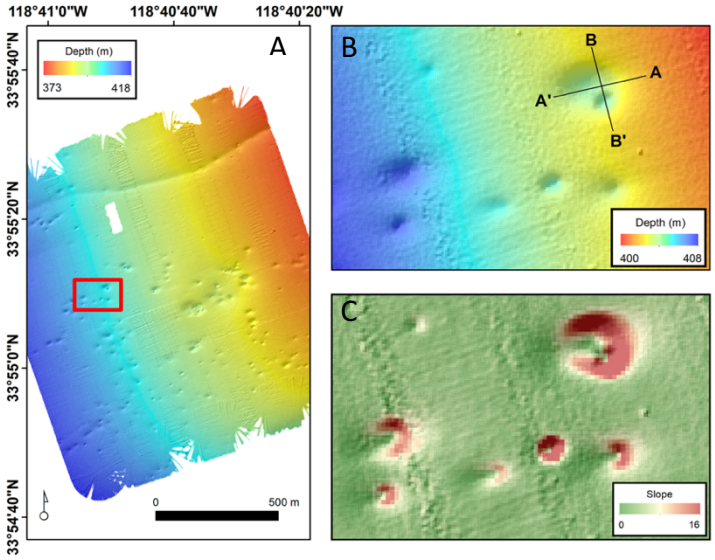

Figure 5: Delineation of pockmarks in the Santa Monica Basin. Cross-sections drawn to the extent of the feature's boundary are shown in panel B. The slope gradient used to define boundaries is shown in panel C.

ArcGIS 10.5 was used to analyze the features of interest, where feature boundaries were defined manually using abrupt changes in slope identified on digital elevation model derivatives (Figure 5). The area within this boundary was defined as the base of the feature and cross-sectional profiles were drawn at the extent of these boundaries and are shown for each site. To characterize the planform nature of each feature, the Minimum Bounding Geometry tool in ArcGIS was used to calculate major and minor axes of the base. An aspect ratio, calculated by dividing the major axis by the minor axis, was used to define the asymmetry of the feature, whereby a perfect circle would have a ratio of 1. Volumes were estimated above the lowest elevation of each feature. Relief was defined as the difference between maximum and minimum elevation within each feature. To compare the coarse relationships between source and flatness, flatness indices are defined as the ratio of basal area to relief, and have units in meters.

To analyze the three-dimensional shape, aspect and elevation values were extracted for each feature at each site. Aspect is defined as the downslope direction of the maximum rate of change between each cell and its eight neighbors. This is calculated in ArcGIS using the Aspect tool, which fits a plane to the elevation values in a 3x3 window and defines the aspect of the center cell as the direction that the plane faces. Aspect values range from 0 – 359.9, with 0 degrees representing true north. Aspects were distributed into 10 degree bins and normalized over the total cell count. Aspects were analyzed for the whole feature as well as the area above a flat bottom (AFB) for elevated HIT, defined by the highest perimeter point (Figures 7 - 12). For pockmarks, aspects were analyzed below a flat ceiling (BFC), defined by the lowest perimeter point (Figures 17 – 18).

Elevation data was normalized for comparison by subtracting the minimum elevation within each feature and dividing by relief. A hypsometric curve was generated for each feature and for each site by generating a cumulative distribution function of the normalized elevations. Normalized area was calculated by multiplying pixel count by area (1 sq. meter). Hypsometric indices (HI) were defined as the area below the curve and represent a more detailed elevation to area ratio. A hypsometric index of 0 could represent a horizontal plane with a few elevated points, while an index of 1 could represent a rectangular prism. Different shapes and indices describe a relationship between constructive and destructive surface processes, and have been utilized to differentiate drainage basin types and shield volcano ages (Strahler, 1952; Luo, 2000; Bleacher and Greeley, 2008).

4. Results

Digital elevation models and a brief summary of direct observations for elevated and depressed HITs are presented in sections 4.1 and 4.2. At the end of each section, geomorphometric comparisons are conducted.

4.1 Elevated Hydrocarbon Induced Terrains

Gopher Flats

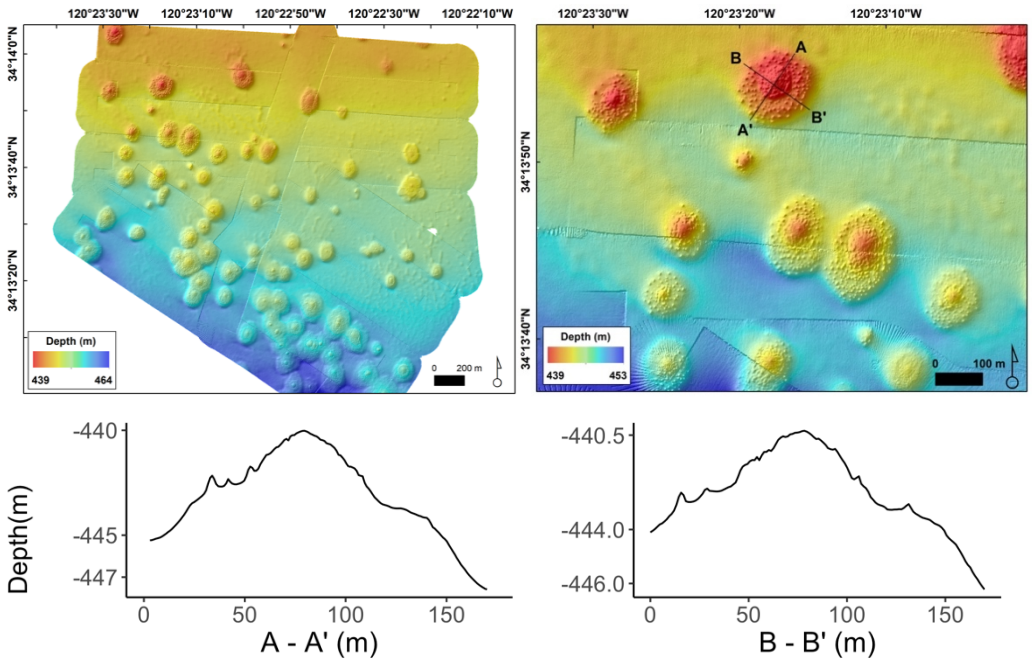

Figure 6: Digital elevation model of oil mounds at Gopher Flats

Gopher Flats is a site located on the western edge of the Santa Barbara Basin (Figure 2). Direct observation showed that they were formed by the extrusion of oil, forming mounds with an average relief and basal area of 5.3 meters and 11 * 10^3 m^2 (Table 2). The size of the mounds at this site vary widely. Some mounds are even peppered with smaller oil mounds (Figure 6b). The seafloor at this site is characterized by a hummocky texture,

possibly representing subsurface oil mounds. Although the subsurface was not surveyed, a sub-bottom profile from Eichhubl et al. (2002) confirms the presence of acoustic anomalies in the subsurface. Direct observations did not reveal active oil extrusion, but methane was observed to degas from oil samples that were brought to the surface.

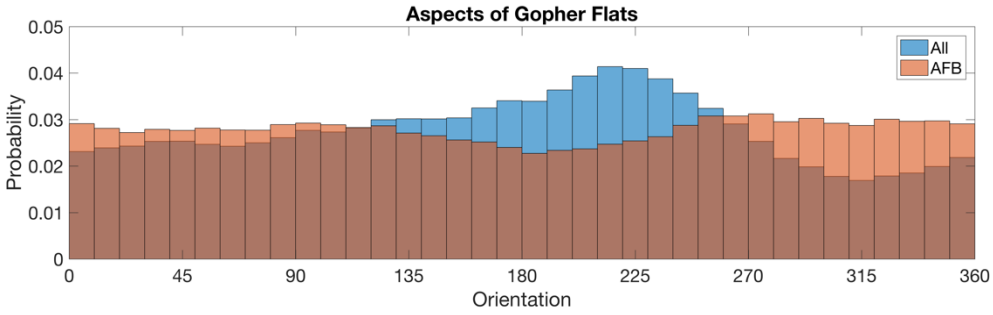

Figure 7: Aspects of cells for mounds at Gopher Flats. AFB denotes aspects above the flat bottom of each mound, defined by the highest point on its perimeter.

Gopher Flats exhibits a peak in aspect distributions at 225 degrees from due north, which is the direction of increasing depth and a minimum at approximately 315 degrees from due north (Figure 7). When analyzed above a flat bottom, these aspects showed an even distribution, with orientations at 225 degrees slightly less probable. Aspect distributions vary largely across individual features, the aspects of the mound shown in Figure 6b did not show a preferential distribution.

Il Duomo and Il Duomito

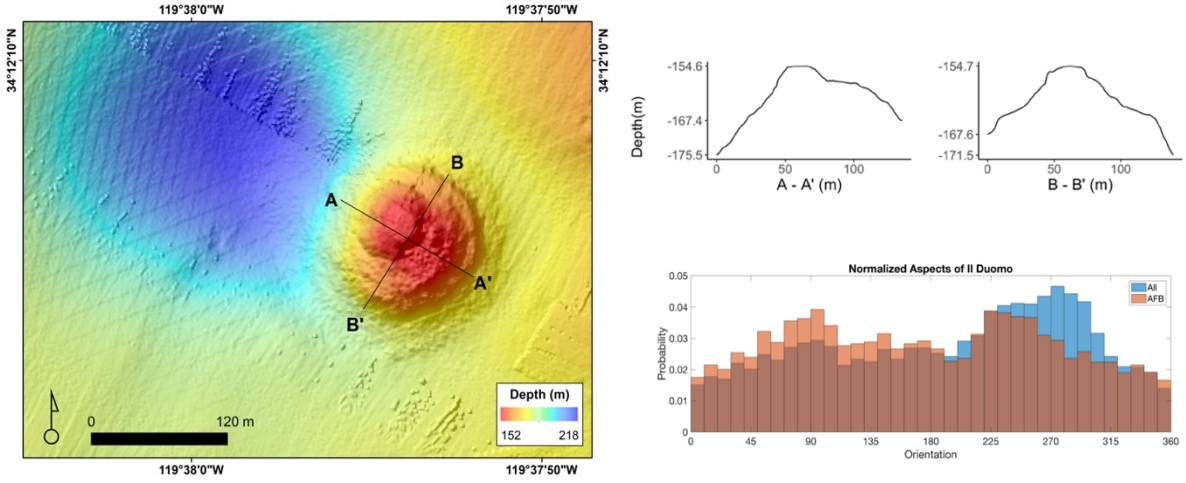

Figure 8: Digital elevation model and a brief geomorphic summary of the asphalt volcano at Il Duomo.

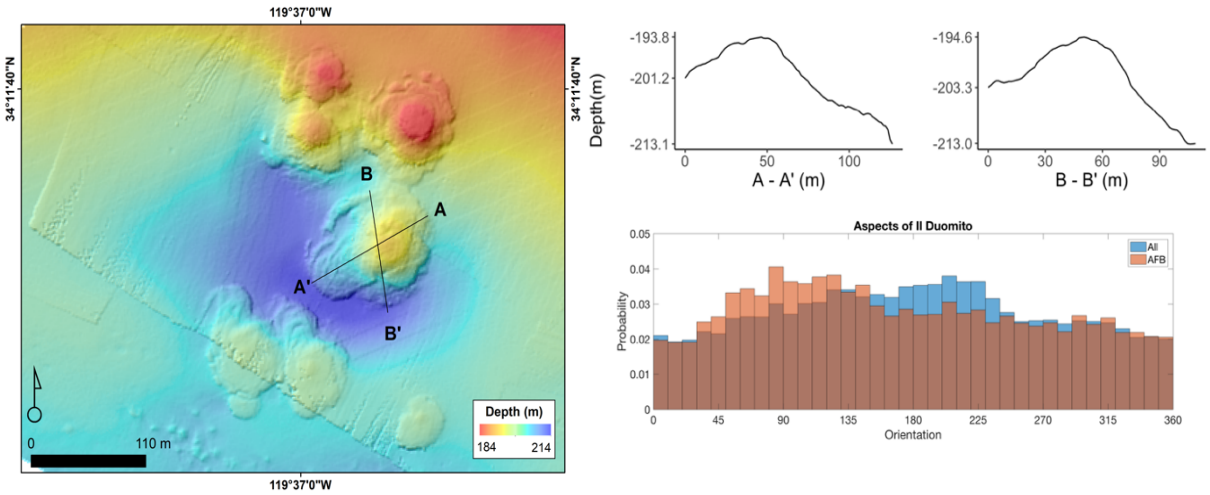

Figure 9: Digital elevation model and a brief summary of asphalt volcanoes at Il Duomito

Il Duomo and Il Duomito are dormant asphalt volcanoes located on the Mid Channel Anticline that likely share the same oil source. Il Duomo is a singular volcano on the western side of the survey site and is adjacent to a large depression (Figure 8). Il Duomito is a group of 6 asphalt volcanoes within a local depression (Figure 9). They were estimated to play a significant role in paleo-methane flux, and inferred to be of compressional origin due

to the lobed, lava-type flows they exhibit (Valentine et al., 2010). Before they were sampled, Keller et al. (2007) noticed the volcanoes as mounds and hypothesized they were a result of hydrocarbon fluid flow, but was not able to confirm their origins.

Paull's Pingo

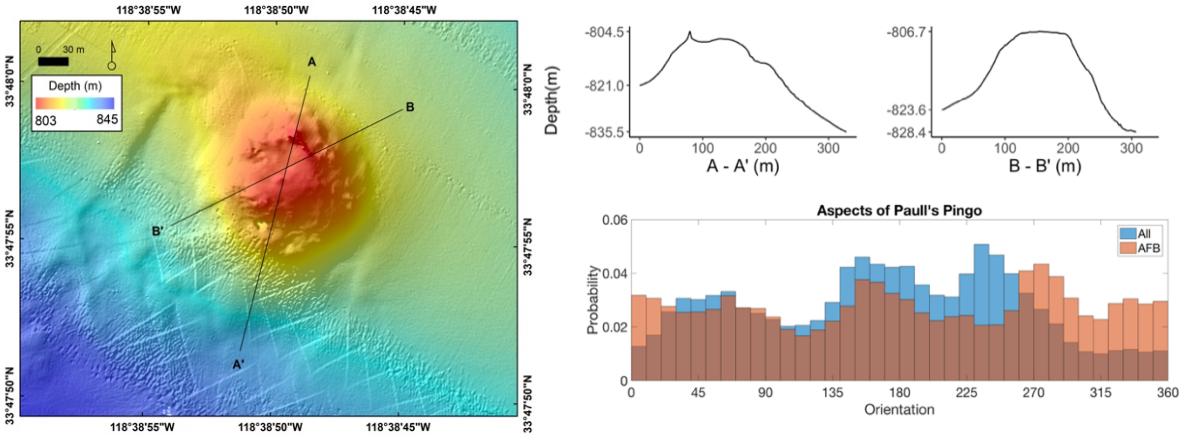

Figure 10: Digital elevation model and a brief geomorphic summary of Paull's Pingo

Paull's Pingo is a methane hydrate feature in the Santa Monica Basin. It is located on the flank of a large bathymetric swell, and has been previously studied by Paull et al. (2008). Some of their observations can also be observed in the bathymetry presented here. For example, the northern area is characterized by a large sediment-free carbonate ridge, seen as a peak at approximately 90 meters in the cross-section A – A' (Figure 10). The southwest flank of the pingo has slumped away, which may be a result of hydrate dissolution. Active methane seepage was observed near the crest of the mound by Paull et al. (2008) as well as during our surveys.

Southwest Mound

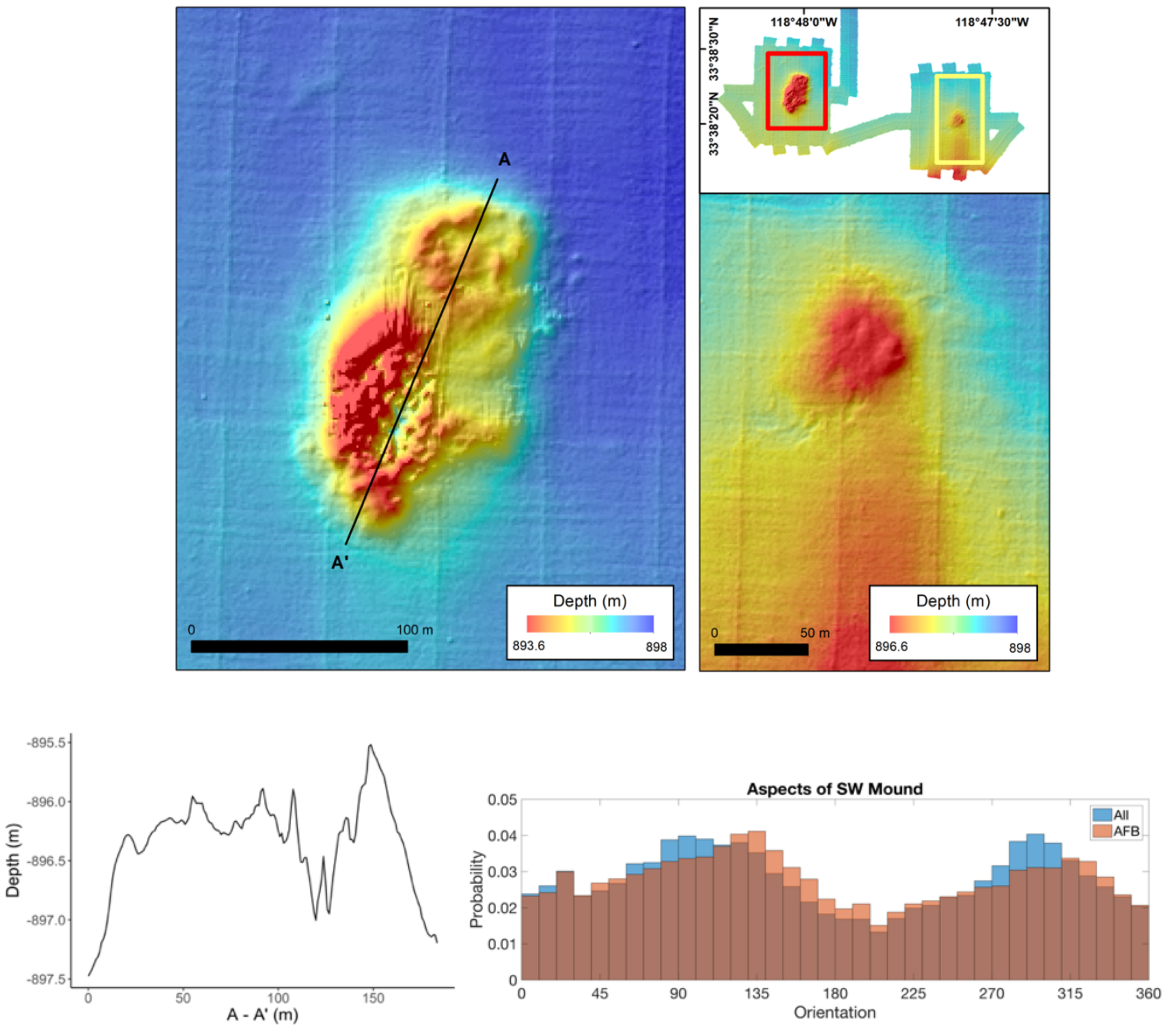

Figure 11: A summary of Southwest Mound. The eastern mound was difficult to delineate, as it had a maximum relief of 0.72 meters and a mean slope of 1.13 degrees.

Southwest Mound is a hydrate mound in the Santa Monica Basin. It is the smallest feature studied here. Active methane seepage was observed at this site (Valentine, personal communications). Its surrounding seafloor exhibits slopes of less than 0.5 degrees, so its orientation is not as affected as the other features studied here (Figure 11). The distribution of aspect values above its highest perimeter point is not substantially different than all of its aspects. The ancillary mound has similar peaks in aspect distributions at approximately SE-

NW (Figure 12). Hence, the preferential orientations at SE-NW of the hydrate mounds may indicate the influence of bottom currents or the orientation of its subsurface methane supply.

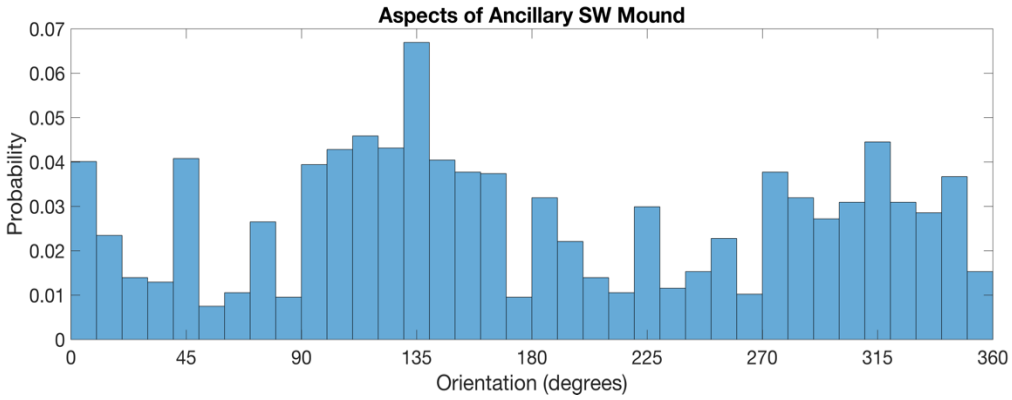

Figure 12: Aspect distribution of ancillary mound at SW Mound site

Gas Spewing Brine Mud Volcano (GSBMV)

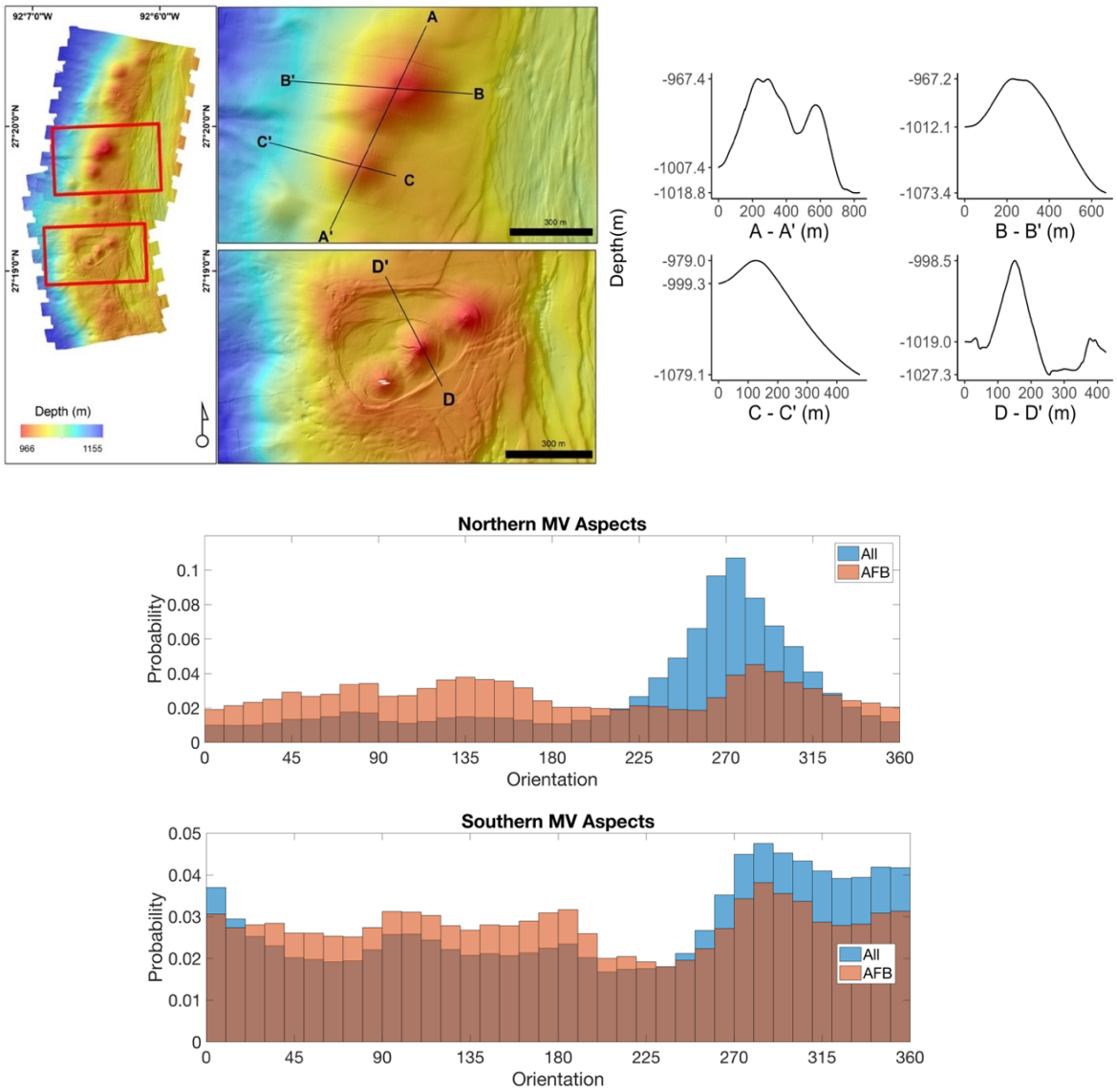

Figure 13: Summary of gas-spewing brine mud volcanoes in the Gulf of Mexico. The southern three mud volcanoes are located within a moat that contains a brine pool.

Six mud volcanoes were delineated in the Gulf of Mexico adjacent to Acadia Mound (Figure 4). All volcanoes are located on a local ridge and display slumping towards the steeper western flank, consistent with expected deformation from its adjacent salt mound.

Three are located inside of a moat that includes a brine pool (Figure 13). The eastern side of the survey area is characterized by lineations approximately parallel to the ridge. These lineations are interpreted to be deformation structures from the adjacent salt dome, and may be related to the conduits that formed the mud volcanoes.

Comparing Elevated Hydrocarbon Induced Terrains

Table 2: Morphometric parameters for elevated features. ± denotes standard deviation

	Gopher Flats	Il Duomo	Il Duomito	Paull's Pingo	SW Mound	GSBMV
Source	Oil	Oil	Oil	Gas Hydrate	Gas Hydrate	Mud
Activity	Dormant	Dormant	Dormant	Active	Active	Active
Count	54	1	6	1	1	6
Depth (m)	439 - 464	152 - 218	184 - 214	803 - 845	893 - 898	966 - 1010
Major Axis (m)	134 ± 41	121	79 ± 32	255	188	300 ± 140
Minor Axis (m)	103 ± 30	113	59 ± 21	206	119	376 ± 159
Length/Width	1.30 ± 0.15	1.07	1.33 ± 0.10	1.58	1.28	1.26 ± 0.1
Relief (m)	5.3 ± 1.8	24.5	12.7 ± 6.3	33.4	4.0	58.3 ± 32.1
Basal Area (10^3 m^2)	11.37 ± 6.08	10.45	3.97 ± 2.87	40.09	16.25	94.24 ± 80.92
Volume (10^3 m^3)	39.3 ± 29.5	147.2	30.06 ± 29.46	877.57	19.84	4629 ± 5872
Average Slope (°)	4.4 ± 0.8	21.2	16.7 ± 5.1	11.3	3.9	13.5 ± 1.5
Area/Relief (10^3 m)	2.04 ± 0.7	0.43	0.3 ± 0.17	1.2	4.06	1.45 ± 0.53
HI	0.56 ± 0.06	0.57	0.58 ± 0.08	0.5	0.3	0.49 ± 0.06

Plotting the flatness index against slope indicates subtle differences between sources (Figure 14). Oil features at Il Duomo/Il Duomito and Gopher Flats show different relationships between their area/relief ratio and average slope value. Features dubbed ‘volcanoes’ have high slopes with low area/relief ratios while features dubbed ‘mounds’

have low slopes with high area/relief ratios. This may suggest different growth mechanisms for ‘volcanoes’ and ‘mounds’ despite both being comprised of similar oil. The ‘volcanoes’ tend to grow upwards instead of outwards, while mounds cover a larger area with less relief. Slopes for the flatter mounds are lower, and relatively consistent at approximately 3-5 degrees. Mud volcanoes in the Gulf of Mexico exhibited a higher flatness index than the volcanoes at Il Duomo, but similar slopes between 10-15 degrees.

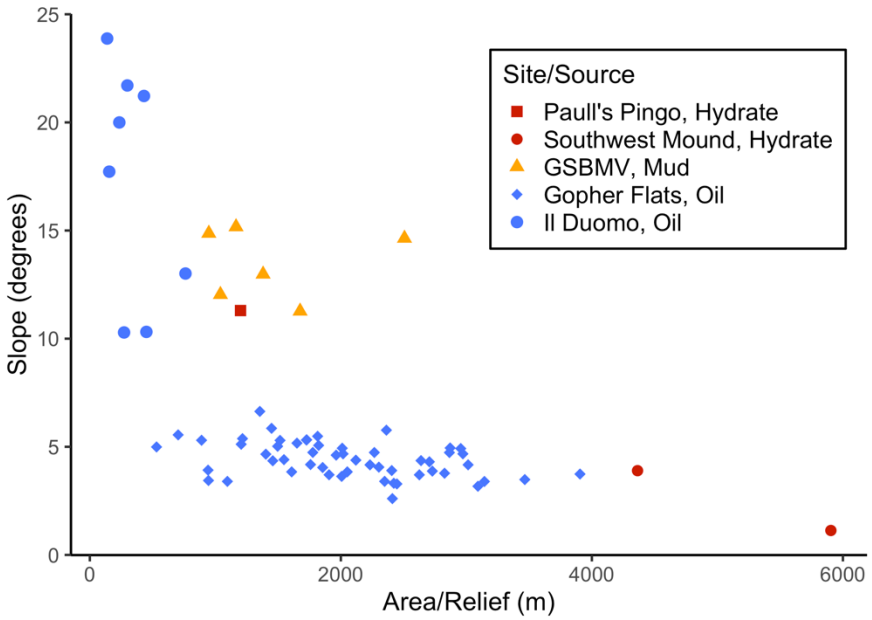

Figure 14: Flatness index plotted against slope for each delineated feature. A small ancillary hydrate mound from Southwest Mound with an area of 4521 m^2 and 0.7 m of relief is plotted for comparison.

Although there were only two hydrate structures studied here, they also show a separation in their flatness index and slope values. Southwest Mound has a high flatness index and low slope, while Paull’s Pingo has a lower flatness index and higher average slope. The aspects of the hydrate features show two maximums: SW Mound at 130 and 300 degrees, and Paull’s Pingo at 170 and 290 degrees. The aspects of Paull’s Pingo are more irregular than those at SW Mound due to its position on a bathymetric swell.

Hypsometry

Hypsometric analyses were conducted to examine the relationship between relief and area with more detail by analyzing the distribution of normalized elevation over normalized planar area (Figure 15). Changes in relief and area for these elevated features are interpreted to be related to the overlying sediment, subsurface geometry, and source. The hypsometric index represents a comprehensive distribution of a given terrain's elevation over its planar area, and represents a more detailed flatness index.

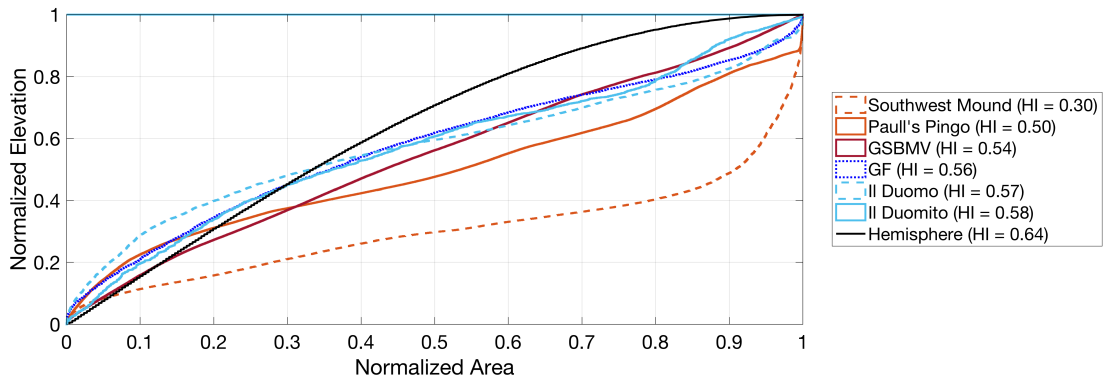

Figure 15: Aggregate hypsometric curves for elevated HIT and an ideal hemisphere of radius 1. Over and underrepresentation of elevation values are determined at half of the normalized area.

Oil mounds and volcanoes had the highest hypsometric index at 0.56 – 0.58, Southwest Mound had the lowest at 0.33, and Paull's Pingo and mud volcanoes were in between at 0.50 and 0.54, respectively. Further classification is accomplished through comparing the overrepresentation or underrepresentation of elevation values across half of their planar area. An ideal hemisphere has a hypsometric index of 0.64 and half of its planar area is overrepresented by the highest 30% of its elevation values (Figure 15). Half of the planar area of Paull's Pingo is distributed between the highest 55% of its elevation values. This fraction of its elevations is slightly underrepresented over its planar area. In contrast,

half of the planar area of mud volcanoes is distributed between the highest 45% of its elevation values. These elevation values are overrepresented over its planar area. For oil mounds, the highest 40% of elevation values represents half of their planar area. Overrepresentation reflects the source's stability without succumbing to gravitational force pulling it towards its lower sections.

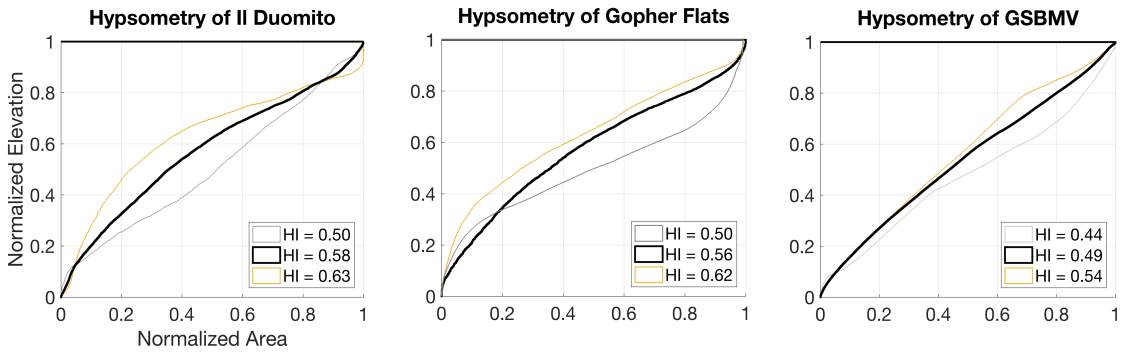

Figure 16: Average hypsometric curves for sites with n > 1 feature. Upper and lower limits are represented in these plots by an individual feature with a HI closest to one standard deviation from the mean curve.

For sites with multiple features, there was a considerable range in hypsometric indices and curves. Standard deviation for the hypsometric curves for sites with multiple features were plotted (Figure 16). Values for oil mounds at Gopher Flats ranged from 0.33 – 0.66 and oil volcanoes at Il Duomito ranged from 0.43 – 0.68. Mud volcanoes ranged from 0.40 – 0.57. The southern three volcanoes had values of 0.40 – 0.47 while the northern volcanoes had values of 0.54 – 0.56.

This spectrum of hypsometric indices approximately parallels the spectrum of the stability of each hydrocarbon source. Oil terrains are the most stable, mud terrains are midway, and hydrate terrains are the least stable. Paull's Pingo may exhibit a higher hypsometric index than typical hydrate features because its hydrate is inferred to be sealed

below a layer of methane derived authigenic carbonate and surficial chemosynthetic biologic communities (Paull et al., 2008).

4.2 Pockmarks

Santa Monica Basin Pits

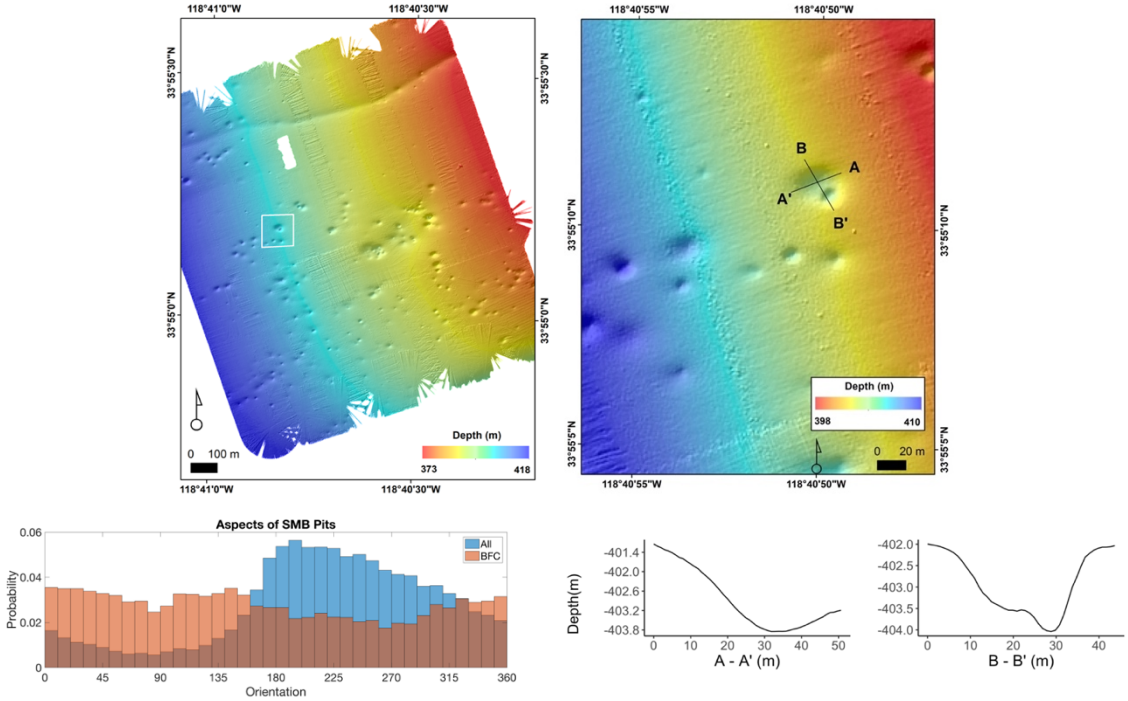

Figure 17: A summary of pockmarks at SMB Pits

Pockmarks at the Santa Monica Basin Pits were observed to be dormant. Pockmarks are U-shaped and tilted downslope: their walls were steeper upslope than downslope (Figure 17). Some pockmarks have developed inside larger ones.

Bullnose

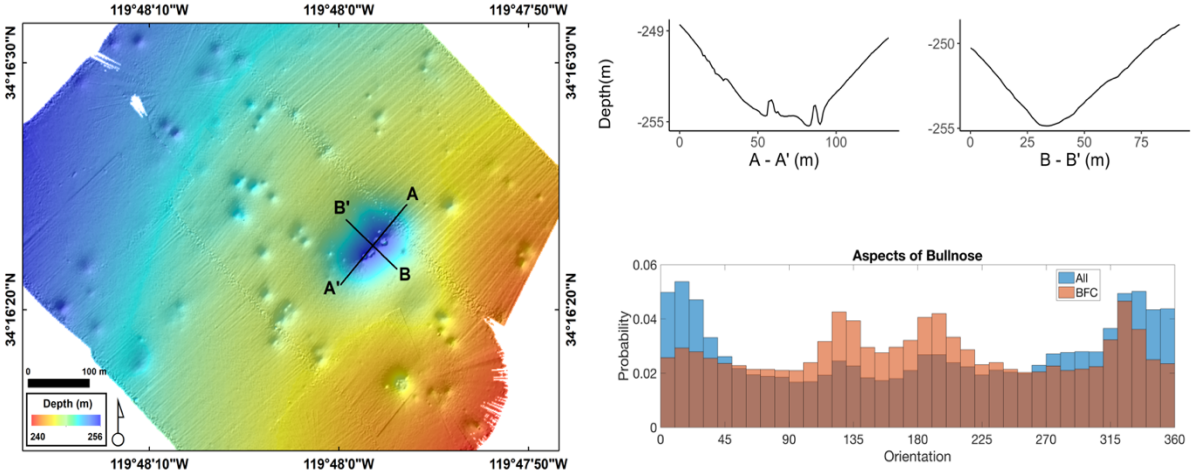

Figure 18: Block 1 of the pockmarks at Bullnose. Block 2 is presented in the appendix.

Bullnose is located on the northwestern end of the Mid-Channel Anticline in the Santa Barbara Basin. Pockmarks at Bullnose were actively seeping methane during the survey. One-meter high carbonate slabs were observed in the center of some pockmarks (Figure 18). Pixels are preferentially oriented north and south, but below a flat ceiling pixels preferred to be oriented south-southeast.

Comparing Pockmarks

Table 3: A summary of morphometric parameters for pockmarks in this study

Site	Santa Monica Basin Pits (n = 109)	Bullnose (n = 214)
Source*	Methane	Methane
Activity	Dormant	Active
Depth (m)	397	225
Length/Width	1.39 ± 0.26	1.32 ± 0.19
Relief (m)	1.6 ± 0.7	1.38 ± 1.68
Basal Area ($10^3 m^2$)	0.504 ± 0.421	0.719 ± 4.503
Volume ($10^3 m^3$)	0.479 ± 0.746	1.28 ± 9.73
Slope (°)	4.9 ± 1.6	6.3 ± 1.2
Area/Relief	0.32 ± 0.6	0.59 ± 3.75
HI	0.50 ± 0.05	0.51 ± 0.06

*Source is presumed in the case of the Santa Monica Basin Pits

The sizes of the pockmarks at both sites vary widely (Table 3). Three pockmarks at Bullnose have basal areas in the tens of thousands of square meters and reliefs an order of magnitude larger than the average. Reliefs for SMB Pits and Bullnose varied from 0.58 – 5.84 m and 0.35 – 18.6 m. Areas ranged from 69.7 – 3076.2 m^2 and 28.8 – 61539.4 m^2 for SMB Pits and Bullnose. Volumes ranged from 18 – 5245 m^3 and 11 – 102470 m^3 for SMB Pits and Bullnose.

To examine the variations in size, volumes are examined by magnitude. The total volume of pockmarks larger than 1000 m^3 at SMB Pits and Bullnose was $2.6 * 10^4$ m^3 and $2.7 * 10^5$ m^3, respectively. Seven pockmarks at Bullnose had volumes in between 10^3 and 10^4 m^3, two between 10^4 and 10^5 m^3, and the largest was on the scale of 10^5 m^3. Fourteen pockmarks at SMB Pits had volumes in between 10^3 and 10^4 m^3. No pockmarks at SMB Pits had volumes larger than 10^4 m^3.

Pockmarks with volumes less than 1000 m^3 at SMB Pits and Bullnose have a mean area of 480 ± 340 m^2 and 224 ± 203 m^2, a mean relief of 1.55 ± 0.7 m and 1.16 ± 0.5 m, and a mean volume of 348 ± 324 m^3 and 163 ± 226 m^3. Nearly 60% of Bullnose pockmarks have volumes less than 100 m^3, as opposed to 20% of pockmarks at SMB Pits (Figure 19).

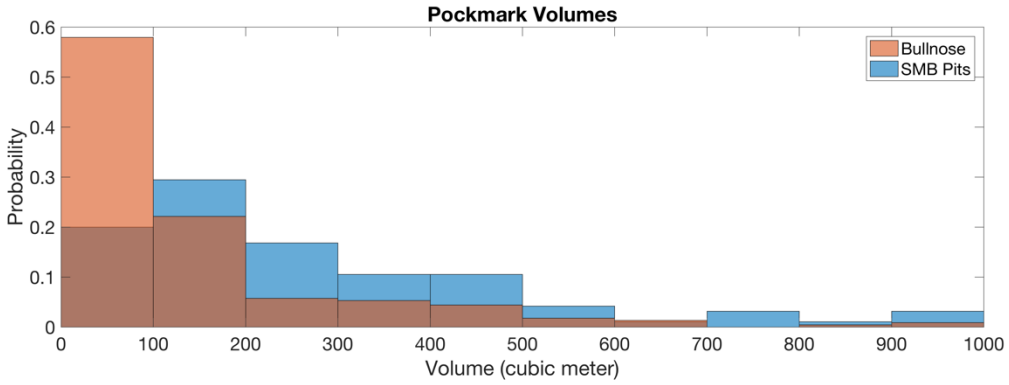

Figure 19: Volumes of pockmarks less than 1000 m^3. A majority of pockmarks at Bullnose are below 100 m^3.

Smaller and shallower pockmarks formed from recent seepage, which can explain the difference in size between the two sites, since SMB Pits was observed to be dormant and Bullnose was observed to be active. An active site is consistently forming pockmarks, and it is expected that there are more young pockmarks being formed than at a dormant site. Bullnose also has much larger elongate pockmarks, which are the product of coalescing pockmarks through continued methane seepage. This is expected at a site where methane is seeping continuously. We interpret these results as follows: active sites are more likely to have more unit pockmarks and sites that have unit pockmarks within large elongated pockmarks are likely to have undergone significant long term seepage.

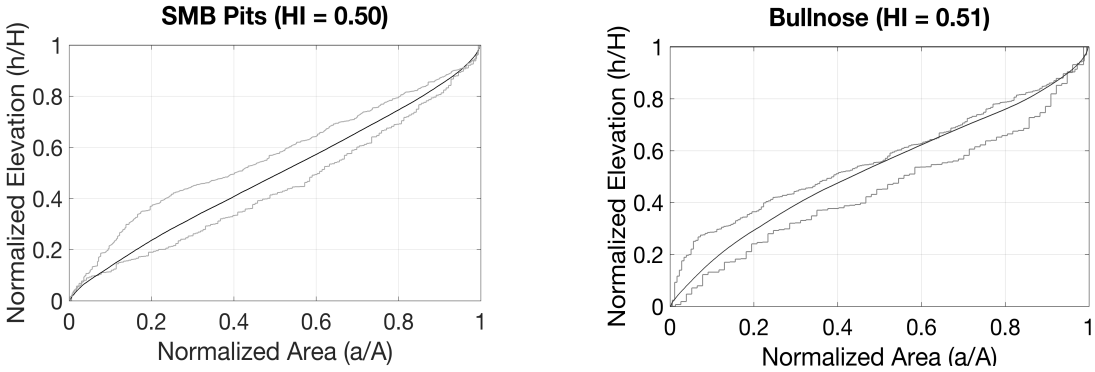

Figure 20: Aggregate hypsometric curves for SMB Pits and Bullnose, plotted with upper and lower bounds

Mean hypsometric indices for SMB Pits and Bullnose are 0.50 ± 0.05 and 0.51 ± 0.06 (Figure 20). However, a higher proportion of Bullnose pockmarks have elevations concentrated at relatively lower depths. Similar hypsometric indices may represent pockmarks formed by methane expulsion. Pockmarks may also be formed from freshwater expulsion, and these may have different shapes.

5. Discussion

Geomorphic parameters such as area, relief, slope, and hypsometric indices can classify HITs based on properties inherent to hydrocarbon sources. It is already well known that constructive features form from a build up of fluidized sediment, such as oil, mud, or gas hydrate, which typically host methane gas as a fluid. They have varying proportions of methane, and this influences the roughness of their topography.

5.1 Aspect distribution

All features in this study seem to be affected by local bathymetry, which is seen in their aspect distribution. They are elongated in the direction of surrounding slope. In areas where seafloor slope is insignificant, such as SW Mound, the aspect distribution may represent the influence of bottom currents or conduit orientation. Since gas hydrate mounds are typically open systems and require a flux of methane and water, the orientation of a hydrate mound could also represent a proxy for the direction of subsurface fluid flow. The hydrate mounds at SW Mound were preferentially oriented SE-NW, which may indicate a narrow SW-NE fault plane.

5.2 Flatness indices and slope

Comparing area, relief, and mean slope prove effective in distinguishing between flat and tall features. Volcanoes should have lower flatness indices and higher slopes, whereas mounds should generally have higher flatness indices and lower slopes. These relationships are consistent with magmatic hydrothermal submarine volcano and dome growth studied in the deep Canary Basin (Sánchez-Guillamón et al., 2018; Medialdea et al., 2017). Their flatness may differ because of different conduit geometries. A singular conduit is inferred to

have formed each volcano at Il Duomo and Il Duomito from lobed, lava type flows observed at their surfaces. The material that formed mounds at Gopher Flats did not exhibit an obvious flow pattern. Instead, some mounds were populated with sub-meter oil mounds. These "peppercorns" are interpreted to be evidence of seepage directly to the seafloor, and is corroborated by the subbottom profiles from Eichhubl et al. (2002). This may suggest that mounds at Gopher Flats formed via a wider conduit or a group of conduits.

The contrasting flatness of the oil mounds and asphalt volcanoes studied here could also be related to their age or the viscosity of the oil seeped. While the age of the asphalt volcanoes from five samples were constrained to 44 – 31 kyr ago (Valentine et al., 2010), the age of mounds at Gopher Flats have yet to be determined. Viscosities of the hydrocarbon fluids that initially formed these solidified features are also unknown, however, they are both likely sourced from the Monterey formation.

The high area to relief ratio for the gas hydrate mounds studied here are consistent with other observations. Ten circular hydrate mounds in the Barkley Canyon were observed to be 10 m in diameter and 2 m high (Paull et al., 2015); seven mounds on the mid-Norwegian shelf were observed to be 4 m in diameter and 1 m high (Hovland and Svensen, 2006). While a high ratio of area to relief is by no means unique to hydrate mounds, it may indicate a characteristic common to such features. Most hydrate mounds studied to date are ovoid shaped with distinctive rough bathymetry (Hovland and Judd, 2007; Paull et al., 2015).

5.2 Hypsometry

Hypsometric analysis classifies features by source with more detail than flatness indices and slope because it considers the distribution of normalized elevation over

normalized area. The spectrum of hypsometric indices for oil, mud, and gas hydrate parallel their stabilities, with oil being the most stable and hydrate being the least. Oil terrains are generally more stable than mud terrains because oil terrains consist of a lower proportion of low viscosity fluids such as water, brine, or methane. Gas hydrate is inherently unstable when compared to oil and mud because it exists only within a limited range of temperature and pressure.

Gas hydrate is formed by the crystallization of water around methane, and thus is dependent on a persistent methane and seawater supply. Seabed methane flux is difficult to quantify, but its intensity has been found to vary widely in space and time, and is sensitive to pressure or temperature changes (Römer et al., 2016, Krämer et al., 2017). Methane flux may also vary locally due to the cyclic charging and release of different local subsurface gas reservoirs (Tryon et al., 1999). Methane seepage pathways can also be sealed by hydrate formation and carbonate precipitation, diverting methane flux. In general, hydrate features are characterized by rough topography due to sediment deformation associated with dynamic patterns of hydrate accumulation and dissociation, which can be a consequence of intermittent methane flux.

High hypsometric indices for hydrate mounds could indicate higher stability, whereas low indices represent lower stability. This range of stability can be partly attributed to the degree of carbonate cementation of near surface sediment, which lowers sediment permeability. Instead of diverting methane flux, continuous subsurface carbonate precipitation may also trap methane gas, allowing for large accumulations of gas hydrate. Cementation of near surface sediment by methane-derived authigenic carbonate was interpreted to trap a sufficient amount of methane for the large amount of hydrate

accumulation that formed Paull's Pingo (Paull et al., 2008). Higher indices suggest that the feature was subjected to less hydrate dissociation, which could be associated with carbonates cementing the sediment.

Hypsometric indices represent a relationship between constructive and destructive surface processes. Since the topography of hydrate features is associated with hydrate inflation and dissolution, they should have lower values than HITs sourced from oil or mud. While the mean HI values from this study support this, smaller oil-derived mounds at Gopher Flats displayed lower HI values of 0.33. Thus, features may have to be large enough that pixel resolution does not affect hypsometric analyses. As the seafloor is mapped at higher resolutions, more features will be recognized but the robust identification and quantification of smaller features will depend on a ratio of pixel resolution to feature size.

5.3 Future applications

By 2030, the seafloor will be mapped in its entirety (Mayer et al., 2018). High-resolution bathymetric data will continue to accumulate for decades to follow, depending on advances in AUV and multibeam technology. This goal will also facilitate the use of AUVs in areas of interest, such as hydrocarbon induced terrains. In areas of HIT, classifying the structures based on source could prove valuable in preliminary assessments because accessing of the cost of and difficulty in directly accessing these areas by other means. Hypsometric analyses can easily be integrated into an automated feature detection algorithm that includes sub-bottom profiling and other inputs, where seafloor features are automatically extracted from bathymetry and other acoustic products (e.g., Masetti et al., 2018). As more features are mapped and studied, hypsometry could prove useful for

classifying source-specific features that are difficult to access based on age or characteristics inherent to the extruded fluid. This could include other planets or moons dominated by methane, such as Titan (Hayes et al., 2018).

Geomorphic analyses of HIT shape can help investigators ask pertinent questions regarding HIT formation and the surrounding factors that influence their shape. Until more work is done to constrain formation processes for these features, the work here represents a preliminary quantification of their shapes: no definitive conclusions were made. Future geomorphic classification of HITs based on source should focus on features with similar bathymetric surroundings, as it was difficult to quantify the effect that local bathymetry had on the shape of the feature in this study. However, geomorphically parameterizing HITs will prove useful as more research is done to understand surface processes controlling their shape. Given the importance of understanding chemosynthetic communities and geohazards associated with hydrocarbon seepage, a deeper understanding of the driving forces behind HIT is inevitable, especially as seafloor surveying capabilities expand.

Works Cited

Andrews, B. D., Brothers, L. L., & Barnhardt, W. A. (2010). Automated feature extraction and spatial organization of seafloor pockmarks, Belfast Bay, Maine, USA. *Geomorphology*, *124*(1–2), 55–64. https://doi.org/10.1016/j.geomorph.2010.08.009

Bleacher, J. E., & Greeley, R. (2008). Relating volcano morphometry to the developmental progression of Hawaiian shield volcanoes through slope and hypsometric analyses of SRTM data. *Journal of Geophysical Research: Solid Earth*, *113*(9), 1–8. https://doi.org/10.1029/2006JB004661

Brown, K. M. 1990. The nature and hydrogeologic significance of mud diapirs and diatremes for accretionary systems. *Geology*, *95*(90), 8982–8982.

Caress, D. W., & Chayes, D. N. (1995). New software for processing sidescan data from sidescan-capable multibeam sonars. *"Challenges of Our Changing Global Environment". Conference Proceedings. OCEANS '95 MTS/IEEE*, *2*, 997–1000. https://doi.org/10.1109/OCEANS.1995.528558

Eichhubl, P., Greene, H. ., Naehr, T., & Maher, N. (2000). Structural control of fluid flow: offshore fluid seepage in the Santa Barbara Basin, California. *Journal of Geochemical Exploration*, *69–70*, 545–549. https://doi.org/10.1016/S0375-6742(00)00107-2

Eichhubl, P., Gary Greene, H., & Maher, N. (2002). Physiography of an active transpressive margin basin: High-resolution bathymetry of the Santa Barbara basin, Southern California continental borderland. *Marine Geology*, *184*(1–2), 95–120. https://doi.org/10.1016/S0025-3227(01)00280-8

Foucher, J., Westbrook, G., Boetius, A., Ceramicola, S., Dupré, S., Mascle, J., Mienert, J., Pfannkuche, O., Praeg, D. (2009). Structure and Drivers of Cold Seep Ecosystems. Oceanography, 22(1), 92-109. Retrieved from http://www.jstor.org/stable/24860928

Garcia-Pineda, O., MacDonald, I., Silva, M., Shedd, W., Daneshgar Asl, S., & Schumaker, B. (2016). Transience and persistence of natural hydrocarbon seepage in Mississippi Canyon, Gulf of Mexico. *Deep-Sea Research Part II: Topical Studies in Oceanography*, *129*, 119–129. https://doi.org/10.1016/j.dsr2.2015.05.011

Hammer, Ø., Webb, K. E., & Depreiter, D. (2009). Numerical simulation of upwelling currents in pockmarks, and data from the Inner Oslofjord, Norway. *Geo-Marine Letters*, *29*(4), 269–275. https://doi.org/10.1007/s00367-009-0140-z

Hayes, A. G., Lorenz, R. D., & Lunine, J. I. (2018). A post-Cassini view of Titan's methane-based hydrologic cycle. *Nature Geoscience*, *11*(5), 306–313. https://doi.org/10.1038/s41561-018-0103-y

Hovland, M., & Svensen, H. (2006). Submarine pingoes: Indicators of shallow gas hydrates in a pockmark at Nyegga , Norwegian Sea, *228*, 15–23. https://doi.org/10.1016/j.margeo.2005.12.005

Hudec, M. R., & Jackson, M. P. A. (2007). Terra infirma: Understanding salt tectonics. *Earth-Science Reviews*, *82*(1–2), 1–28. https://doi.org/10.1016/j.earscirev.2007.01.001

Krämer, K., Holler, P., Herbst, G., Bratek, A., Ahmerkamp, S., Neumann, A., Bartholomä, A., van Beusekom, J., Holtappels, M., Winter, C. (2017). Abrupt emergence of a large pockmark field in the German Bight, southeastern North Sea. *Scientific Reports*, *7*(1), 1–8. https://doi.org/10.1038/s41598-017-05536-1

Keller, E. A., Duffy, M., Kennett, J. P., & Hill, T. (2007). Tectonic geomorphology and hydrocarbon induced topography of the Mid-Channel Anticline, Santa Barbara Basin, California. *Geomorphology*, *89*(3–4), 274–286. https://doi.org/10.1016/j.geomorph.2006.12.006

Kinsey, J. C., Yoerger, D. R., Jakuba, M. V, Camilli, R., Fisher, C. R., German, C.R. (2011). Assessing the Deepwater Horizon Oil Spill with the Sentry Autonomous Underwater Vehicle, 261–267

A. J. Kopf, Significance of mud volcanism, Review Geophysics, 40(2), 1005, doi:10.1029/2000RG000093, 2002.

Kvenvolden, K. A., & Lorenson, T. D. (2000). The global occurrence of natural gas hydrate. American Geophysical Union, 3–18.

Kvenvolden, K. A., & Cooper, C. K. (2003). Natural seepage of crude oil into the marine environment. *Geo-Marine Letters*, *23*(3–4), 140–146. https://doi.org/10.1007/s00367-003-0135-0

Loher, M., Marcon, Y., Pape, T., Römer, M., Wintersteller, P., dos Santos Ferreira, C., Praeg, D., Torres, M., Bohrmann, G. (2018). Seafloor sealing, doming, and collapse associated with gas seeps and authigenic carbonate structures at Venere mud volcano, Central Mediterranean. *Deep-Sea Research Part I: Oceanographic Research Papers*, *137*(October 2017), 76–96. https://doi.org/10.1016/j.dsr.2018.04.006

Luo, W. (2000). Quantifying groundwater-sapping landforms with a hypsometric technique. *Journal of Geophysical Research E: Planets*, *105*(E1), 1685–1694. https://doi.org/10.1029/1999JE001096

Masetti, G., Mayer, L., & Ward, L. (2018). A Bathymetry- and Reflectivity-Based Approach for Seafloor Segmentation. *Geosciences*, *8*(1), 14. https://doi.org/10.3390/geosciences8010014

Mayer, L., Jakobsson, M., Allen, G., Dorschel, B., Falconer, R., Ferrini, V., Ferrini, V., Lamarche, G., Snaith, H., Weatherall, P. (2018). The Nippon Foundation—GEBCO Seabed 2030 Project: The Quest to See the World's Oceans Completely Mapped by 2030. *Geosciences*, *8*(2), 63. https://doi.org/10.3390/geosciences8020063

Medialdea, T., Somoza, L., González, F. J., Vázquez, J. T., de Ignacio, C., Sumino, H., Sánchez-Guillamón, Orihashi, Y., León, R., Palomino, D. (2017). Evidence of a modern deep water magmatic hydrothermal system in the Canary Basin (eastern central Atlantic Ocean). *Geochemistry, Geophysics, Geosystems*, *18*(8), 3138–3164. https://doi.org/10.1002/2017GC006889

Milkov, A. V. (2000). Worldwide distribution of submarine mud volcanoes and associated gas hydrates, *167*, 29–42.

Paull, C. K., Normark, W. R., Ussler, W., Caress, D. W., & Keaten, R. (2008). Association among active seafloor deformation, mound formation, and gas hydrate growth and accumulation within the seafloor of the Santa Monica Basin, offshore California. *Marine Geology*, *250*(3–4), 258–275. https://doi.org/10.1016/j.margeo.2008.01.011

Paull, C. K., Caress, D. W., Thomas, H., Lundsten, E., Anderson, K., Gwiazda, R., Riedel, M., McGann, M., Herguera, J. C. (2015). Seafloor geomorphic manifestations of gas venting and shallow subbottom gas hydrate occurrences. *Geosphere*, *11*(2), 491–513. https://doi.org/10.1130/GES01012.1

Picard, K., Radke, L., Williams, D., Nicholas, W., Siwabessy, P., Howard, F., Gaferia, J., Przeslawski, R., Huang, Z., Nichol, S. (2018). Origin of High Density Seabed Pockmark Fields and Their Use in Inferring Bottom Currents. *Geosciences*, *8*(6), 195. https://doi.org/10.3390/geosciences8060195

Pilcher, R., & Argent, J. (2007). Mega-pockmarks and linear pockmark trains on the West African continental margin. *Marine Geology*, *244*(1–4), 15–32. https://doi.org/10.1016/j.margeo.2007.05.002

Reagan, M. T., & Moridis, G. J. (2008). Dynamic response of oceanic hydrate deposits to ocean temperature change. *Journal of Geophysical Research: Oceans*, *113*(12). https://doi.org/10.1029/2008JC004938

Sahling, H., Rickert, D., Lee, R. W., Linke, P., & Suess, E. (2002). Macrofaunal community structure and sulfide flux at gas hydrate deposits from the Cascadia convergent margin, NE Pacific. *Marine Ecology Progress Series*, *231*, 121–138. https://doi.org/10.3354/meps231121

Sahling, H., Borowski, C., Escobar-Briones, E., Gaytán-Caballero, A., Hsu, C. W., Loher, M., …, Bohrmann, G. (2016). Massive asphalt deposits, oil seepage, and gas venting support abundant chemosynthetic communities at the Campeche Knolls, southern Gulf of Mexico. *Biogeosciences*, *13*(15), 4491–4512. https://doi.org/10.5194/bg-13-4491-2016

Schwanghart, W. (2015). Short Communication: TopoToolbox 2 – an efficient and user-friendly tool for Earth surface sciences, (August 2013). https://doi.org/10.5194/esurfd-1-261-2013

Sanchez-Guillamón, O., Vázquez, J. T., Palomino, D., Medialdea, T., Fernández-Salas, L. M., León, R., & Somoza, L. (2018). Morphology and shallow structure of seafloor mounds in the Canary Basin (Eastern Central Atlantic Ocean). *Geomorphology*, *313*, 27–47. https://doi.org/10.1016/j.geomorph.2018.04.007

Sassen, R., Roberts, H. H., Carney, R., Milkov, A. V., DeFreitas, D. A., Lanoil, B., & Zhang, C. (2004). Free hydrocarbon gas, gas hydrate, and authigenic minerals in chemosynthetic communities of the northern Gulf of Mexico continental slope: Relation to microbial processes. *Chemical Geology*, *205*(3–4), 195–217. https://doi.org/10.1016/j.chemgeo.2003.12.032

Sorlien, C. C., Kamerling, M. J., Seeber, L., & Broderick, K. G. (2006). Restraining segments and reactivation of the Santa Monica-Dume-Malibu Coast fault system, offshore Los Angeles, California. *Journal of Geophysical Research: Solid Earth*, *111*(11), 1–22. https://doi.org/10.1029/2005JB003632

Sultan, N., Bohrmann, G., Ruffine, L., Pape, T., Riboulot, V., Colliat, J. L., De Prunelé, A., Dennielou, B., Garzglia, S., Himmler, T., Marsset, T., Peters, C.A., Rabiu, A., Wei, J. (2014). *Journal of Geophysical Research:Solid Earth*, *119*(December 2011), 2679–2694. https://doi.org/10.1029/2010JB007453.Pockmark

Valentine, D. L., Reddy, C. M., Farwell, C., Hill, T. M., Pizarro, O., Yoerger, D. R., Camili, R., Nelson, R.K., Peacock, E.E., Bagby, S.C., Clarke, B.A., Roman, C.N., Soloway, M. (2010). Asphalt volcanoes as a potential source of methane to late Pleistocene coastal waters. *Nature Geoscience*, *3*(5), 345–348. https://doi.org/10.1038/ngeo848

Vanneste, M., Sultan, N., Garziglia, S., Forsberg, C. F., L'Heureux, J. S. (2014). Seafloor instabilities and sediment deformation processes: The need for integrated, multi-disciplinary investigations. *Marine Geology*, *352*, 183–214. https://doi.org/10.1016/j.margeo.2014.01.005

Wynn, R. B., Huvenne, V. A. I., Le Bas, T. P., Murton, B. J., Connelly, D. P., Bett, B. J., Ruhl, H.A., Morris, K.J., Peakall, J., Parsons, D.R., Sumner, E.J., Darby, S.E., Dorrell, R.M., Hunt, J. E. (2014). Autonomous Underwater Vehicles (AUVs): Their past, present and future contributions to the advancement of marine geoscience. *Marine Geology*, *352*, 451–468. https://doi.org/10.1016/j.margeo.2014.03.012

Yun, J. W., Orange, D. L., & Field, M. E. (1999). Subsurface gas offshore of northern California and its link to submarine geomorphology. *Marine Geology*, *154*(1–4), 357–368. https://doi.org/10.1016/S0025-3227(98)00123-6

Appendix

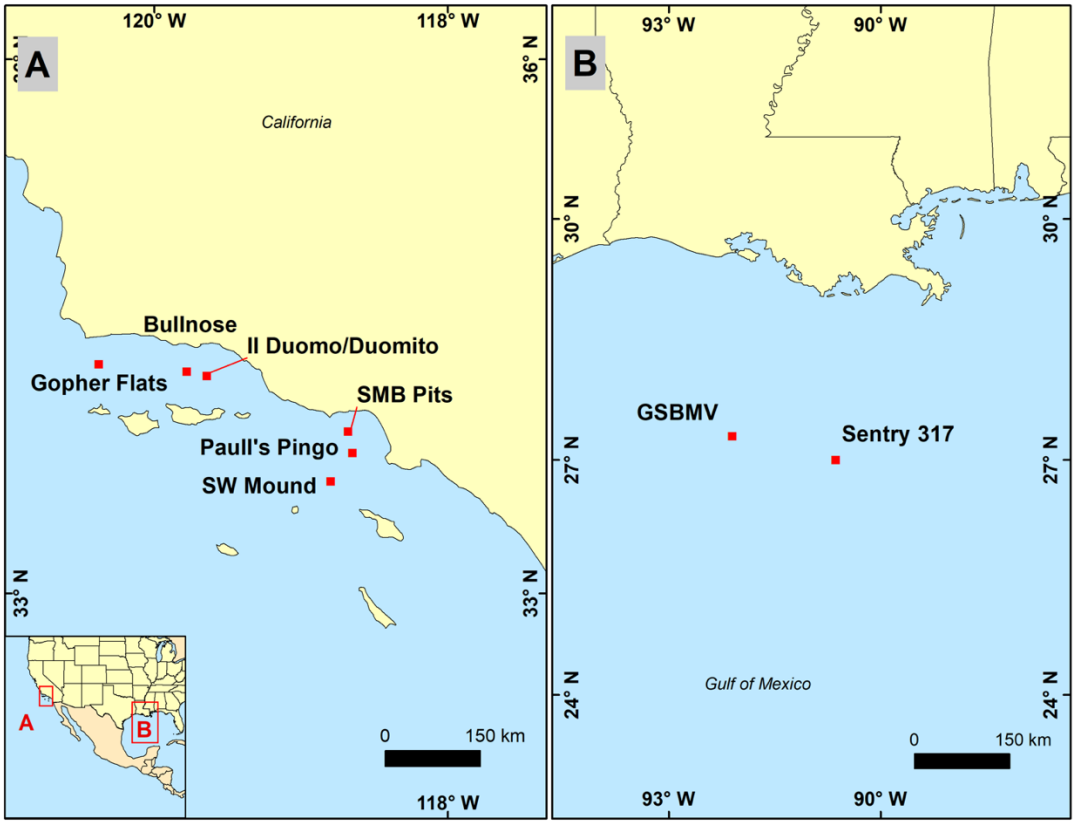

Figure A1-1: An overview of the sites surveyed by AUV Sentry included in this appendix

This appendix consists of various 2D and 3D maps of each survey site in the study. All maps were generated using multibeam data collected from a Reson 7125 Seabat multibeam sonar system and processed using MB-System (Caress et al., 1995) and ArcGIS 10.5. Each map was gridded at a 1-meter resolution. Each site is organized into 2D and 3D map sections, where they begin with an overview of the area, followed by increasingly zoomed-in perspectives. Figures in this appendix are located in the encompassing directory and are all 300 DPI.

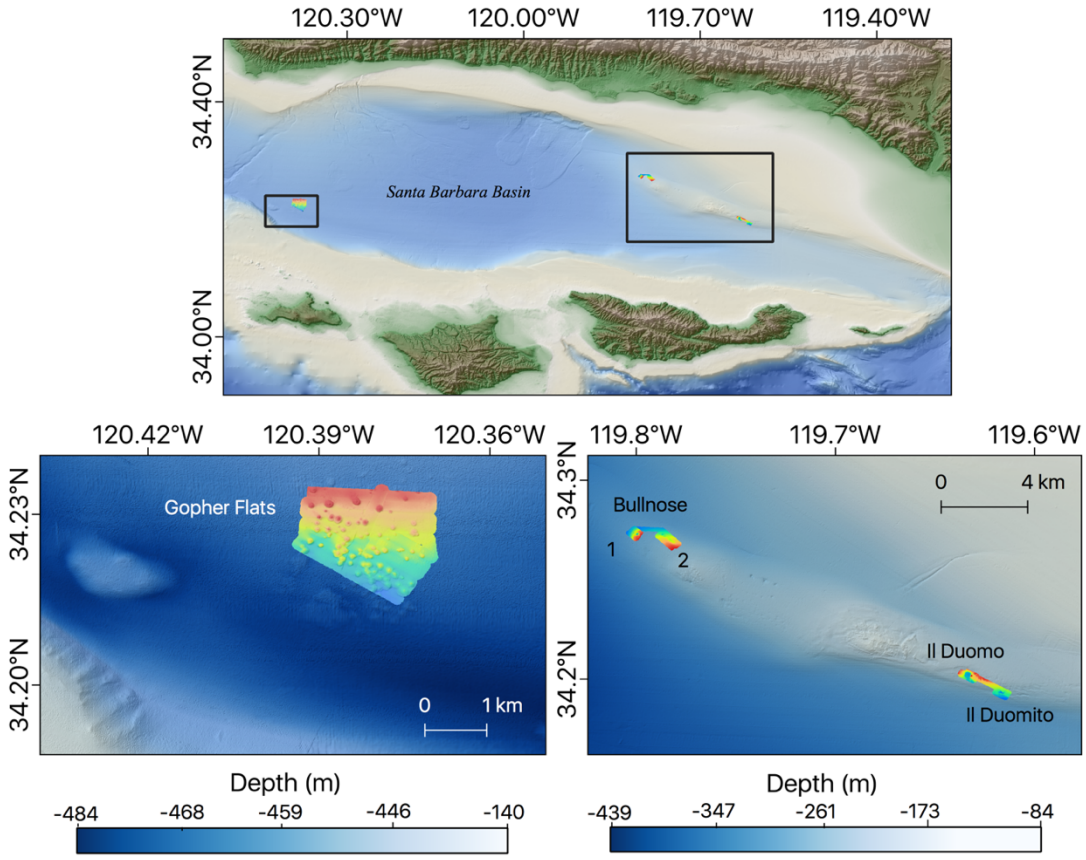

Figure A1-2: Coarse bathymetry for Sentry dives in the Santa Barbara Basin.

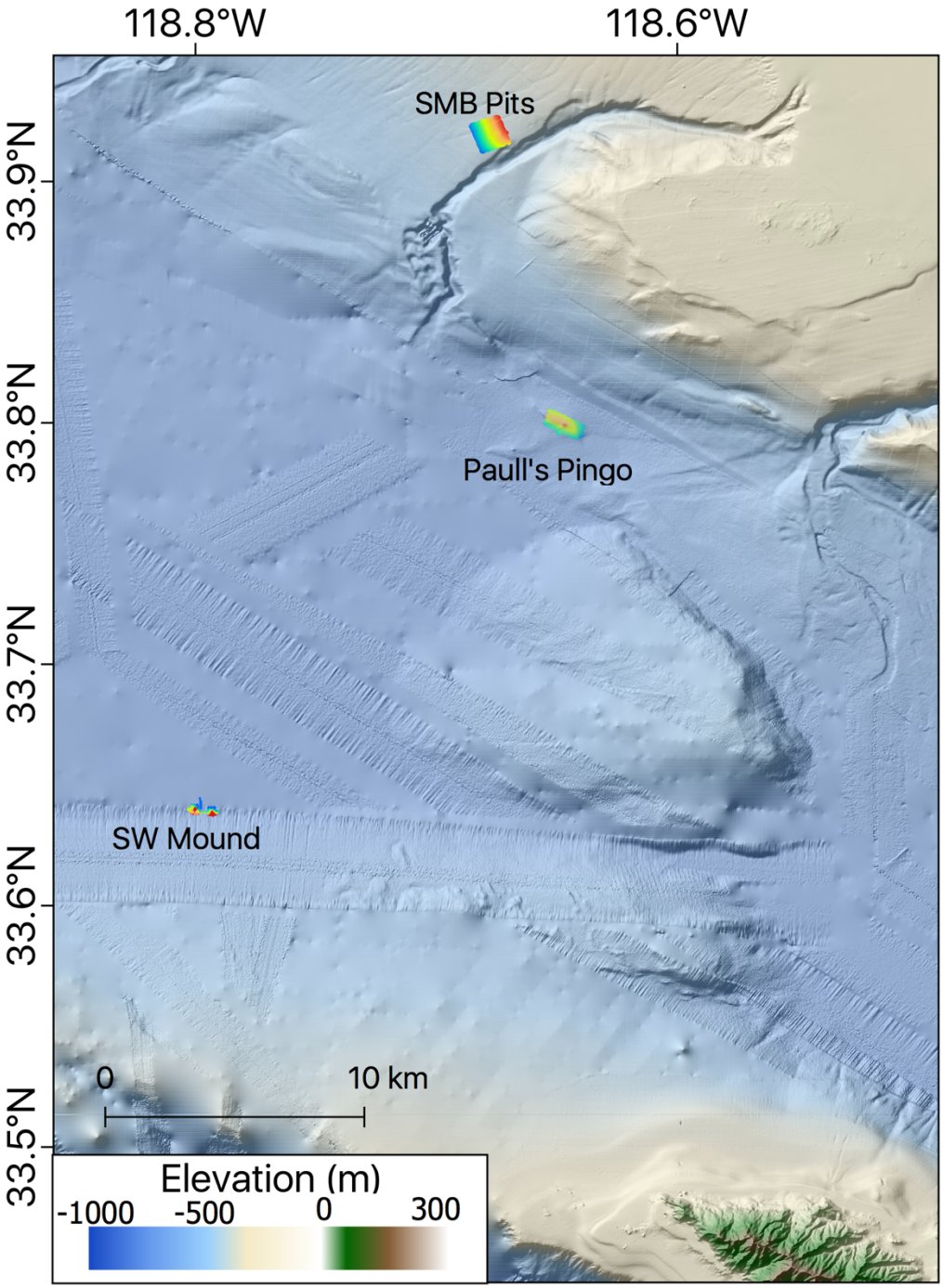

Figure A1-3: Coarse bathymetry for Sentry surveys in the Santa Monica Basin.

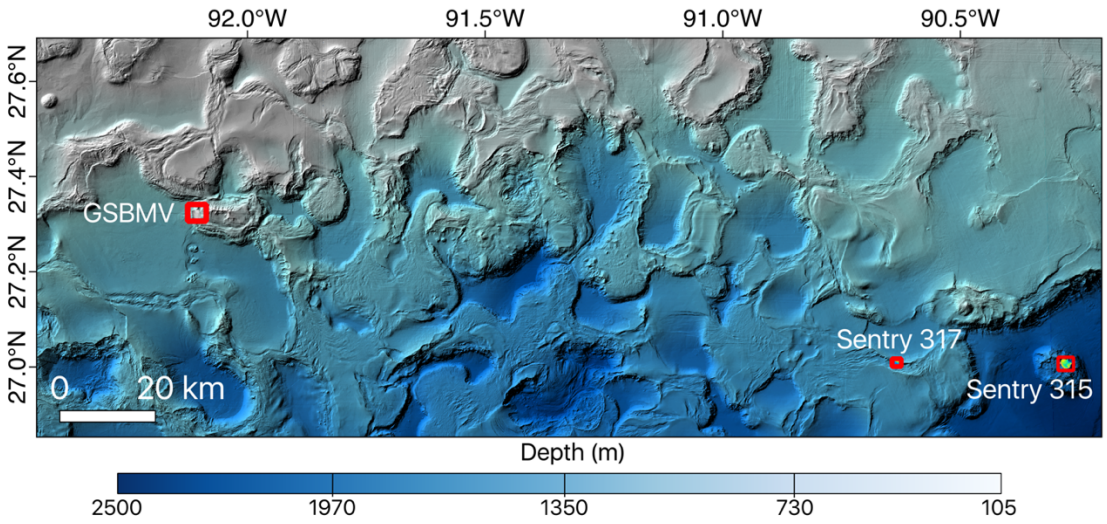

Figure A1-4: Coarse bathymetry of Sentry dives in the Gulf of Mexico

TABLE OF CONTENTS: APPENDIX

Elevated Hydrocarbon Induced Terrains

Gopher Flats (Sentry 118)

Gopher Flats was surveyed on 09/19/11 between 00:15 and 09:16. 54 mounds were delineated at this site. Mounds consist of extruded oil and typically have a relief of 4-5 meters and are 100-130 meters in diameter.

Gopher Flats	
Source	Oil
Activity	Dormant
Count	54
Depth (m)	439 - 464
Major Axis (m)	134 ± 41
Minor Axis (m)	103 ± 30
Length/Width	1.30 ± 0.15
Relief (m)	5.3 ± 1.8
Basal Area (10^3 m^2)	11.37 ± 6.08
Volume (10^3 m^3)	39.3 ± 29.5
Average Slope (°)	4.4 ± 0.8
Area/Relief (10^3 m)	2.04 ± 0.7
HI	0.56 ± 0.06

2D Maps

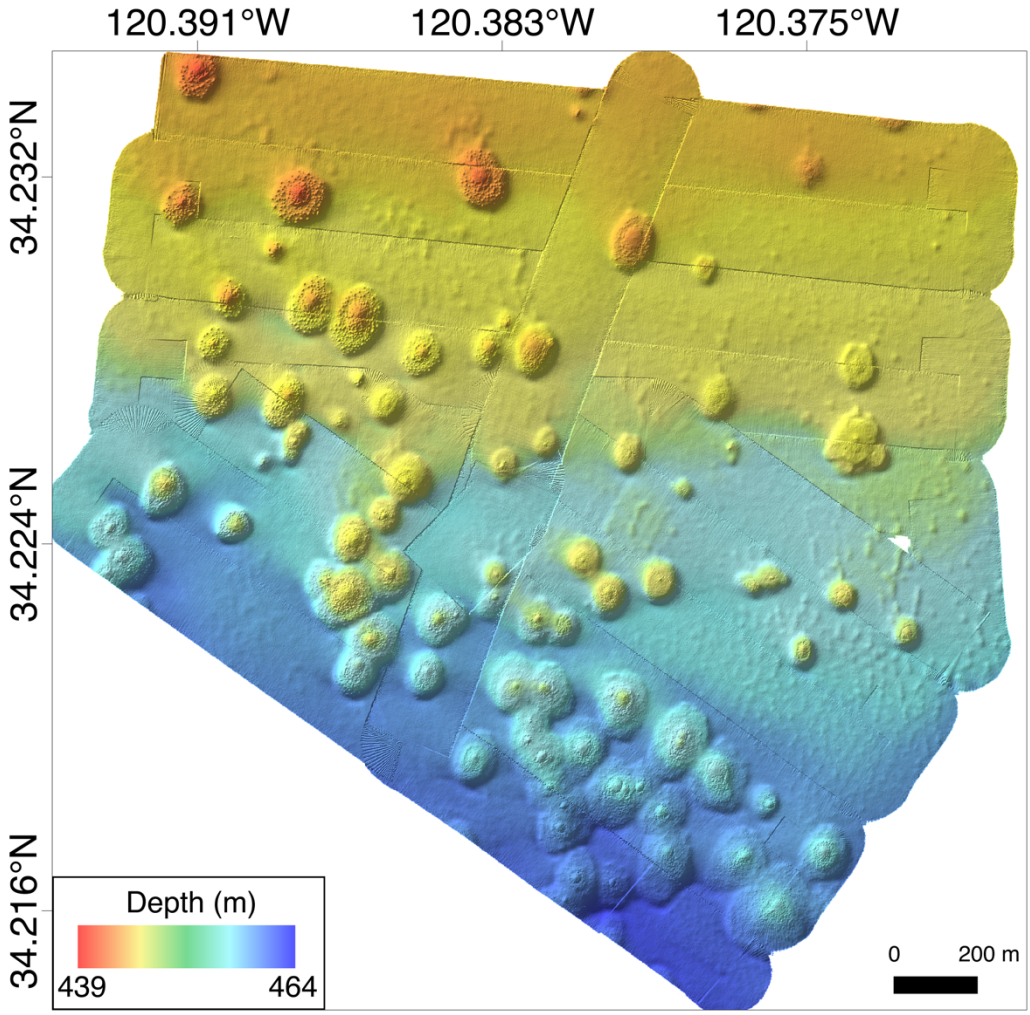

Figure A2-1: An overview of oil mounds at Gopher Flats

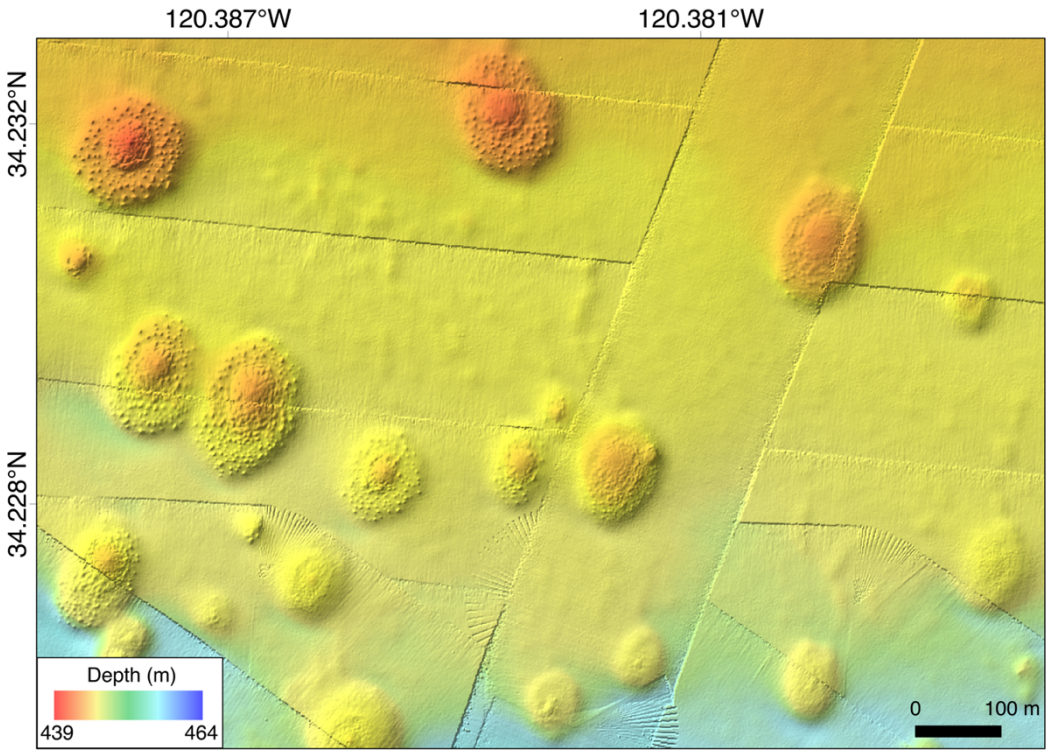

Figure A2-2: Zoomed in view of northern mounds

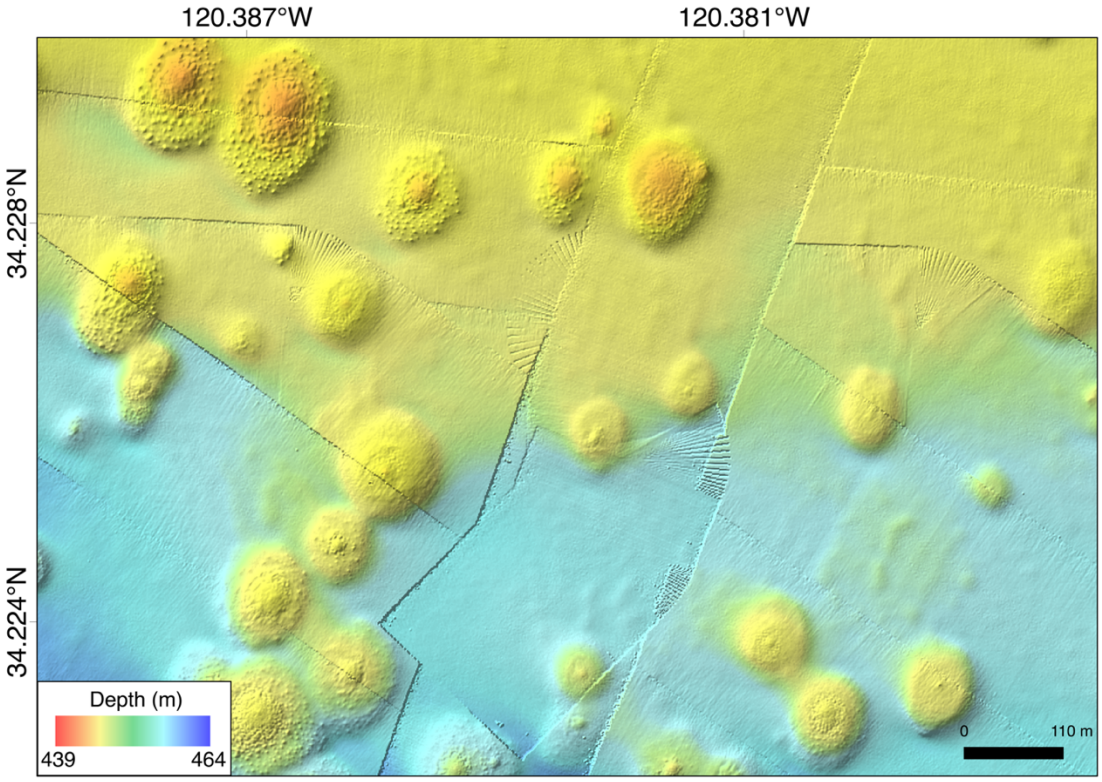

Figure A2-3: Zoomed in view of middle section

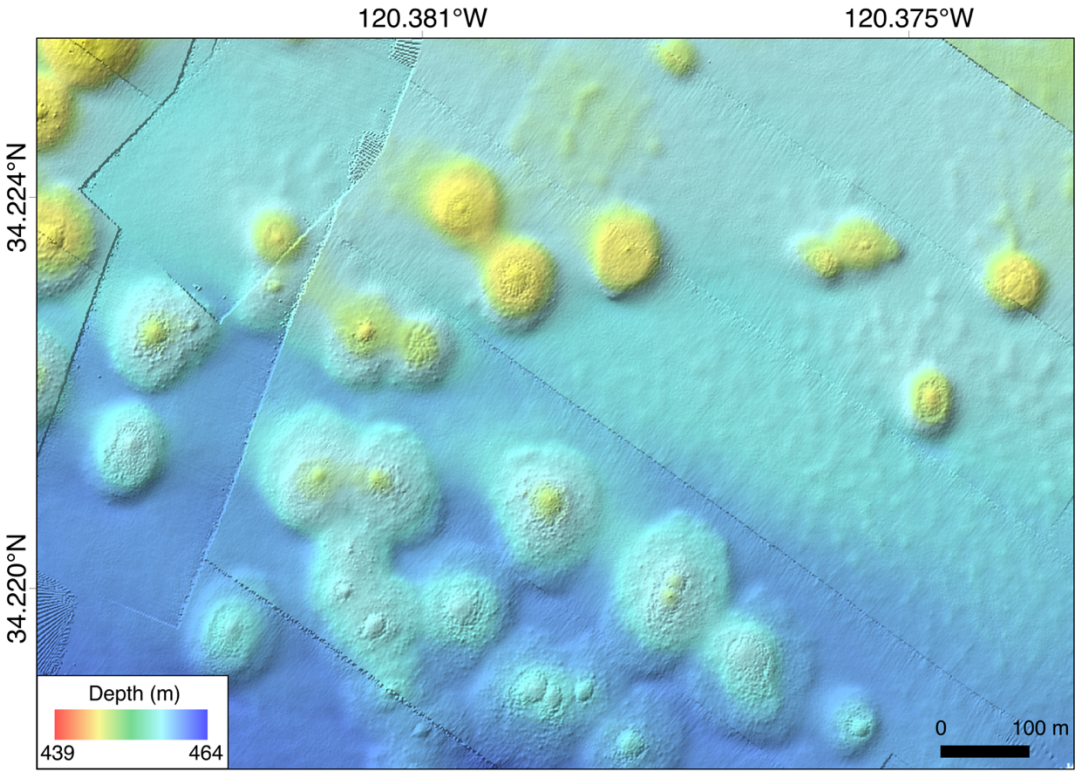

Figure A2-4: Zoomed in perspective of amalgamated southern mounds

Individual Mounds

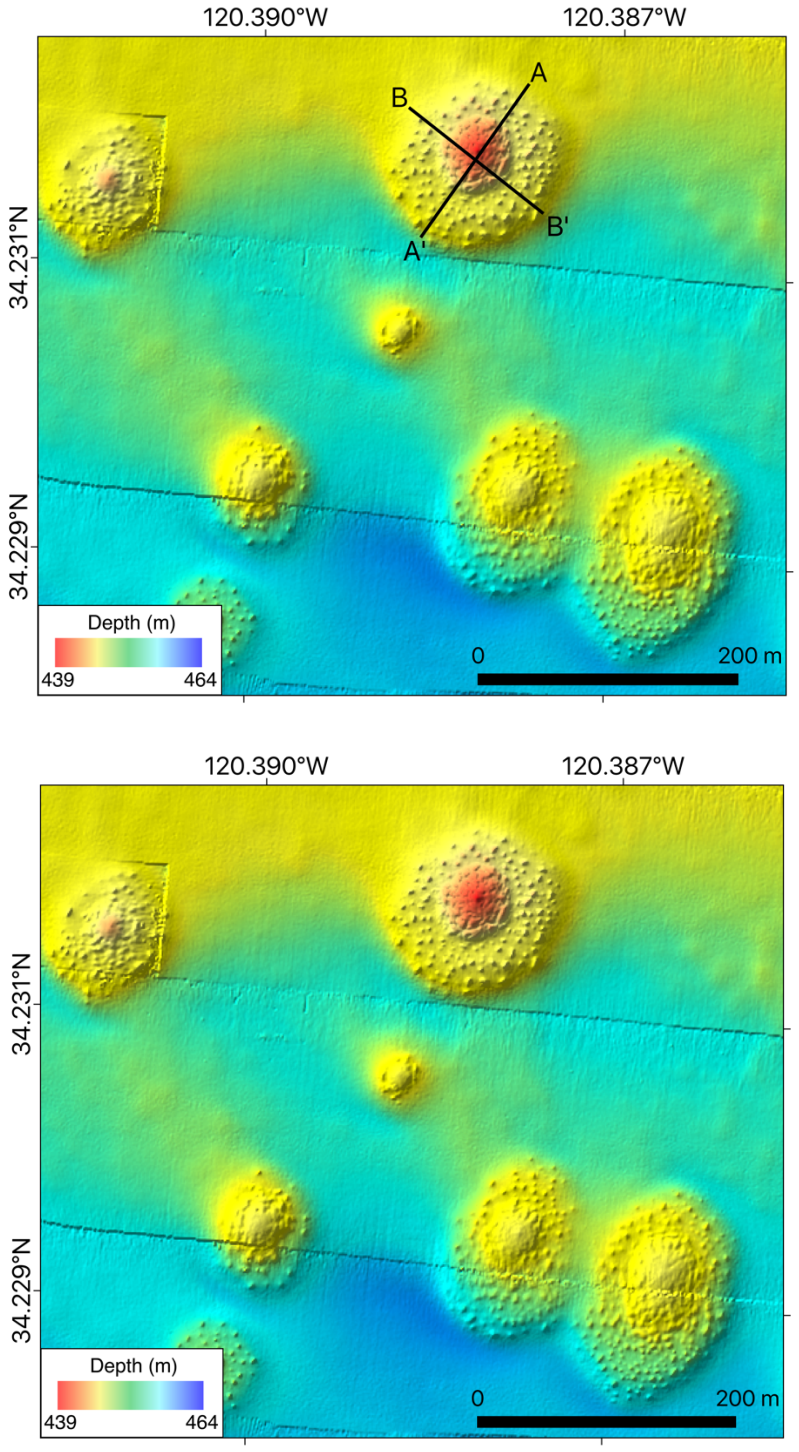

Figure A3-1: Oil mounds at Gopher Flats. They are peppered with smaller oil mounds about 1 meter across.

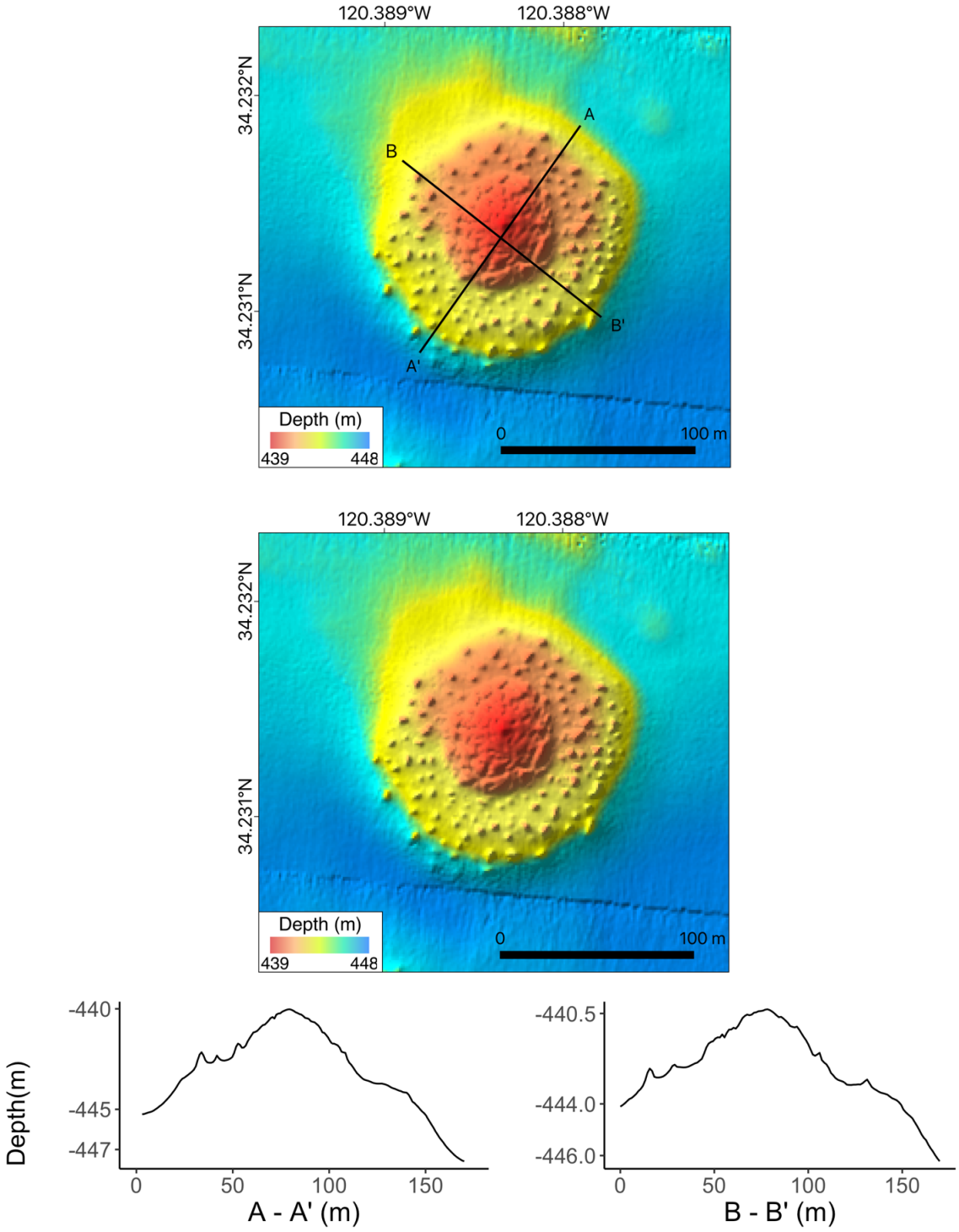

Figure A3-2: Oil mound at Gopher Flats, showing a summit and a base

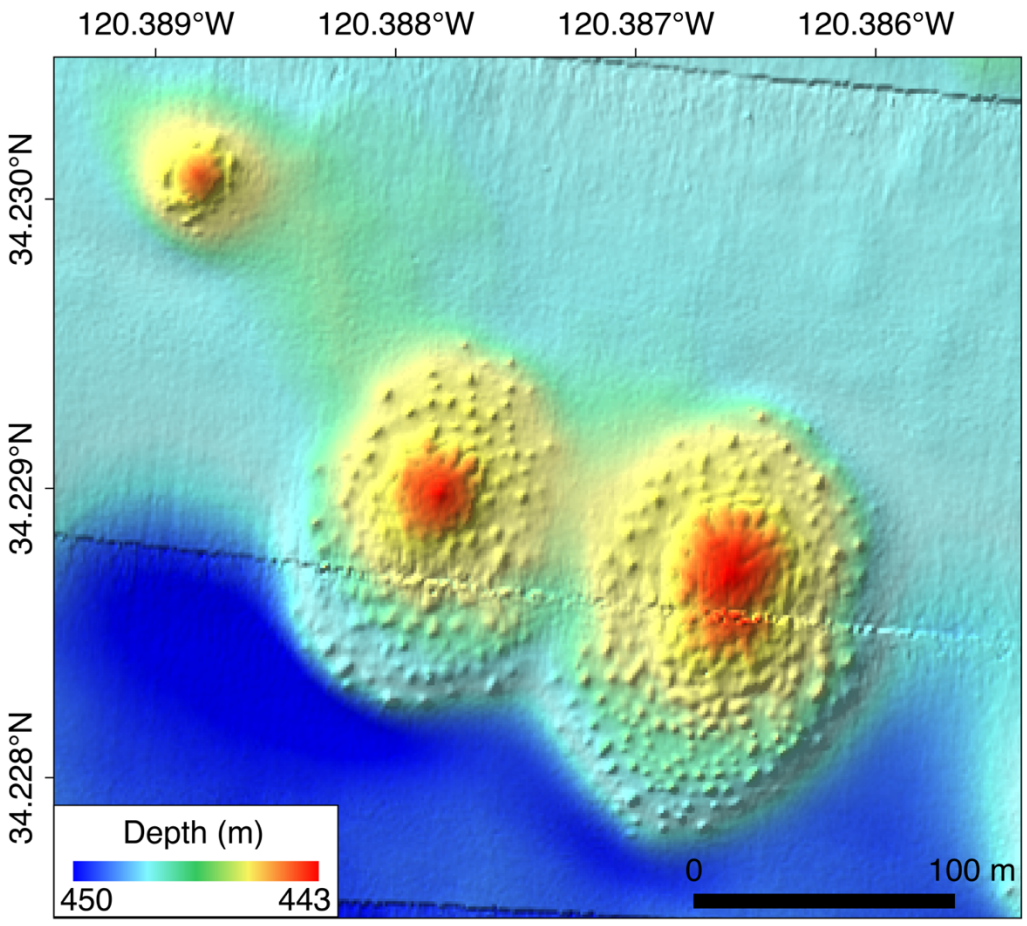

Figure A3-3: Two nearly amalgamated oil mounds at Gopher Flats

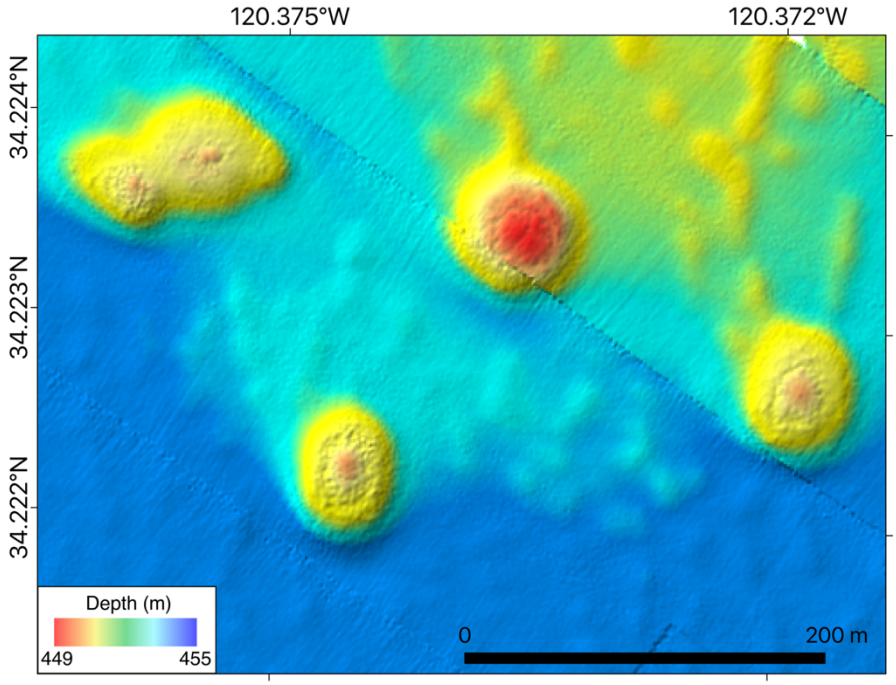

Figure A3-4: Irregular mounds on the southeastern section of the survey site

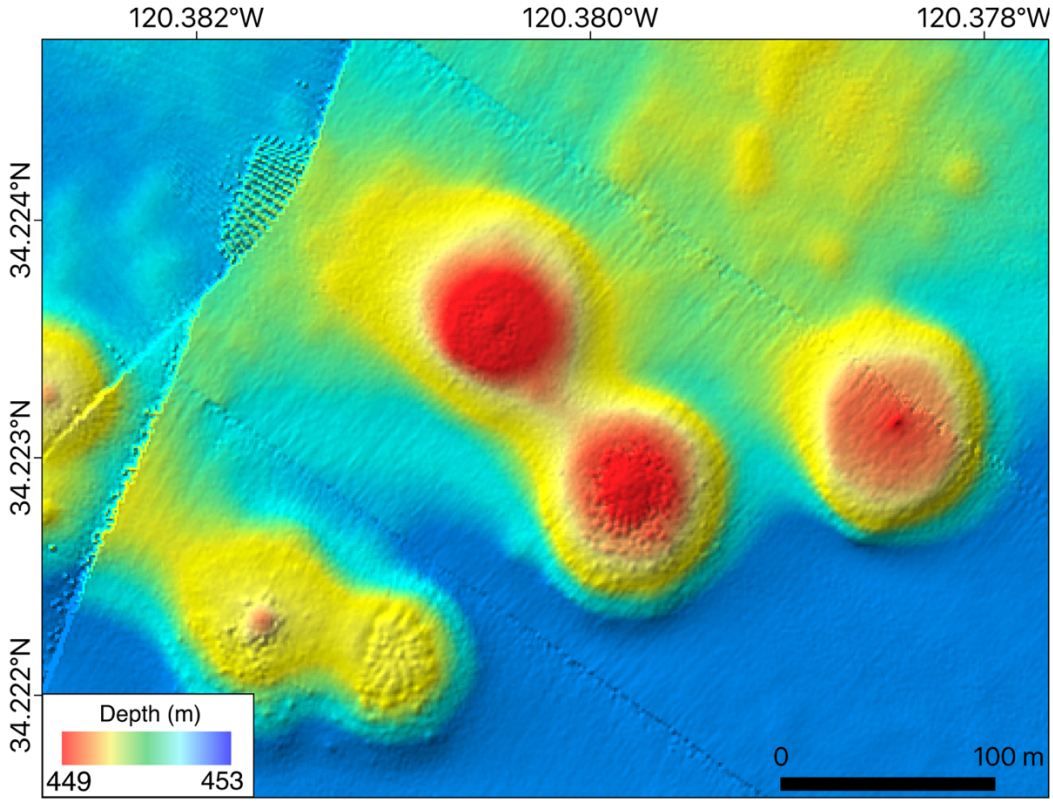

Figure A3-5: Irregular mounds on the southeastern section of the Gopher Flats survey site

3D Maps

These maps are displayed at 5x vertical exaggeration. The same color ramp is used from 2D maps.

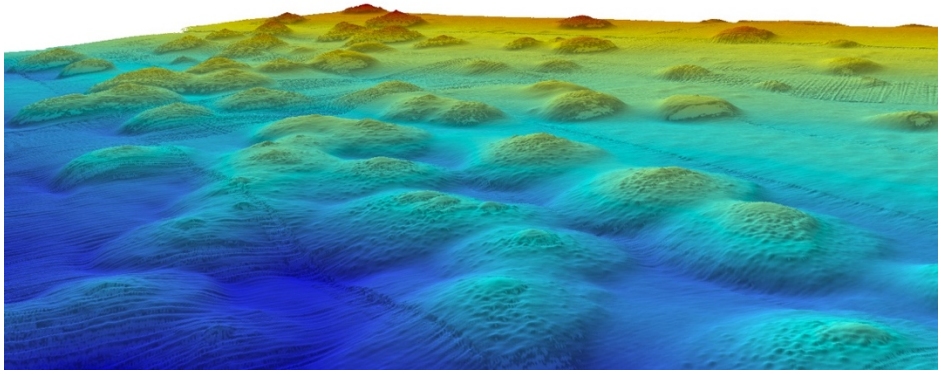

Figure A4-1: 3D perspective of Gopher Flats from the SE

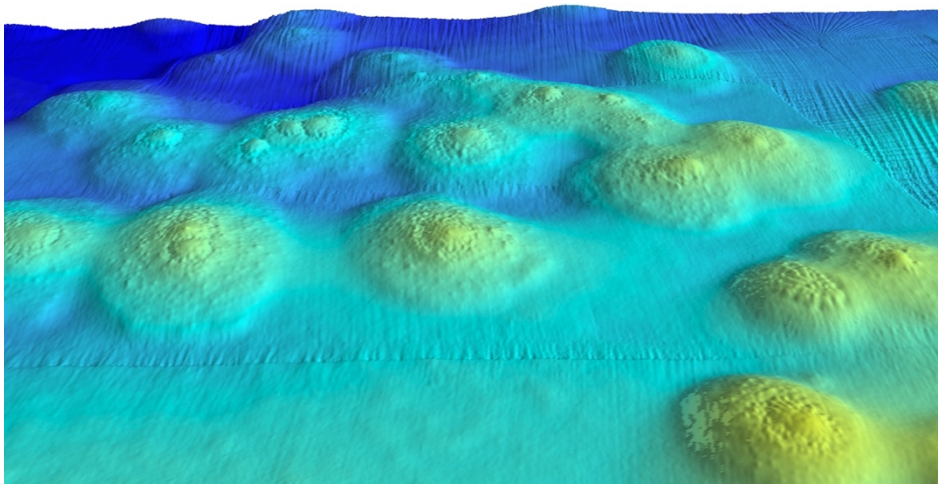

Figure A4-2: 3D perspective of amalgamated mounds in the southern section of the survey area

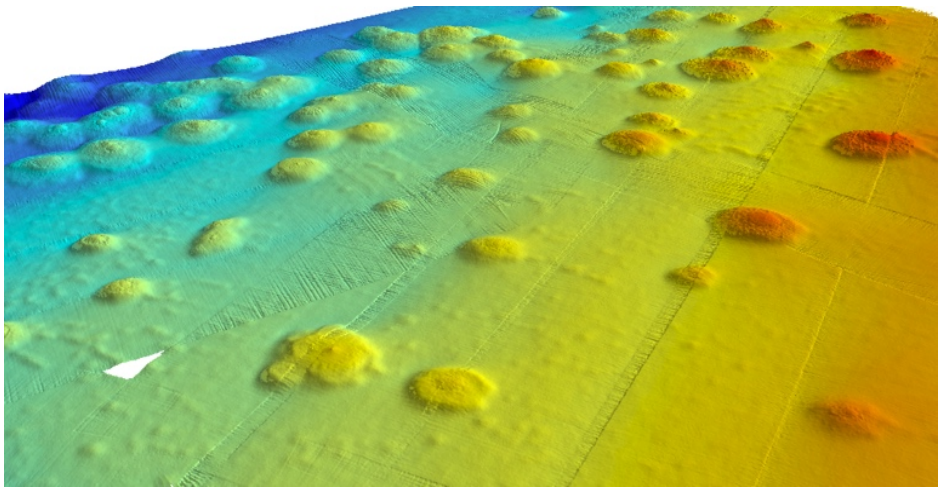

Figure A4-3: 3D perspective of Gopher Flats from the NE

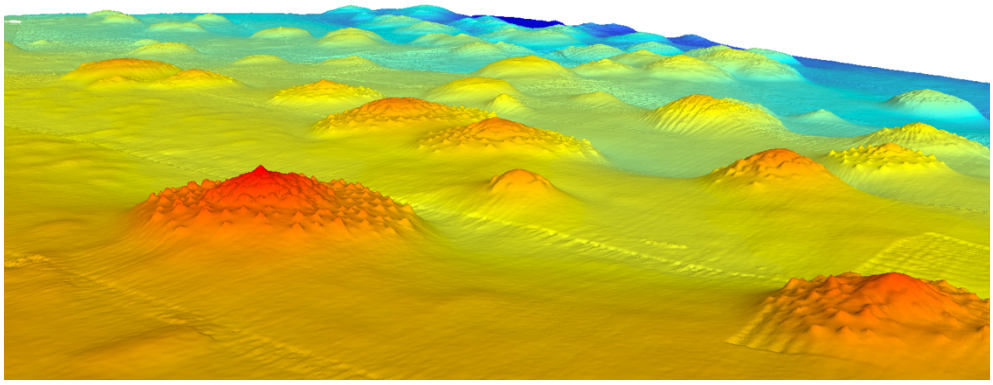

Figure A4-4: View from NNW. Mound in the bottom left of the figure is the same mound shown in figure A3-2

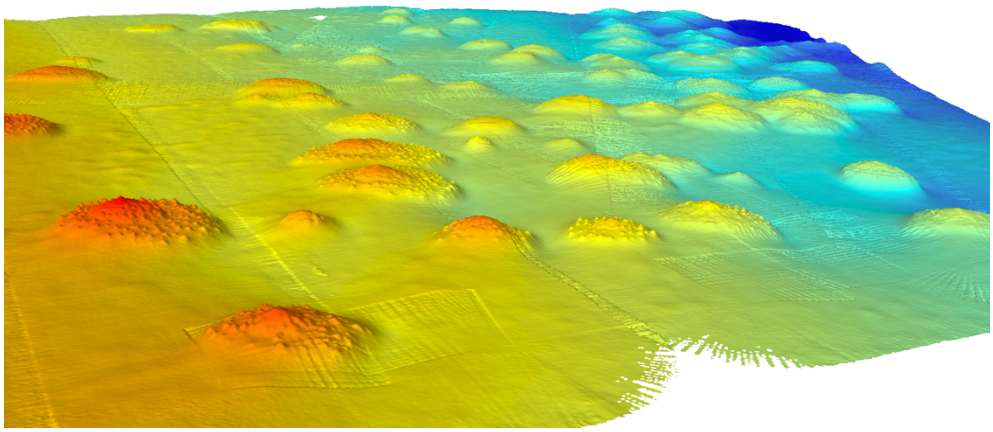

Figure A4-5: View from the west.

Il Duomo (Sentry 031)

Il Duomo was surveyed during Sentry031 on 09/19/09 between 01:58 and 02:35. It is an asphalt volcano that is about 120 meters in diameter and has 24.5 meters of relief. The neighboring depression is about 200 meters in diameter and about 50 meters deep.

Il Duomo	
Source	Oil
Activity	Dormant
Count	1
Depth (m)	152 - 218
Major Axis (m)	121
Minor Axis (m)	113
Length/Width	1.07
Relief (m)	24.5
Basal Area (10^3 m^2)	10.45
Volume (10^3 m^3)	147.2
Average Slope (°)	21.2
Area/Relief (10^3 m)	0.43
HI	0.57

2D Maps

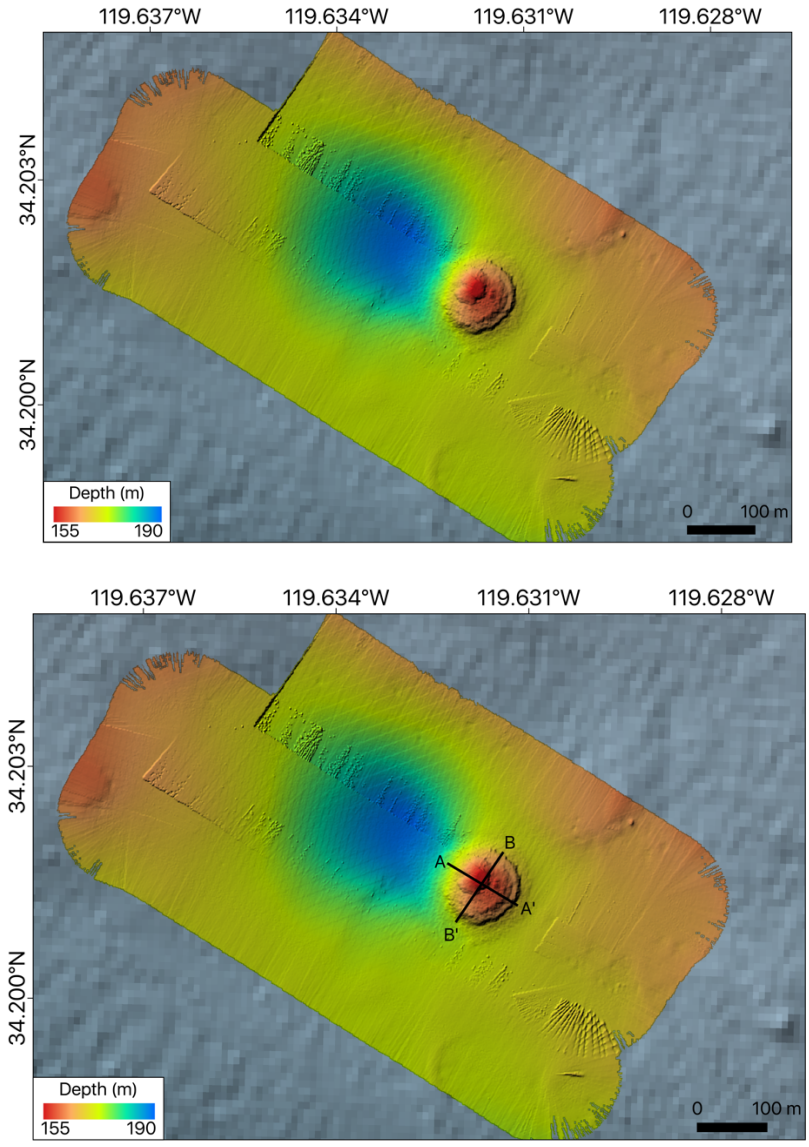

Figure A5-1: An overview of the Il Duomo survey area, with and without cross-sections

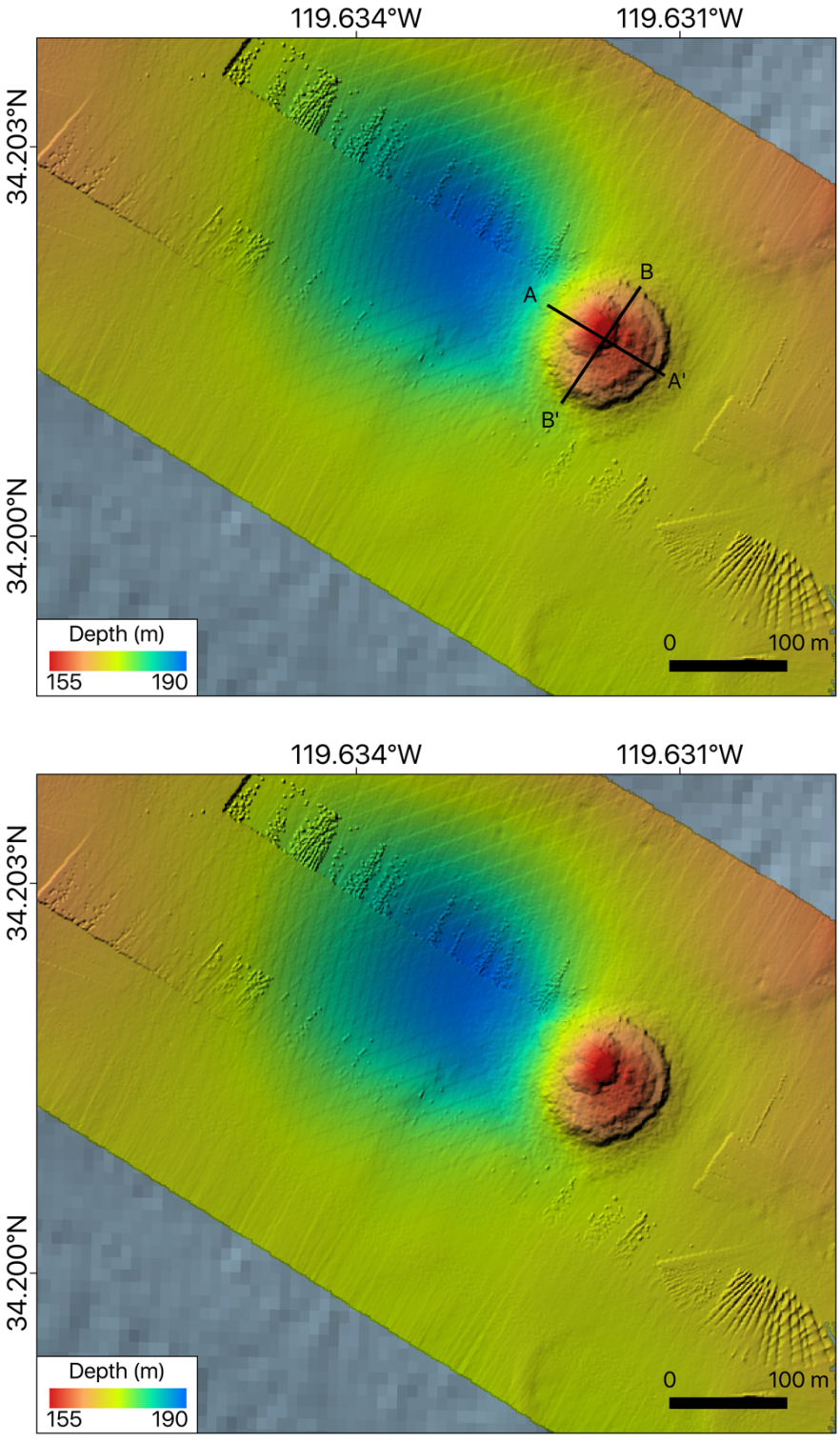

Figure A5-2: Slight zoom of Il Duomo

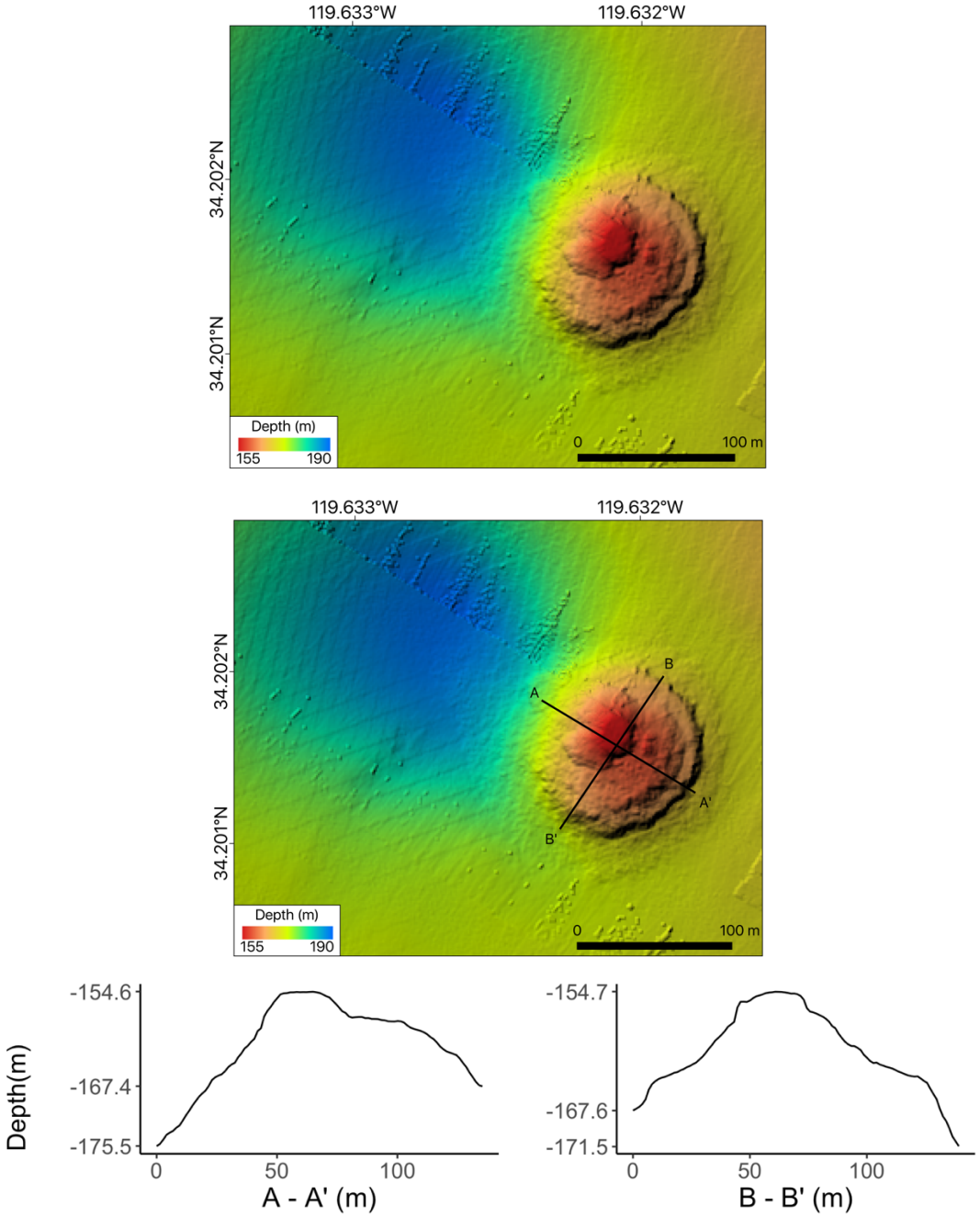

Figure A5-3: Full zoom of Il Duomo

3D Maps

These 3D perspectives were made at 7x vertical exaggeration.

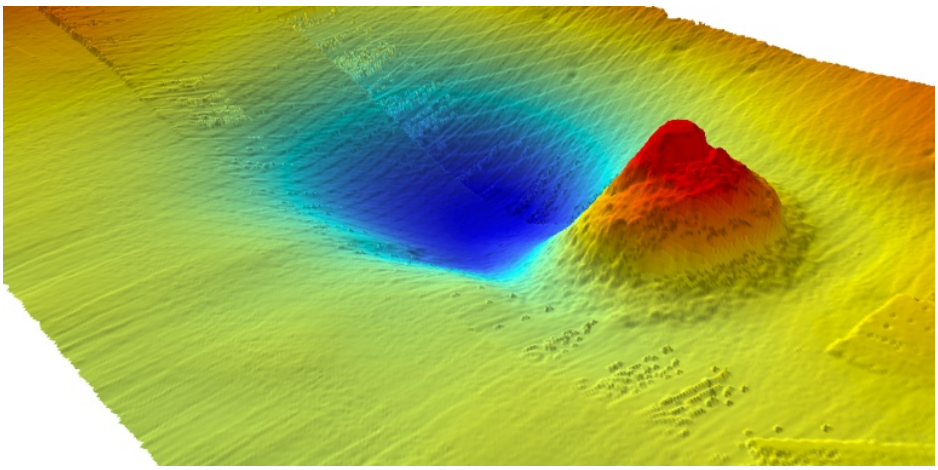

Figure A6-1: View of Il Duomo from the southeast

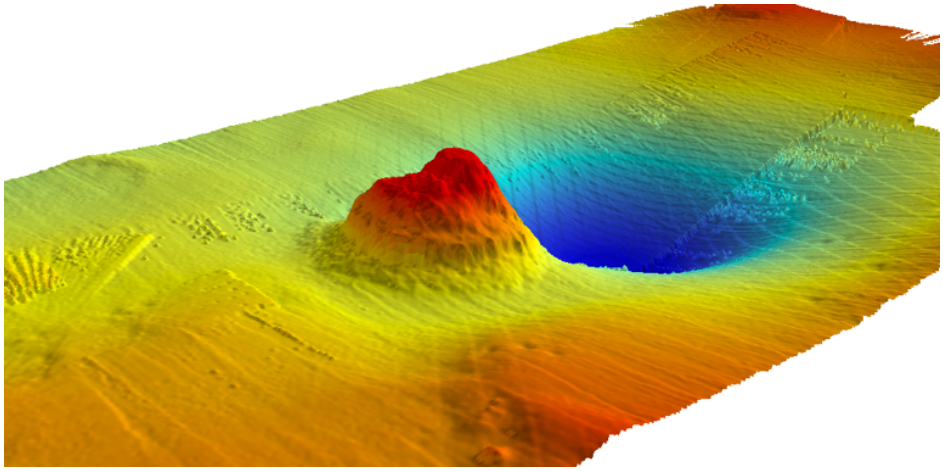

Figure A6-2: View of Il Duomo from northeast

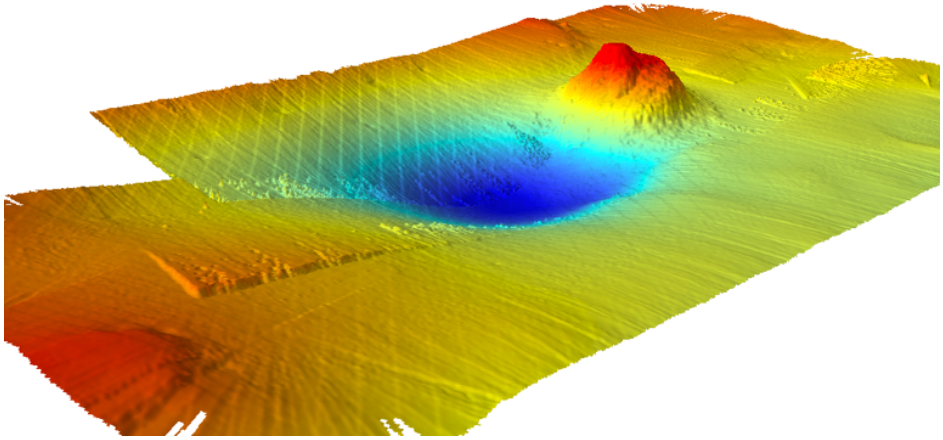

Figure A6-3: View of Il Duomo from northwest

Il Duomito (Sentry 031)

Il Duomito was surveyed by AUV Sentry between 12:32 and 13:30 on 09/19/09. It is the second block of Sentry 031.

Il Duomito	
Source	Oil
Activity	Dormant
Count	6
Depth (m)	184 - 214
Major Axis (m)	79 ± 32
Minor Axis (m)	59 ± 21
Length/Width	1.33 ± 0.10
Relief (m)	12.7 ± 6.3
Basal Area (10^3 m^2)	3.97 ± 2.87
Volume (10^3 m^3)	30.06 ± 29.46
Average Slope (°)	16.7 ± 5.1
Area/Relief (10^3 m)	0.3 ± 0.17
HI	0.58 ± 0.08

2D Maps

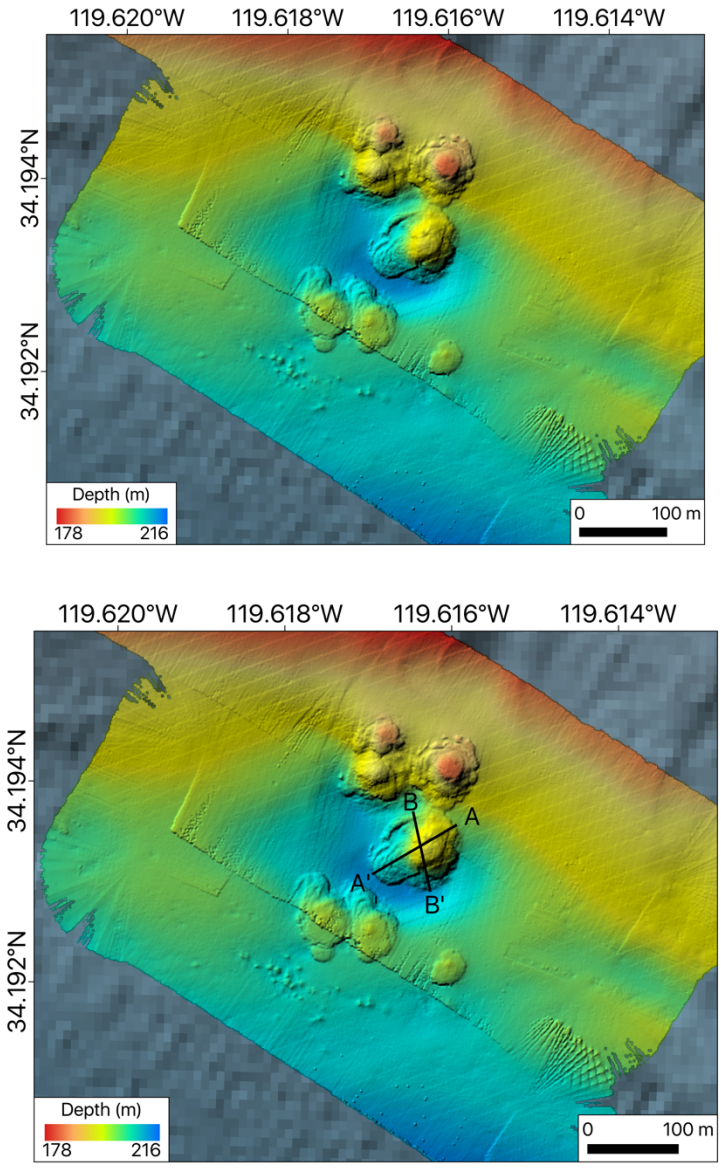

Figure A7-1: An overview of dormant asphalt volcanoes at Il Duomito

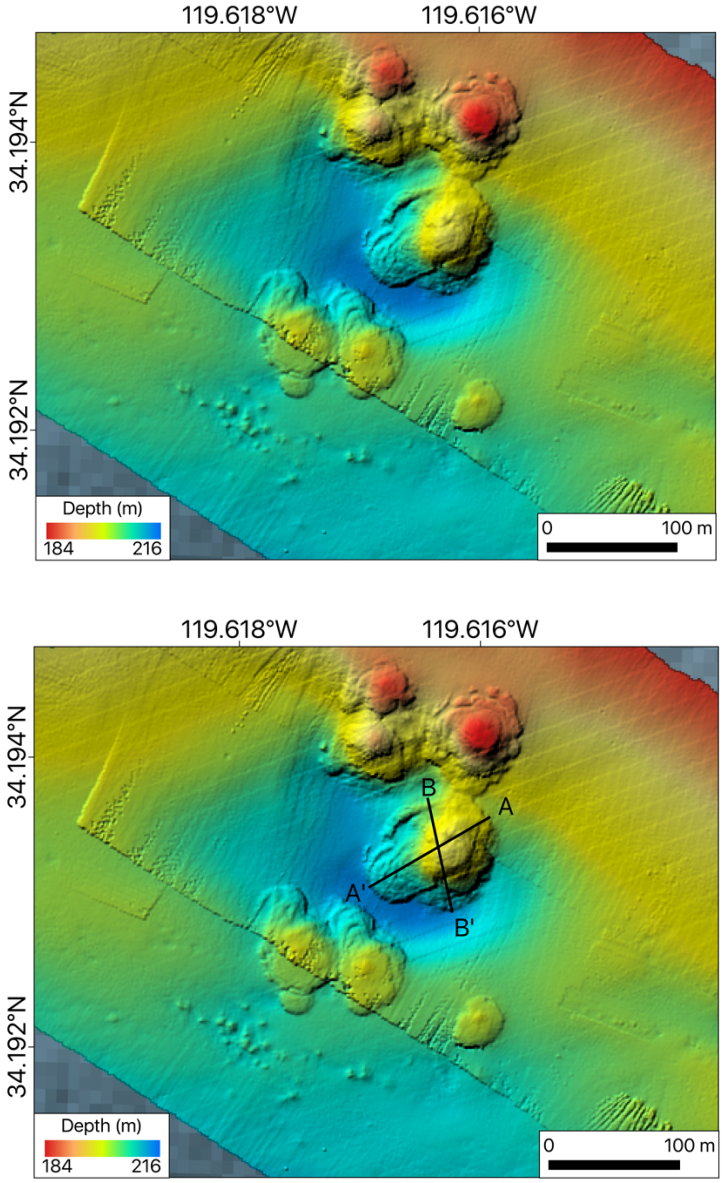

Figure A7-2: Slight zoom of asphalt volcanoes at Il Duomito

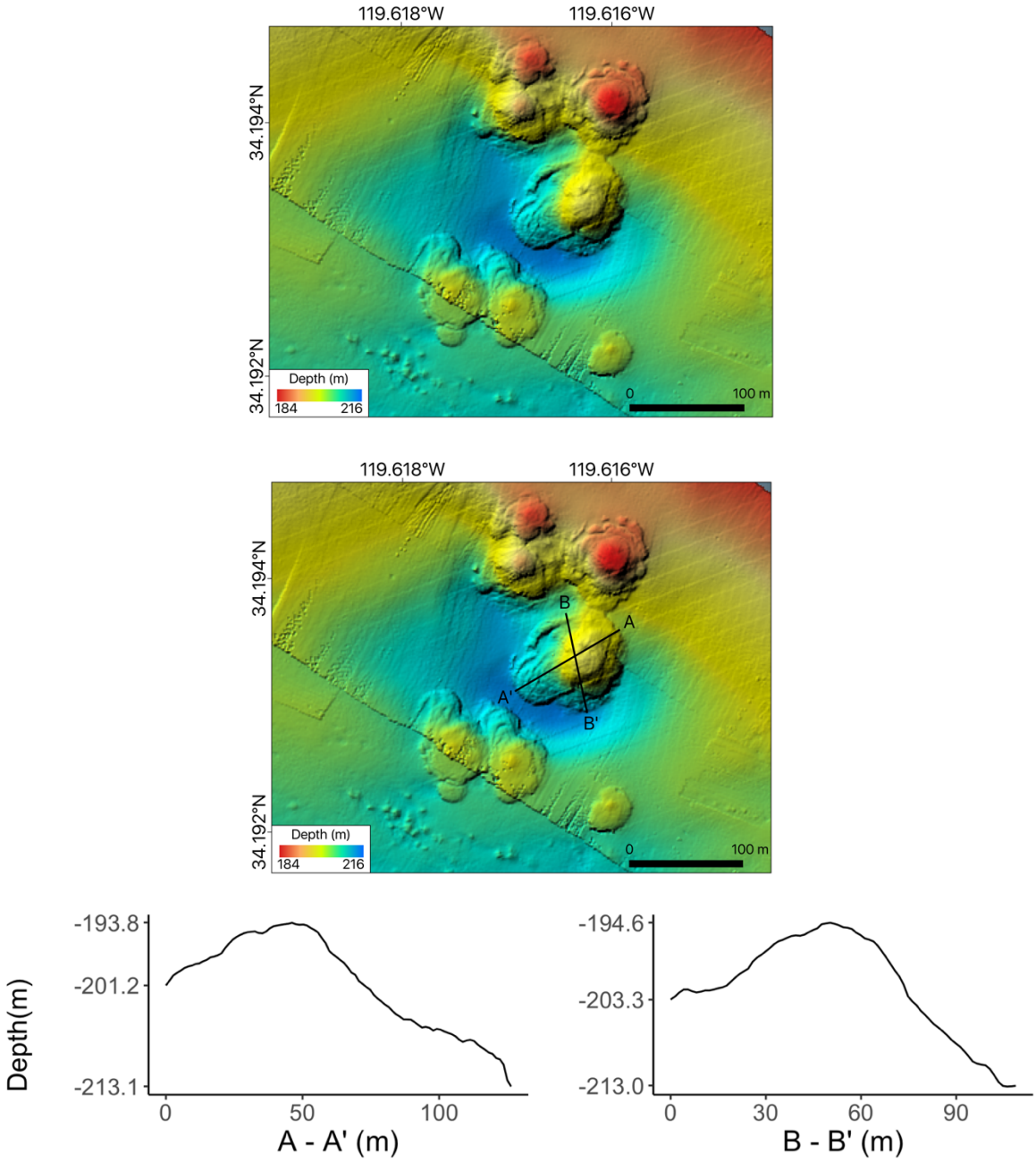

Figure A7-3: Full zoom of dormant asphalt volcanoes at Il Duomito

3D Maps

These 3D perspectives are displayed at 7x vertical exaggeration.

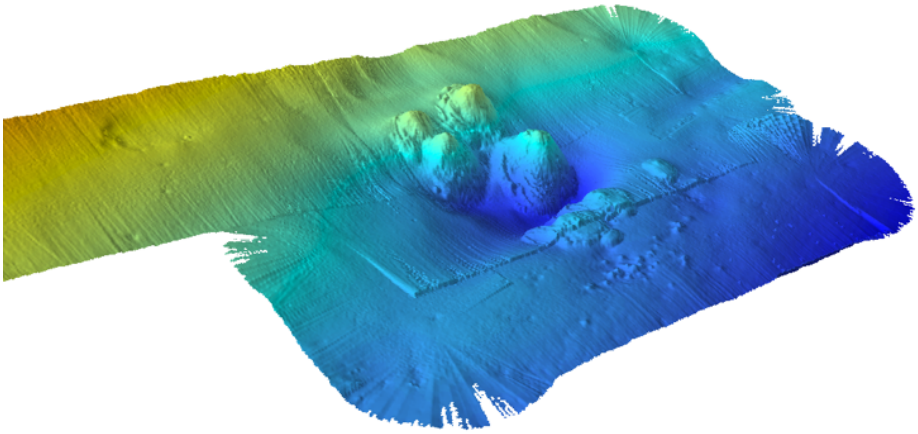

Figure A8-1: View from the southwest

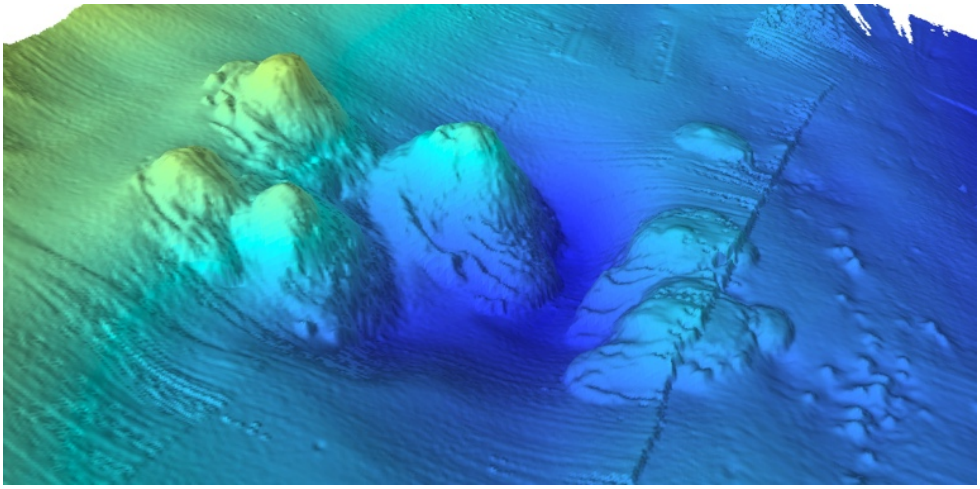

Figure A8-2: Zoomed in view from the west

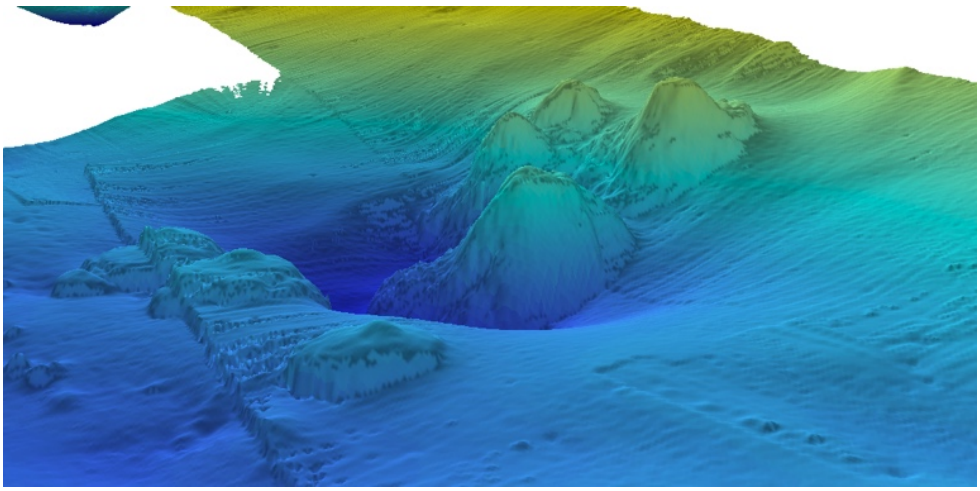

Figure A8-3: View from the east

Paull's Pingo (Sentry 036)

Paull's Pingo was surveyed in 2009, 2011 (Sentry 120), and 2013 (Sentry 203). The maps below were generated using data collected on 09/27/09, between 02:15 and 05:13. It is located on a bathymetric swell and some degree of slumping is present on the southwestern flank.

Paull's Pingo	
Source	Gas Hydrate
Activity	Active
Count	1
Depth (m)	803 - 845
Major Axis (m)	255
Minor Axis (m)	206
Length/Width	1.58
Relief (m)	33.4
Basal Area (10^3 m^2)	40.09
Volume (10^3 m^3)	877.57
Average Slope (°)	11.3
Area/Relief (10^3 m)	1.2
HI	0.5

2D Maps

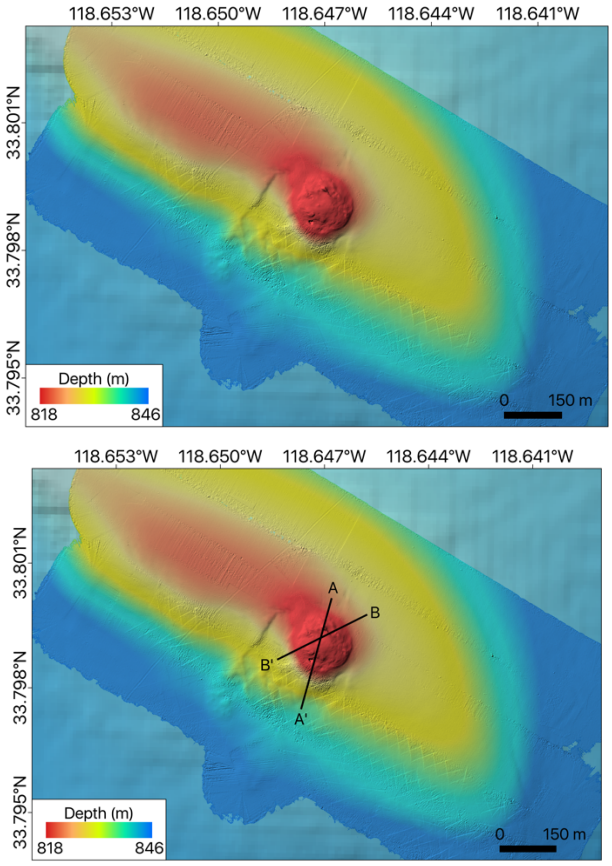

Figure A9-1: An overview of Paull's Pingo, with and without cross-sections

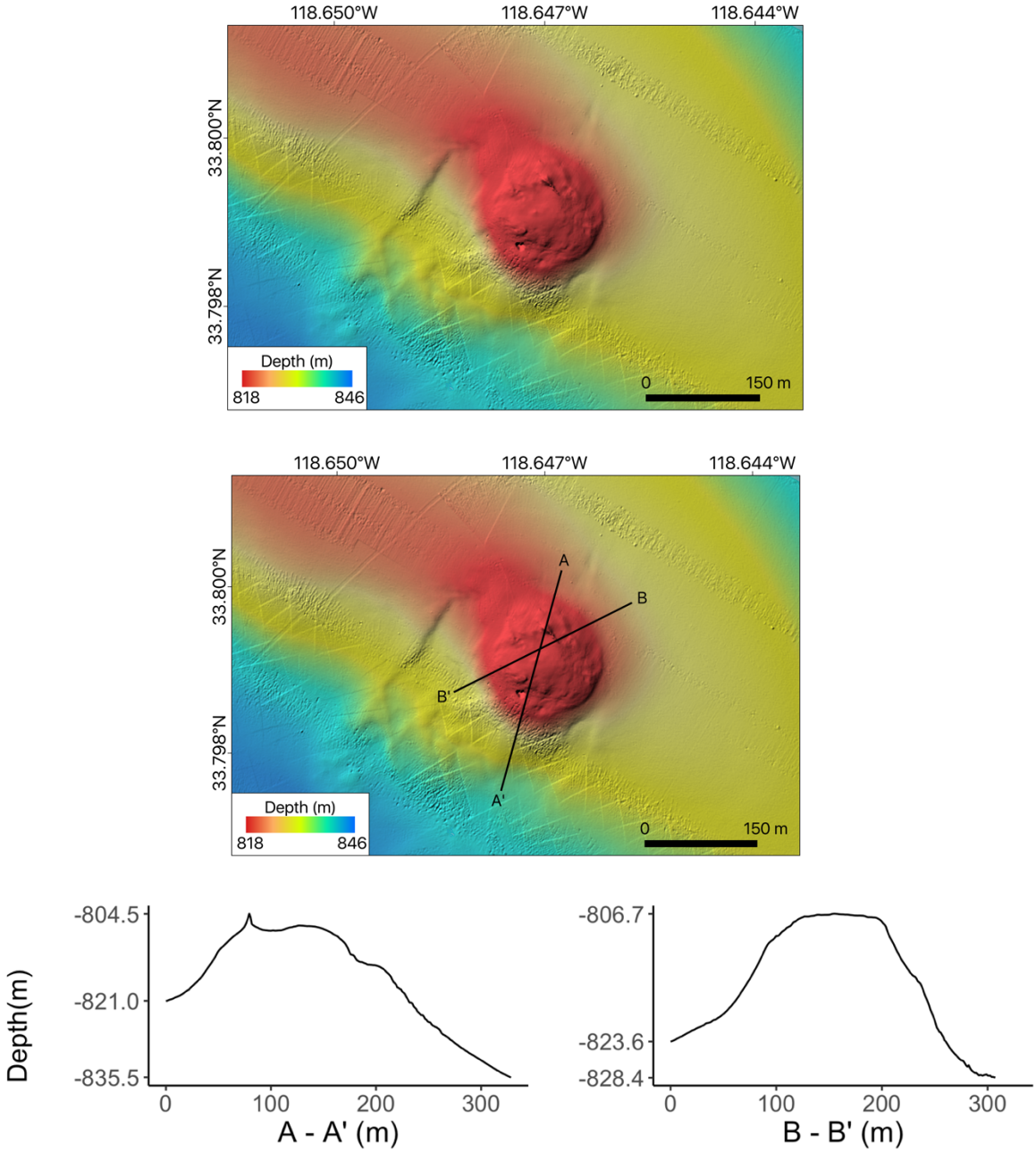

Figure A9-2: A zoomed in perspective, with and without cross-sections. A 20 m carbonate ridge can be seen on the northern side of the feature

3D Maps

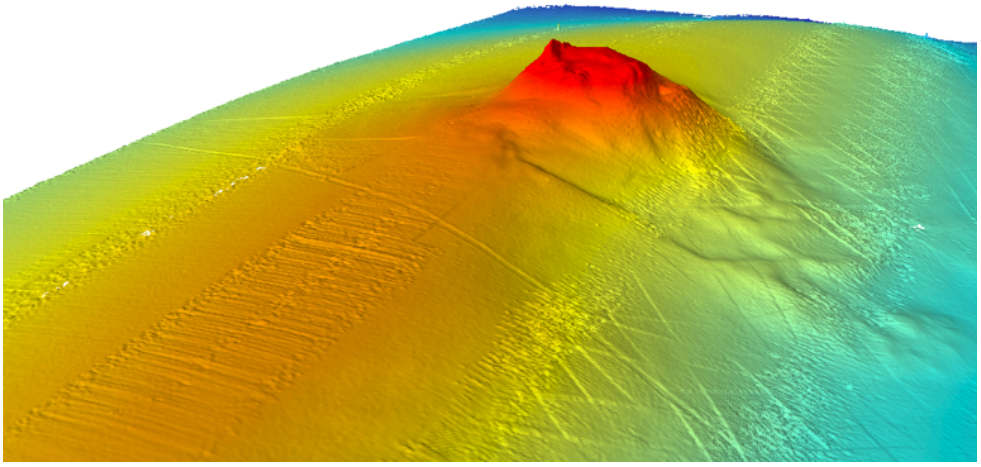

Figure A10-1: 3D perspective from the northwest

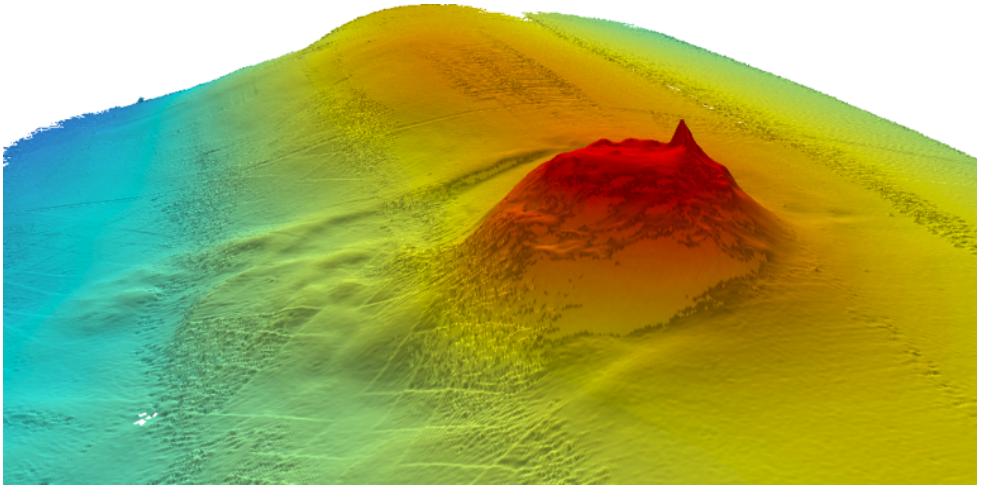

Figure A10-2: 3D perspective from the southeast

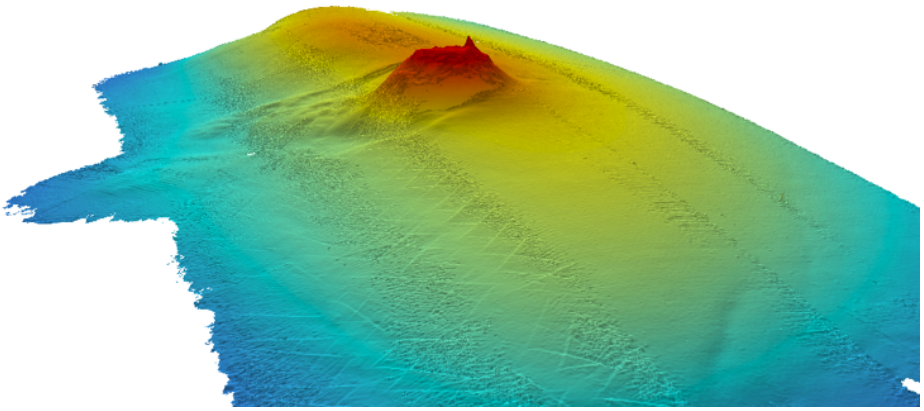

Figure A10-3: Zoomed out perspective from southeast

Southwest Mound (Sentry 199)

Southwest Mound was surveyed 09/29/13 - 09/30/13 between 23:12 and 01:42.

SW Mound	
Source	Gas Hydrate
Activity	Active
Count	1
Depth (m)	893 - 898
Major Axis (m)	188
Minor Axis (m)	119
Length/Width	1.28
Relief (m)	4.0
Basal Area (10^3 m^2)	16.25
Volume (10^3 m^3)	19.84
Average Slope (°)	3.9
Area/Relief (10^3 m)	4.06
HI	0.3

2D Maps

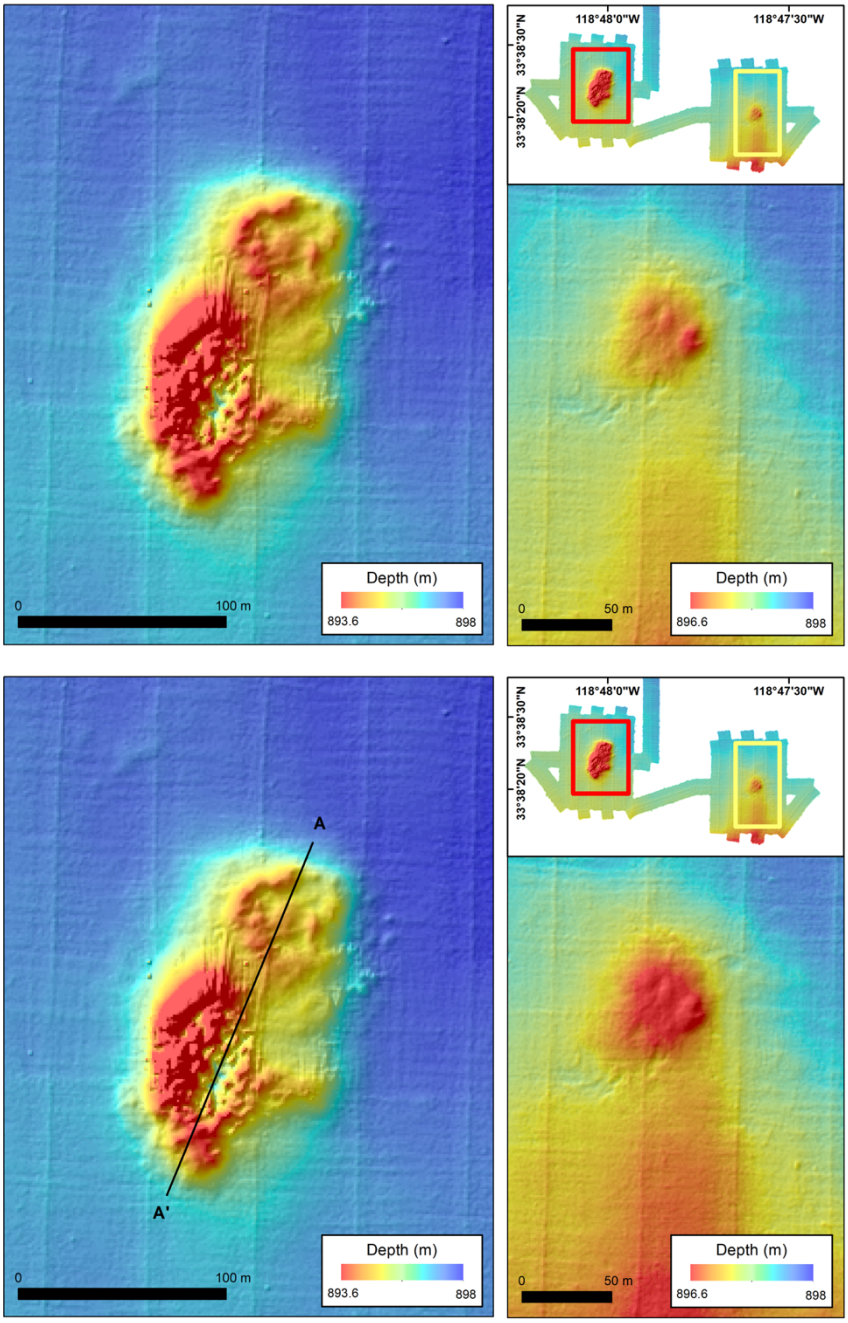

Figure A11-1: An overview of the Southwest Mounds site. The smaller mound on the right did not have a high enough slope for delineation.

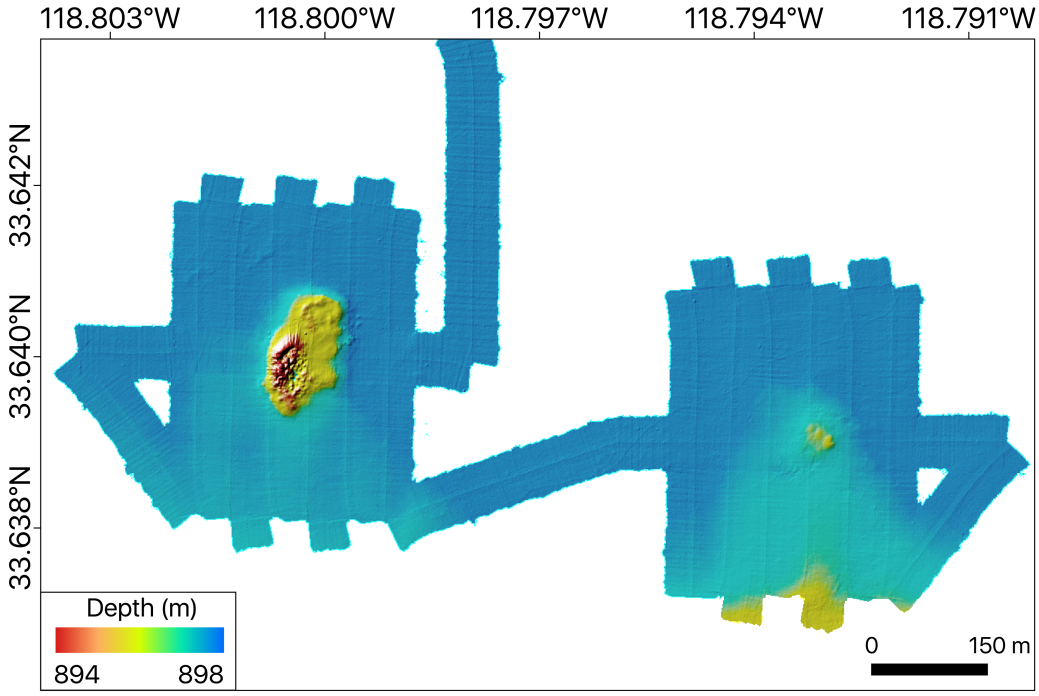

Figure A11-2: An overview of the Southwest Mounds site

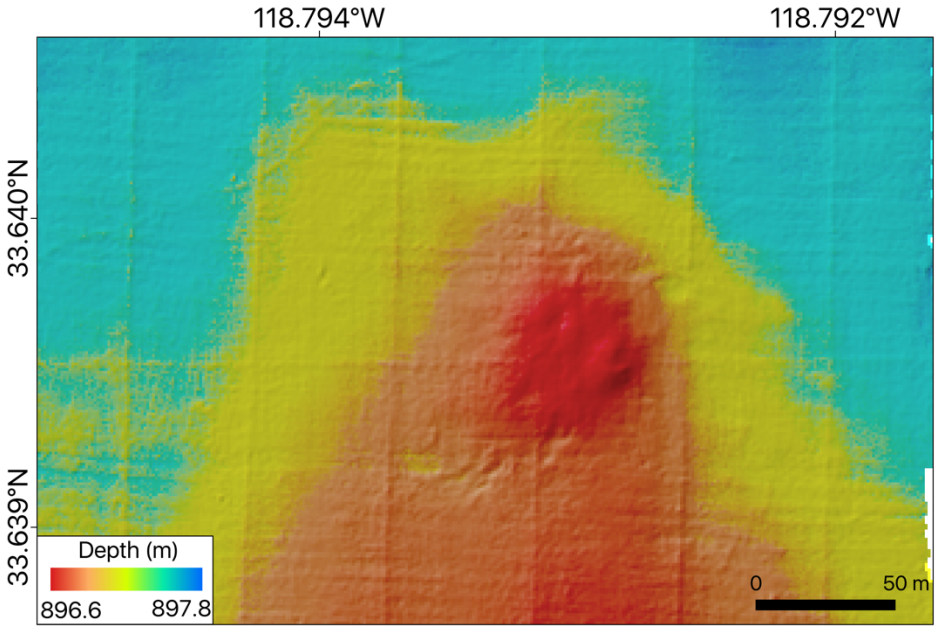

Figure A11-3: Eastern mound at Southwest Mound site

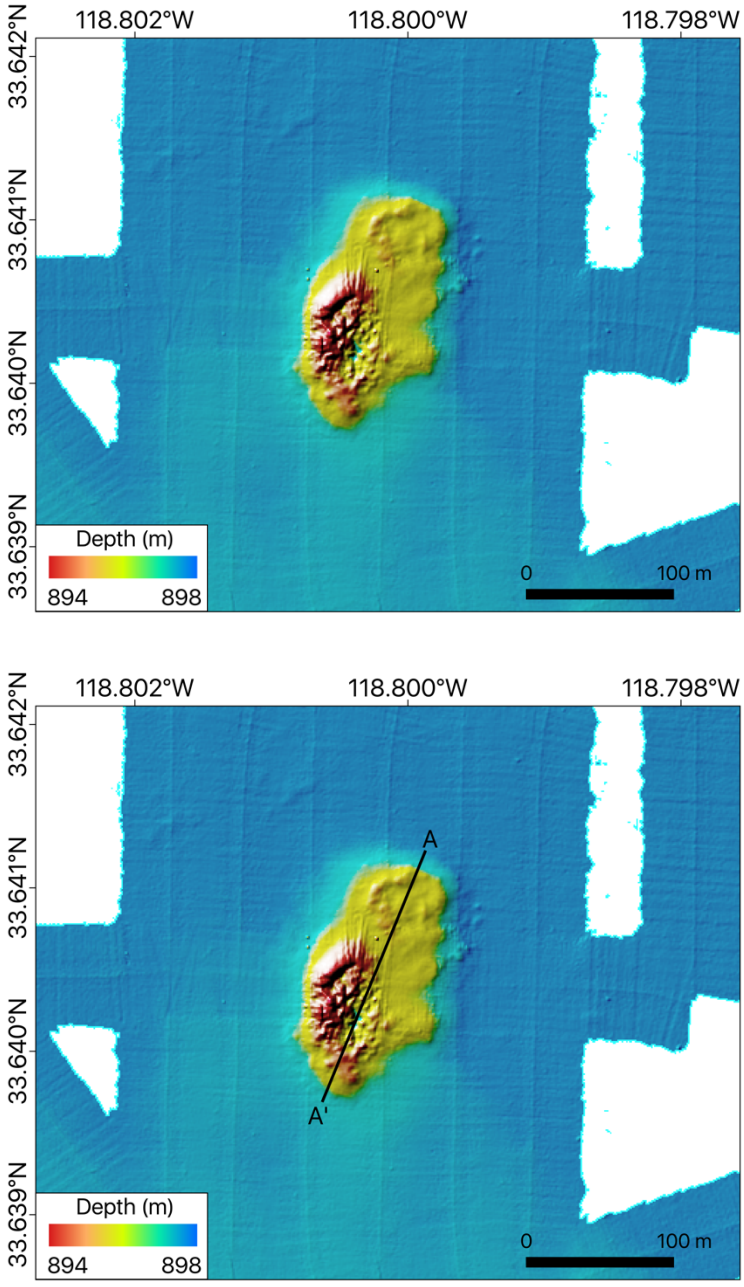

Figure A11-4: Slight zoom of larger mound on the western side of Southwest Mound site

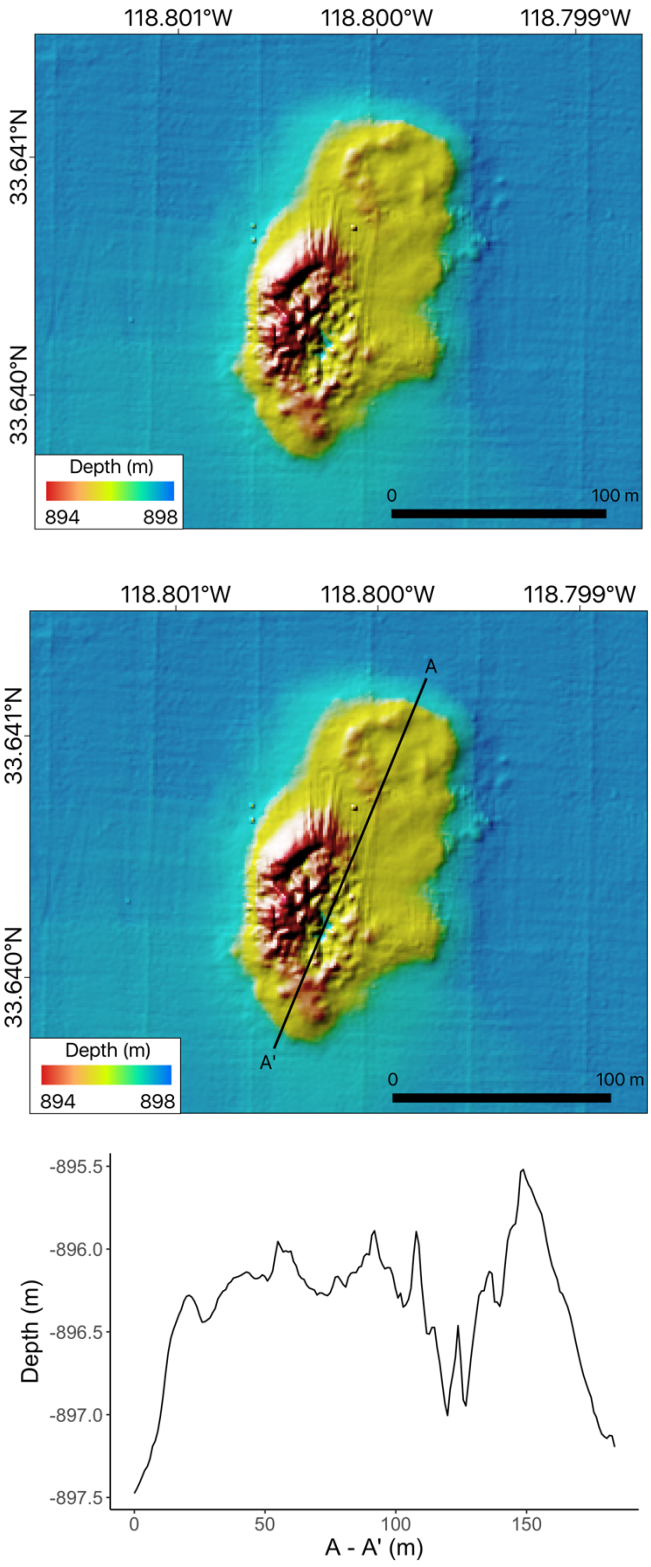

Figure A11-5: Full zoom of western hydrate mound at Southwest Mound site

3D Maps

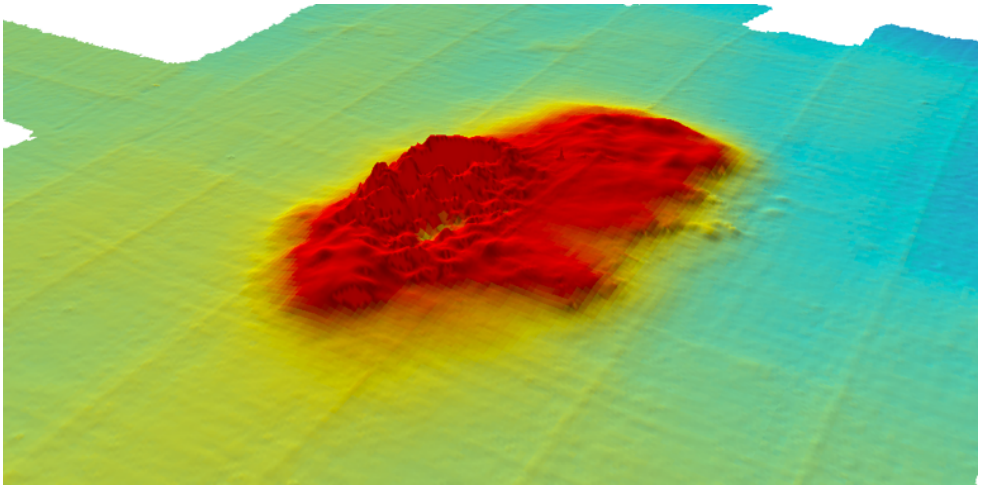

Figure A12-1: View of the larger mound from the south-southeast

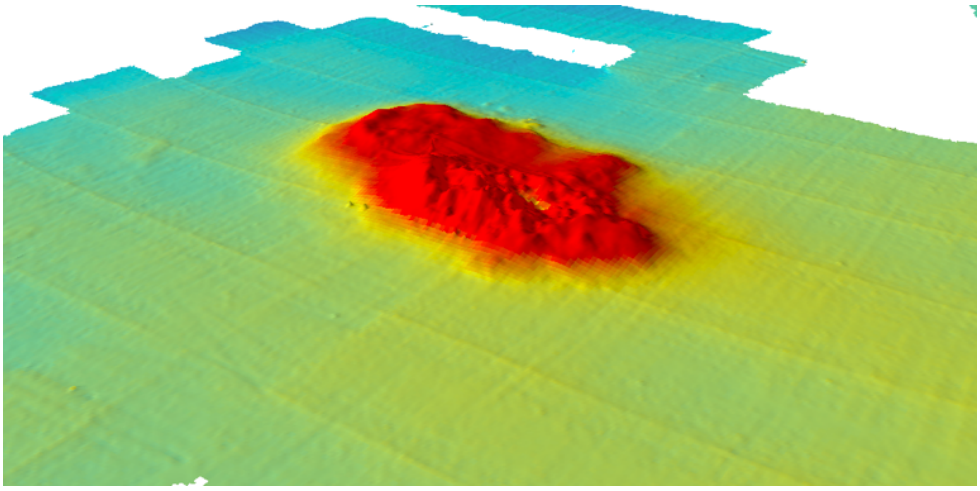

Figure A12-2:View of the larger mound from the southwest

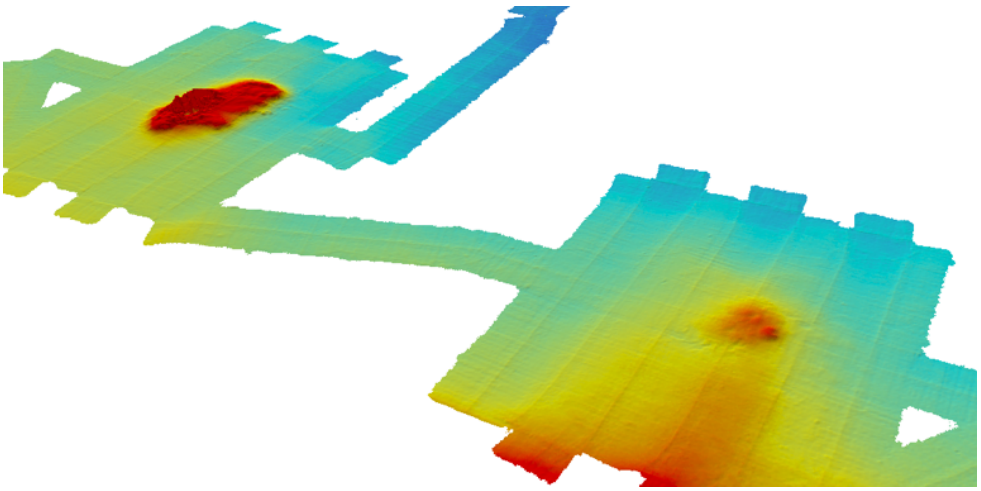

Figure A12-3: View of entire survey area

Gas Spewing Brine Mud Volcano (Sentry 319 and 320)

The gas-spewing, brine mud volcano was surveyed on Sentry 319 and Sentry 320. Sentry 319 was conducted on 06/24/15 between 04:45 and 10:29. Sentry 320 was conducted on 06/25/15 between 00:51 and 07:20.

GSBMV	
Source	Mud
Activity	Active
Count	6
Depth (m)	966 - 1010
Major Axis (m)	300 ± 140
Minor Axis (m)	376 ± 159
Length/Width	1.26 ± 0.1
Relief (m)	58.3 ± 32.1
Basal Area (10^3 m^2)	94.24 ± 80.92
Volume (10^3 m^3)	4629 ± 5872
Average Slope (°)	13.5 ± 1.5
Area/Relief (10^3 m)	1.45 ± 0.53
HI	0.49 ± 0.06

2D Maps

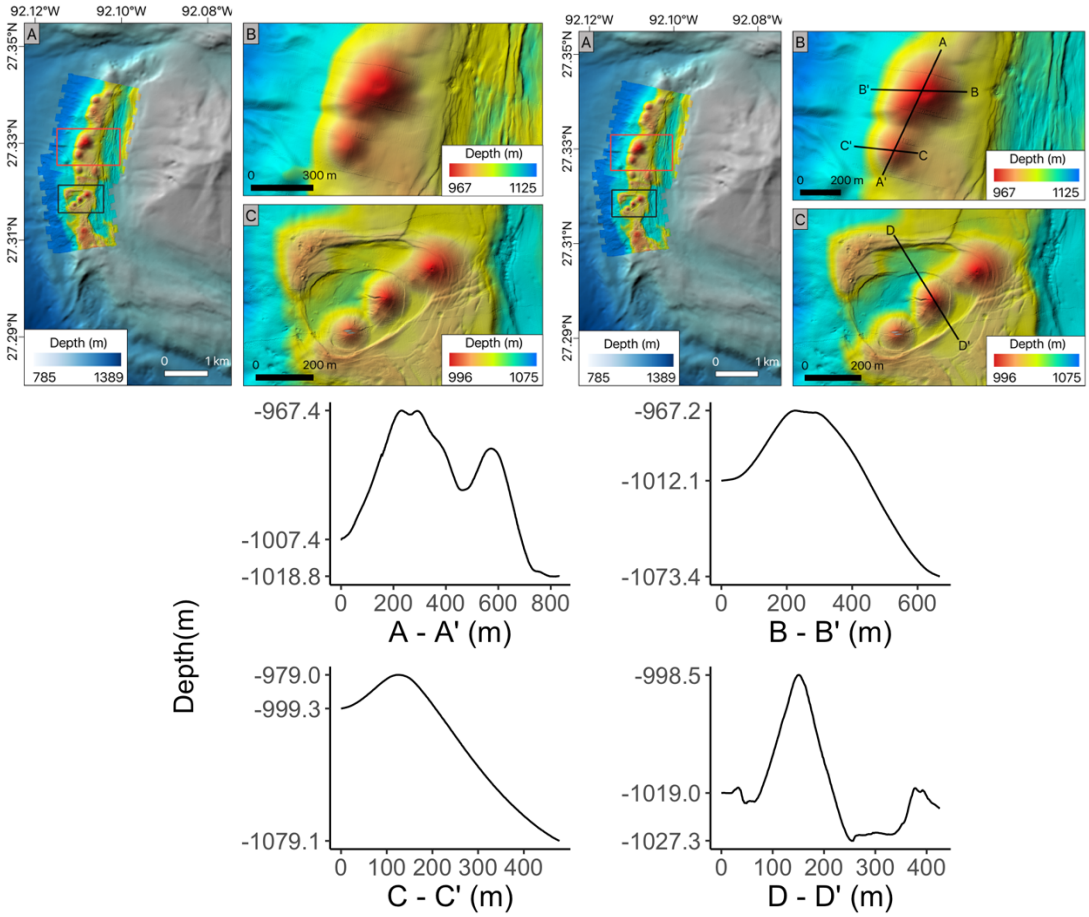

Figure A13-1: A overview of the GSBMV site

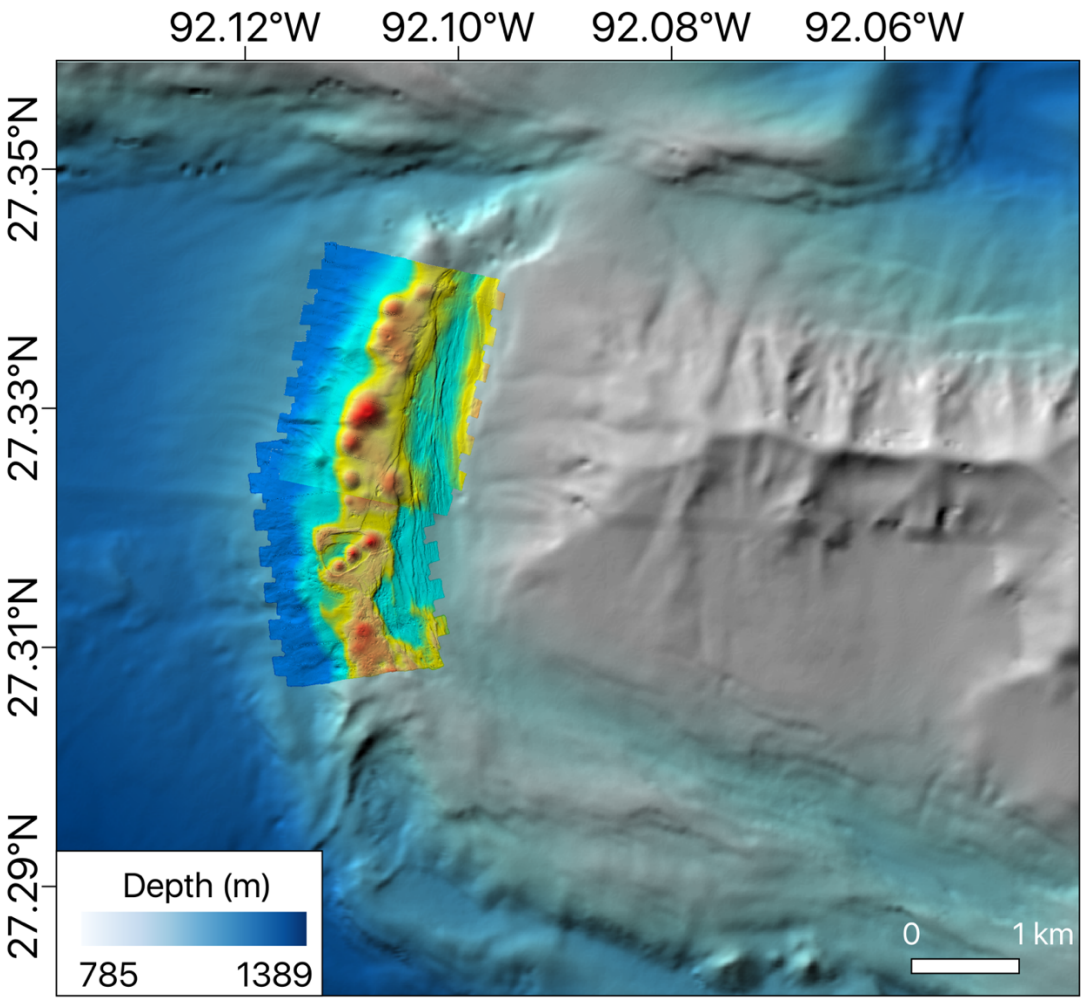

Figure A13-2: An overview of the GSBMV site without the zooms

Northern Block Maps (Sentry320)

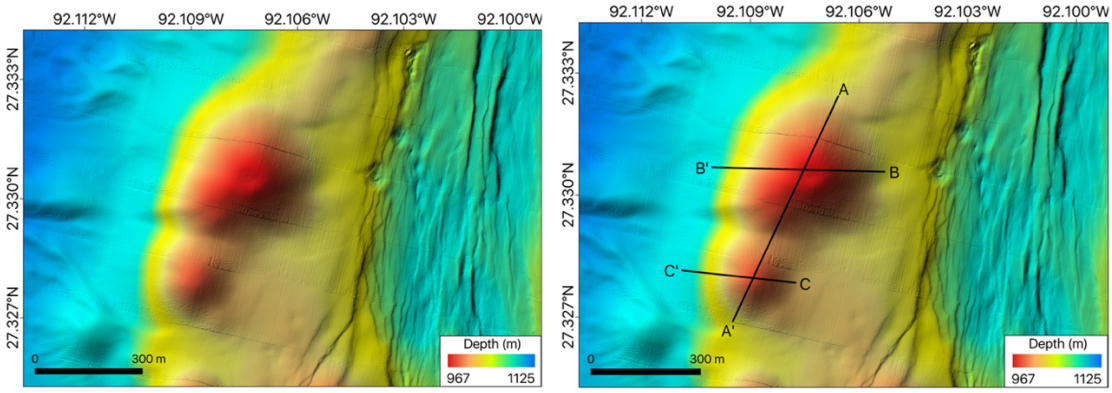

Figure A13-3: Mud volcanoes at GSBMV site from Sentry 320

Sentry 320	
Source	Mud
Activity	Active
Count	3
Depth (m)	967 - 1010
Major Axis (m)	513 ± 112
Minor Axis (m)	404 ± 122
Length/Width	1.30 ± 0.13
Relief (m)	86.9 ± 17.4
Basal Area (10^3 m^2)	153.7 ± 77.1
Volume (10^3 m^3)	8807 ± 5834
Average Slope (°)	14.26 ± 0.93
Area/Relief (10^3 m)	1.68 ± 0.59
HI	0.56 ± 0.01

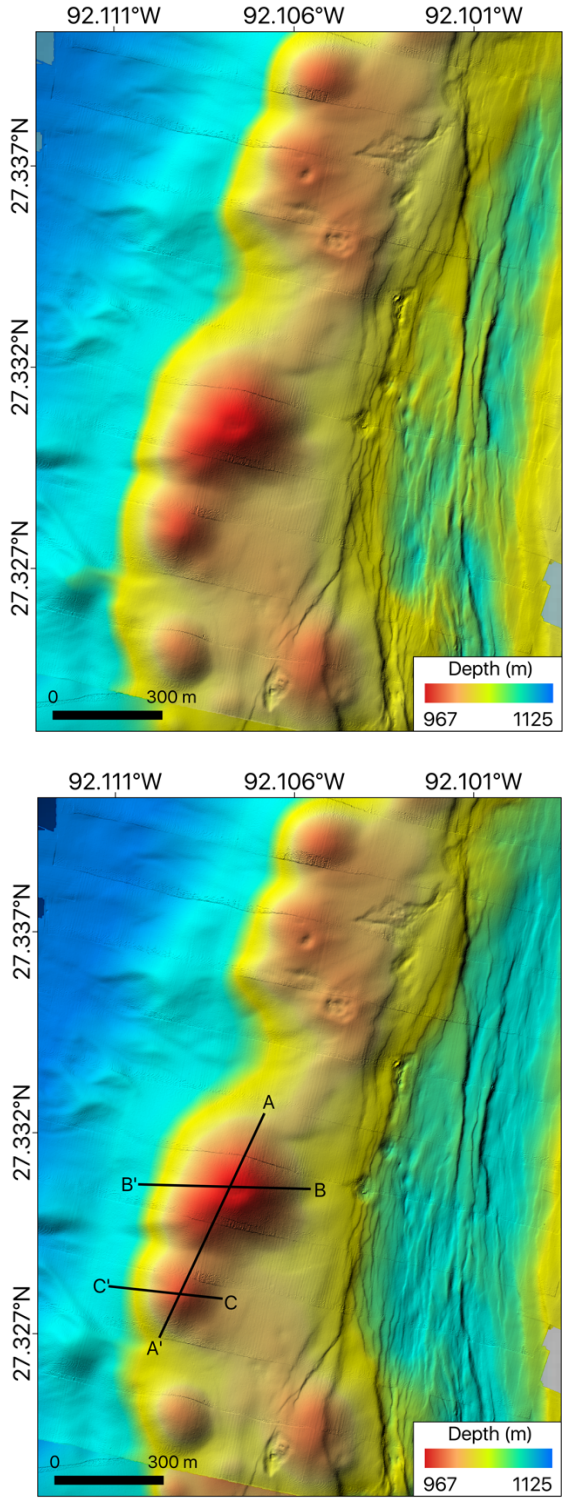

Figure A13-4: Mud volcanoes at the GSBMV site from Sentry 320

Southern Block (Sentry319)

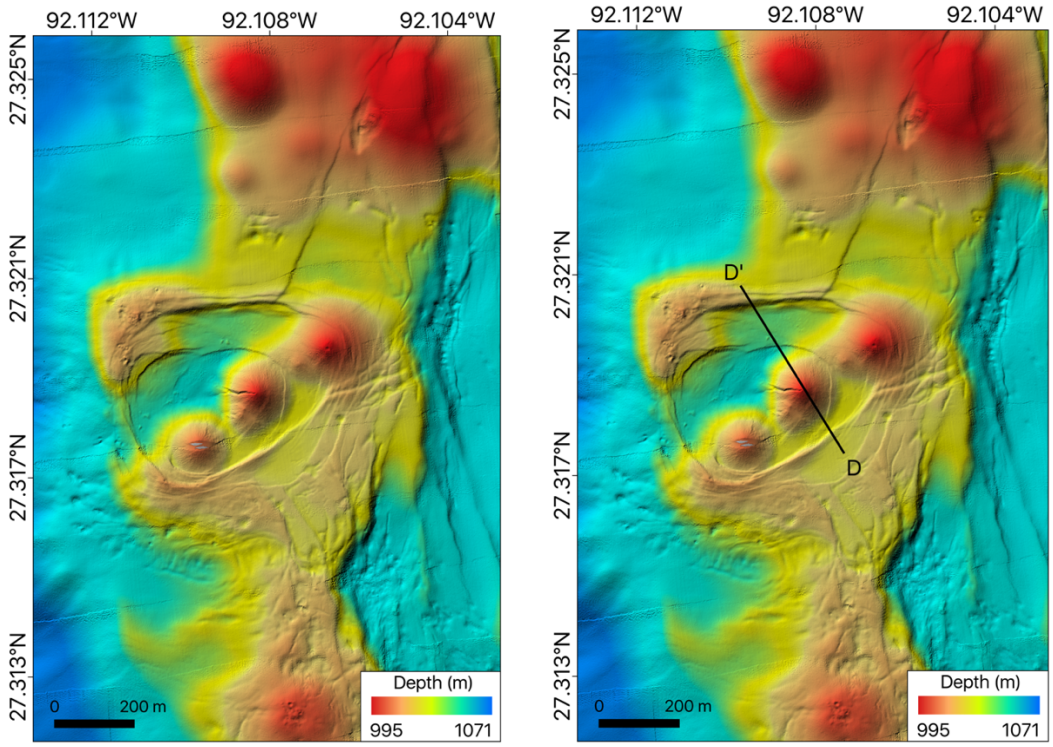

Figure A13-5: Three mud volcanoes within a brine pool at the GSBMV site.

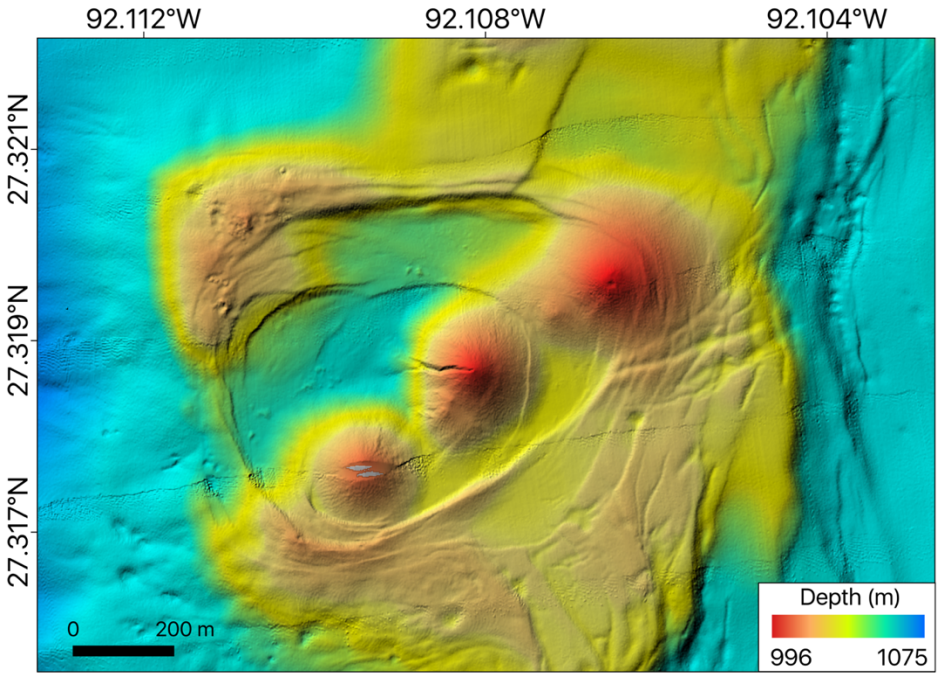

Figure A13-6: Different view of mud volcanoes from Sentry 319

Sentry 319	
Source	Mud
Activity	Active
Count	3
Depth (m)	996 - 1010
Major Axis (m)	239 ± 22
Minor Axis (m)	194 ± 27
Length/Width	1.24 ± 0.08
Relief (m)	28.8 ± 3.6
Basal Area (10^3 m^2)	34.8 ± 8.7
Volume (10^3 m^3)	450 ± 96
Average Slope (°)	12.3 ± 1.5
Area/Relief (10^3 m)	1.22 ± 0.32
HI	0.44 ± 0.03

3D Maps

Sentry 320

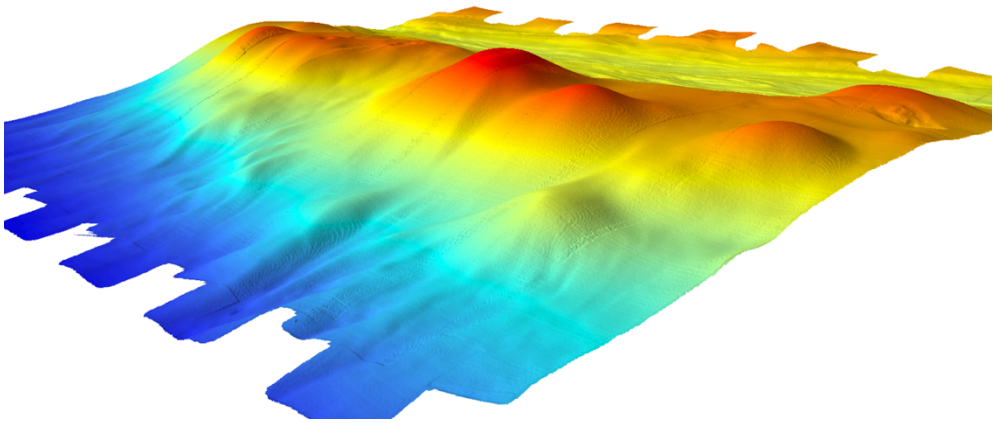

Figure A14-1: Perspective view from the south-southwest

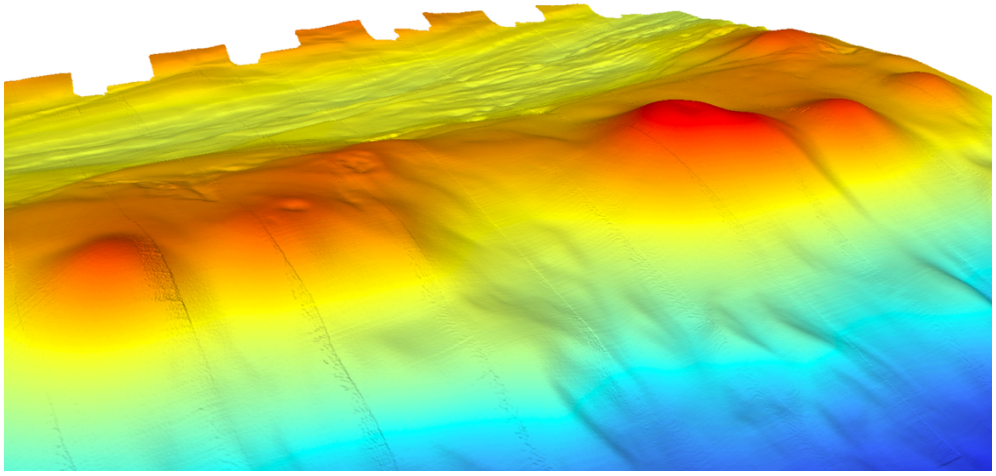

Figure A14-2: Perspective view from the west

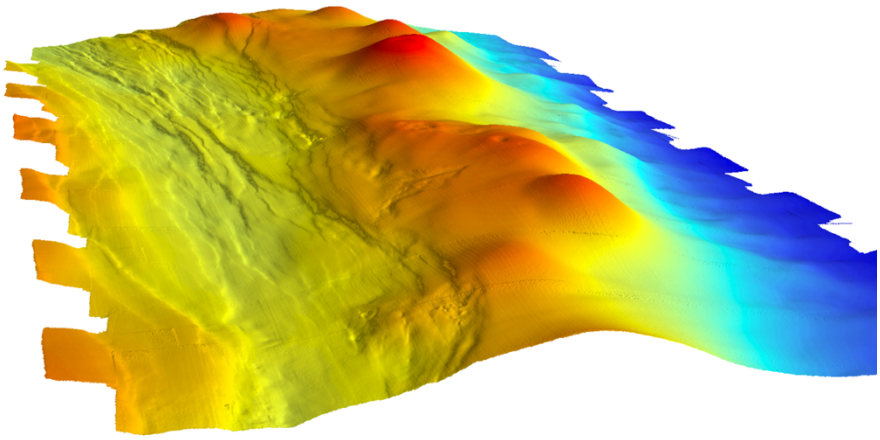

Figure A14-3: Perspective view from the north

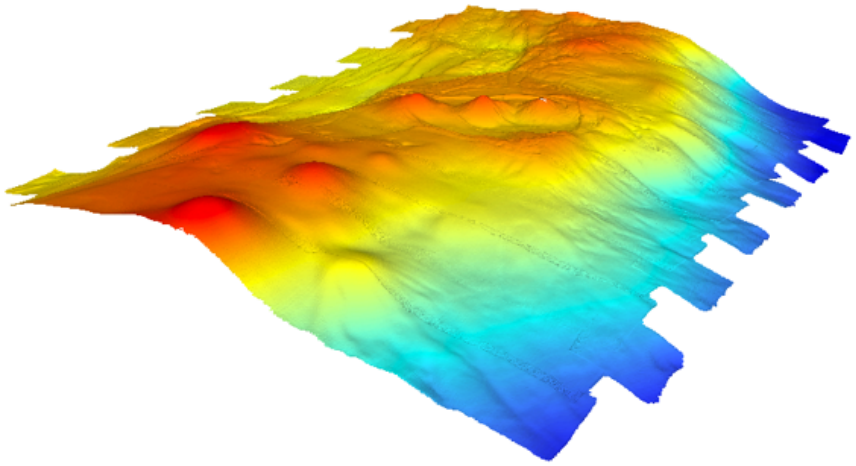

Figure A14-4: Perspective view from the north

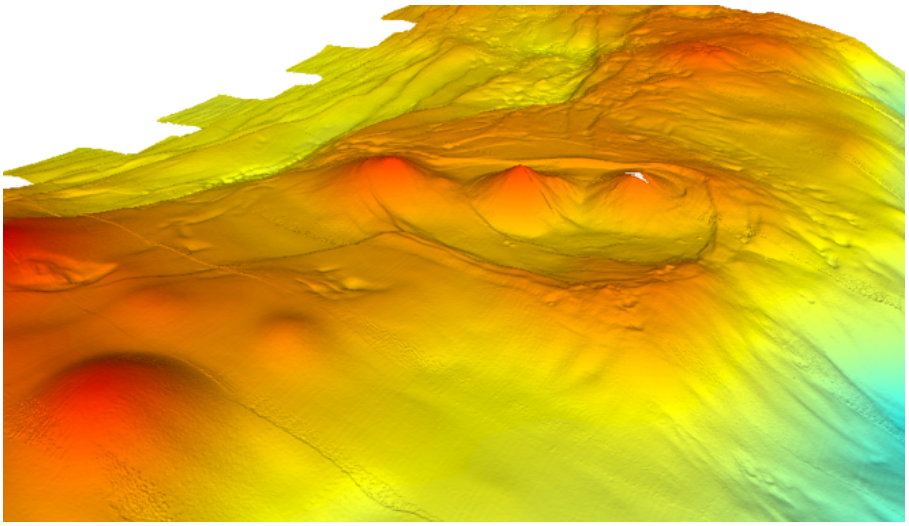

Figure A14-5: Close-up of mud volcanos in a brine pool from north

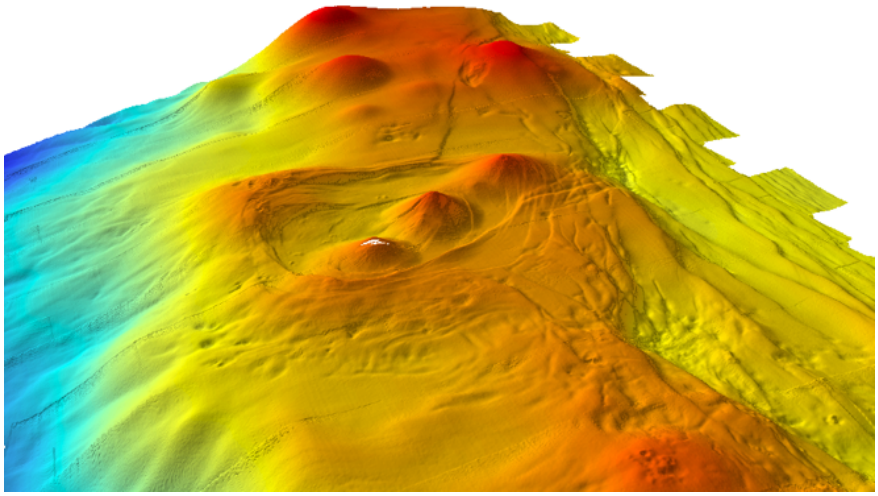

Figure A14-6: Perspective view from south

Pockmarks

Bullnose (Sentry 030)

Site	Bullnose (n = 214)
Source	Methane
Activity	Active
Depth (m)	225
Length/Width	1.32 ± 0.19
Relief (m)	1.38 ± 1.68
Basal Area (10^3m^2)	0.719 ± 4.503
Volume (10^3m^3)	1.28 ± 9.73
Slope (°)	6.3 ± 1.2
Area/Relief	0.59 ± 3.75
HI	0.51 ± 0.06

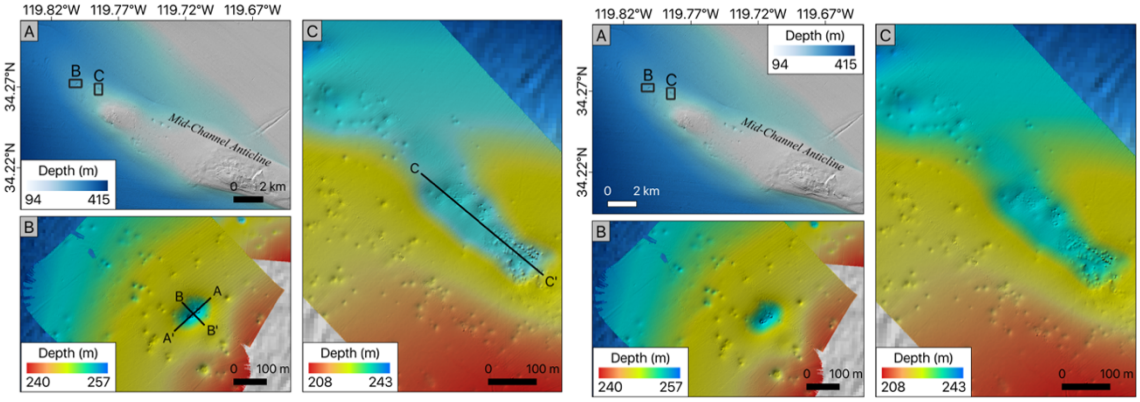

Figure A15-1: Overview of Bullnose pockmarks. Block 1 is shown in panel B and Block 2 is shown in panel C. Cross sections are shown in block specific sections below.

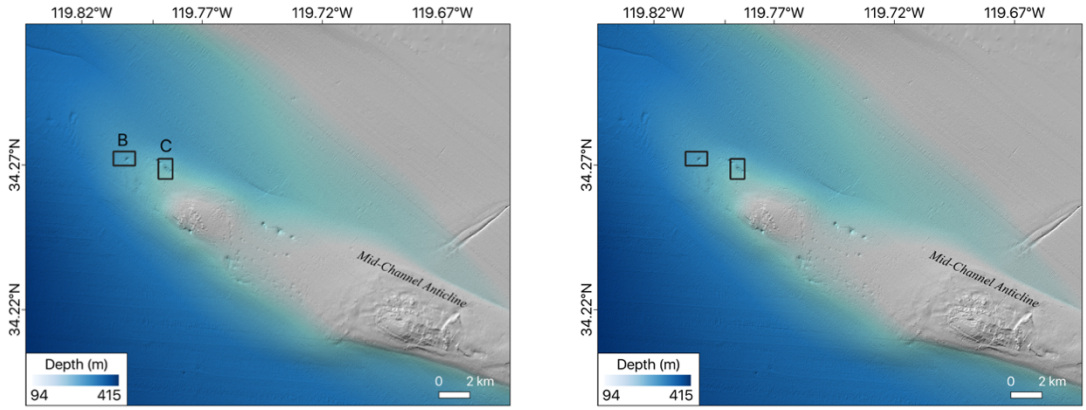

Figure A15-2: Coarse bathymetry of pockmarks at Bullnose

Bullnose (Block 1)

Bullnose was surveyed on Sentry 030. Block 1 was conducted on 09/18/09 between 04:16 and 05:01.

2D Maps

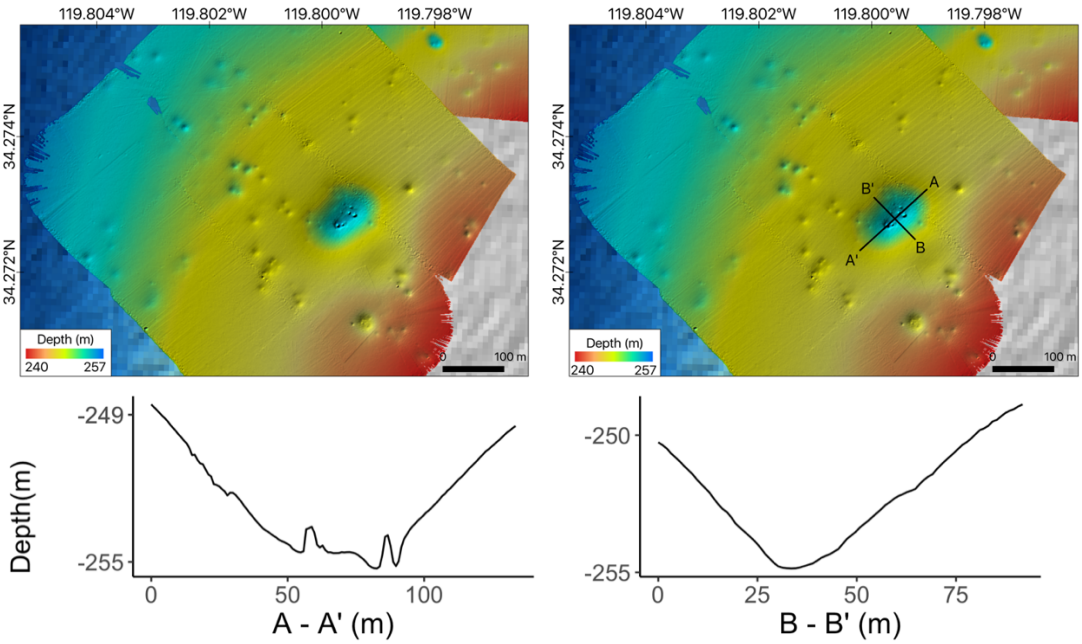

Figure A15-3: An overview of the northeastern block of the Bullnose site

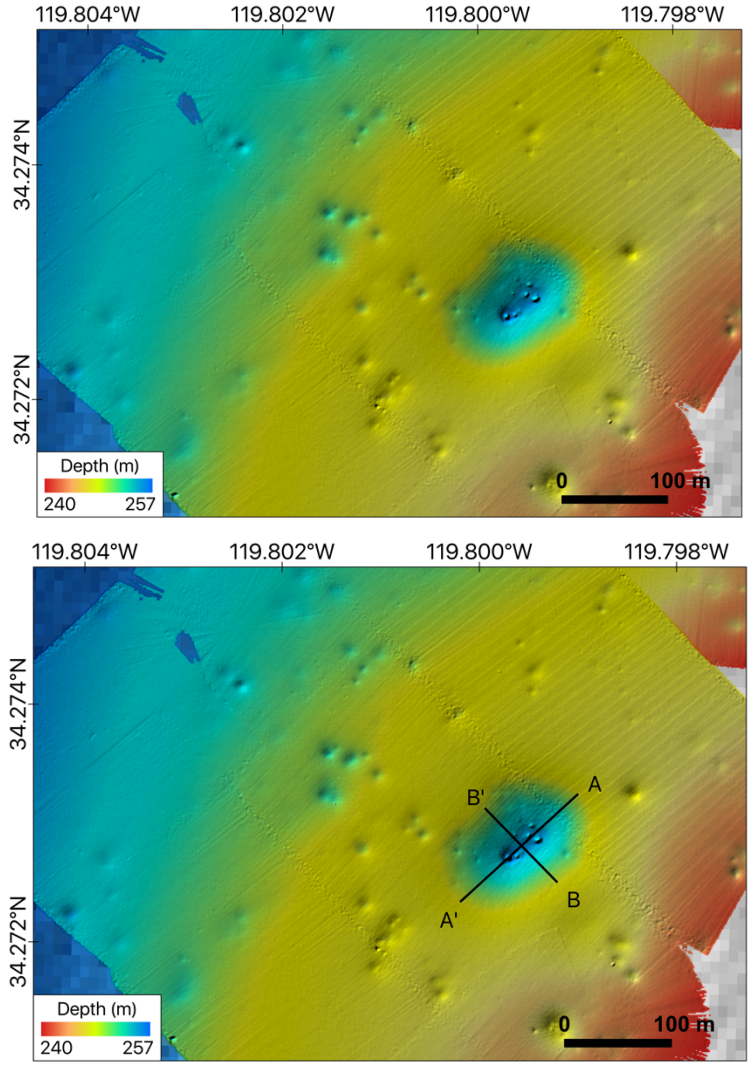

Figure A15-4: Slight zoom of block 1 of the Bullnose area

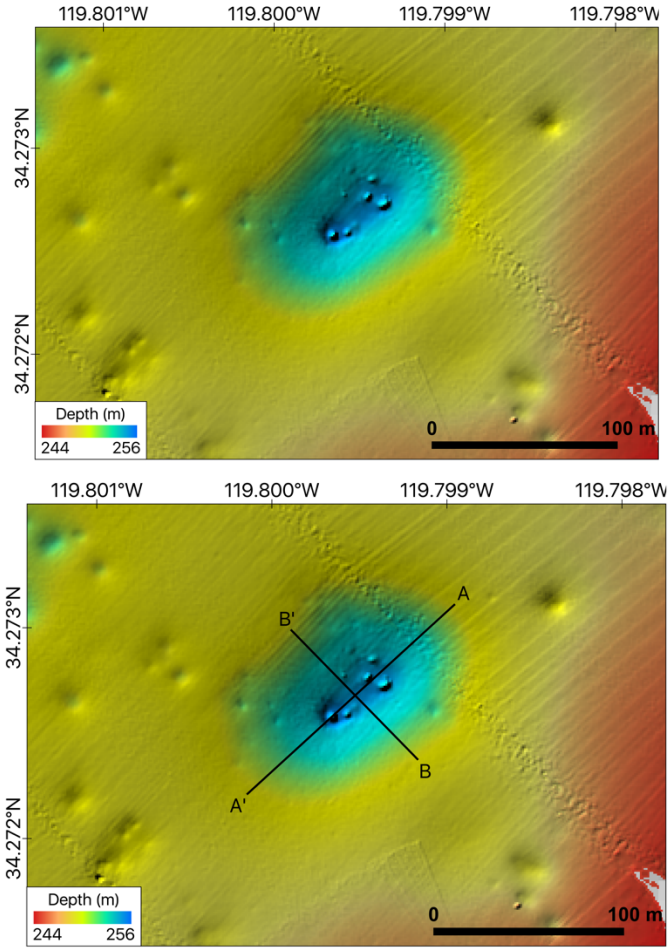

Figure A15-5: A closer look at the largest pockmark in this area

3D Maps

These maps were generated at 5x exaggeration.

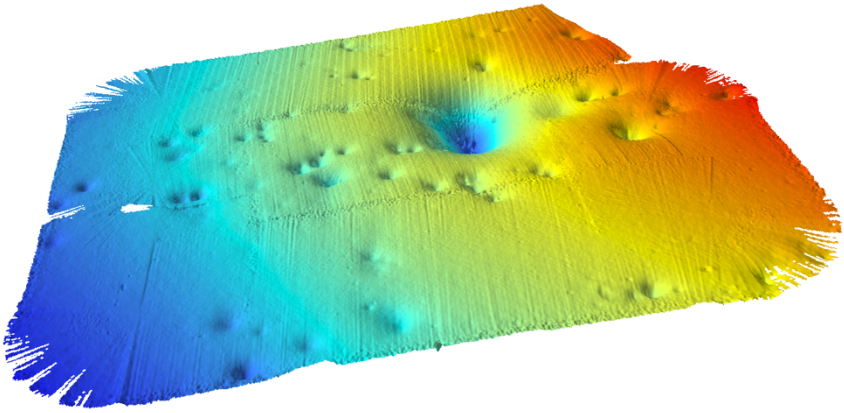

Figure A16-1: Perspective view from the southwest. The largest pockmark is about 120 meters in diameter.

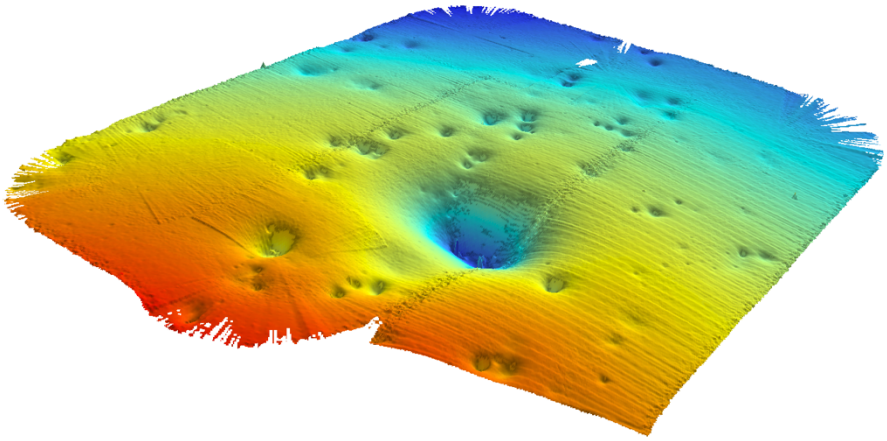

Figure A16-2: Perspective view from the east

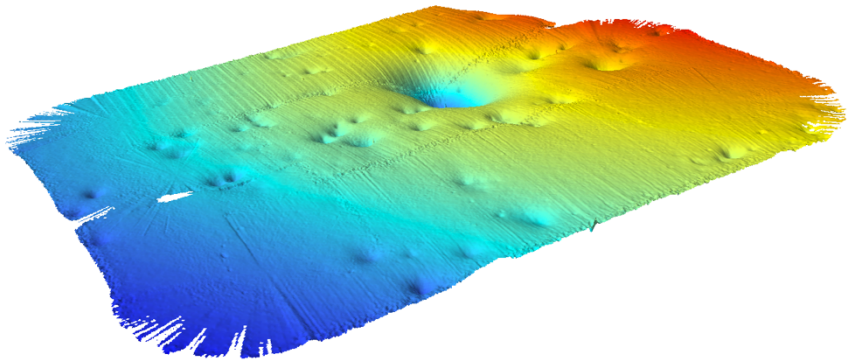

Figure A16-3: Perspective view from the west, at a lower elevation

Bullnose (Block 2)

Block 2 of Sentry 030 was conducted on 09/18/09 between 06:16 and 07:55.

2D Maps

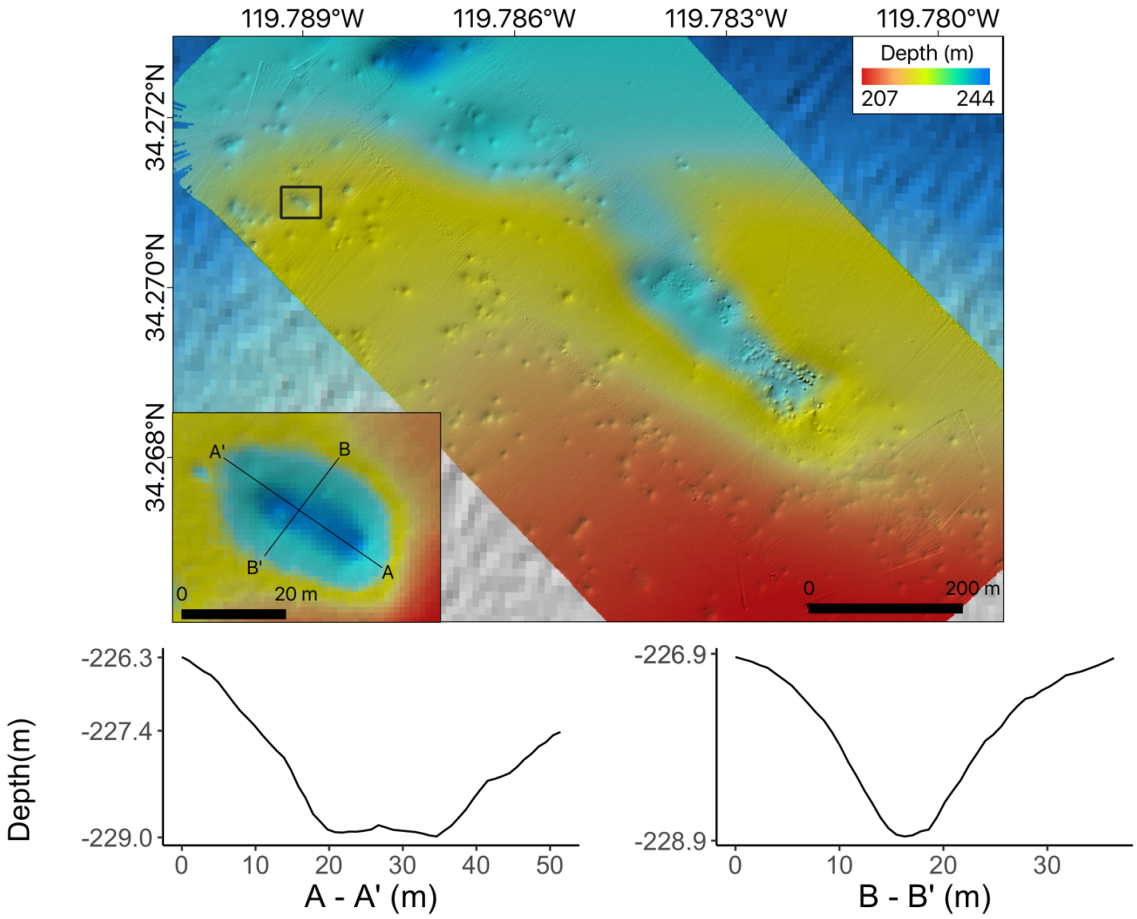

Figure A17-1: An overview of block 2 of the Bullnose survey area

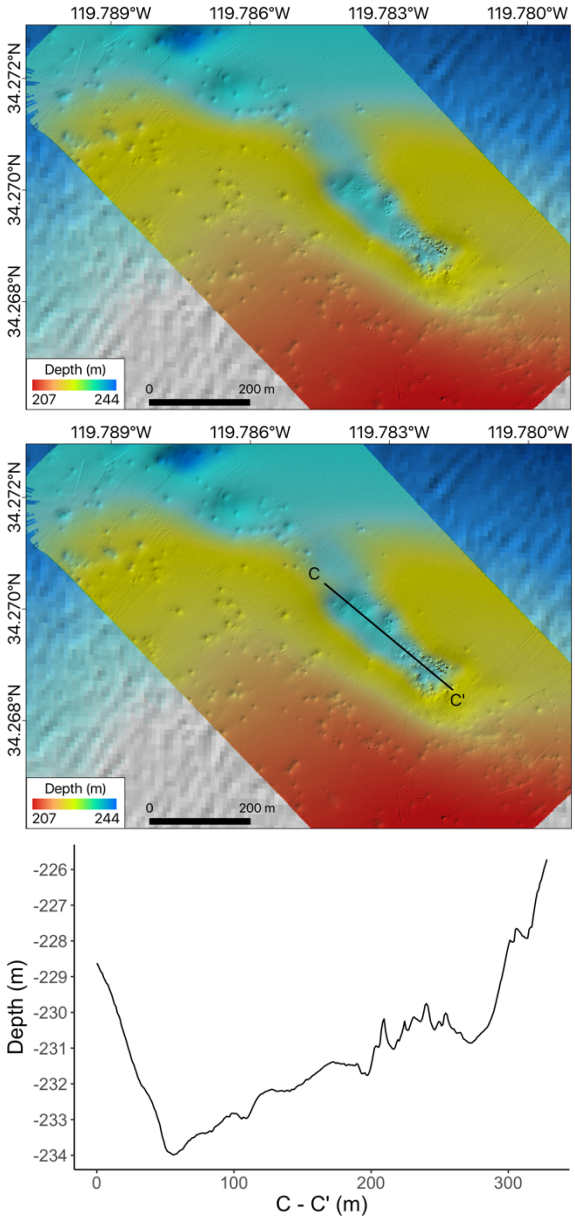

Figure A17-2: A slight zoom of block 2 of the Bullnose survey area

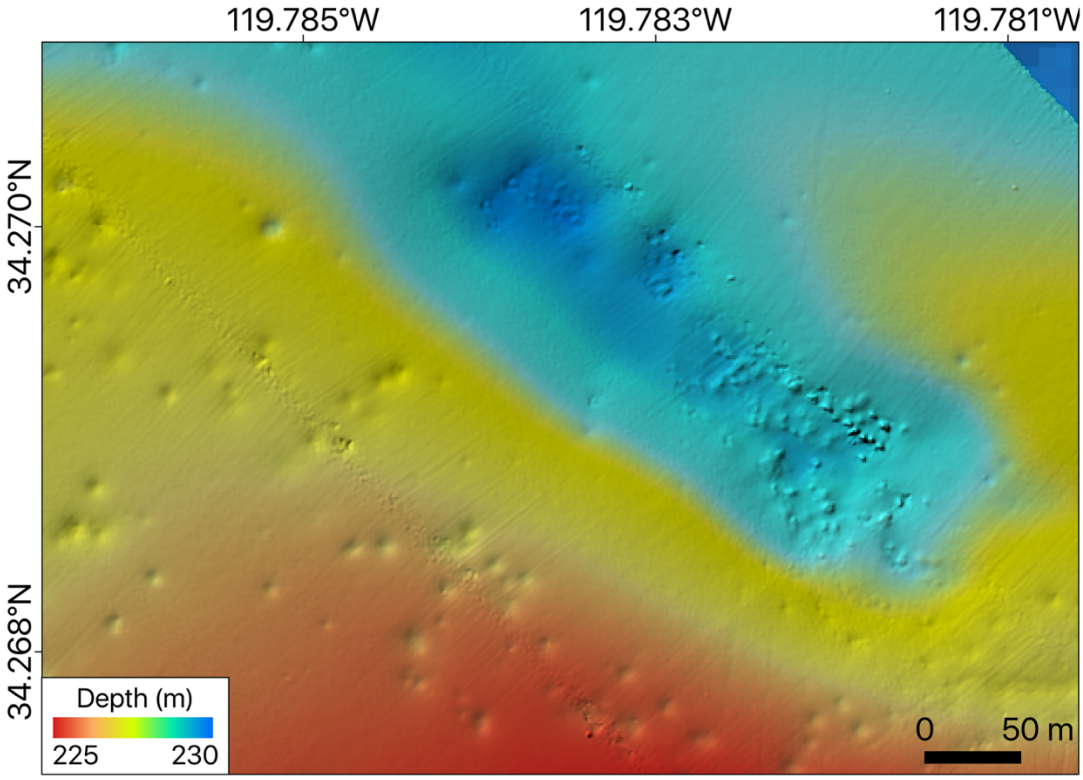

Figure A17-3: A closer view of the elongated pockmark at Bullnose

3D Maps

These maps are displayed at 3x vertical exaggeration.

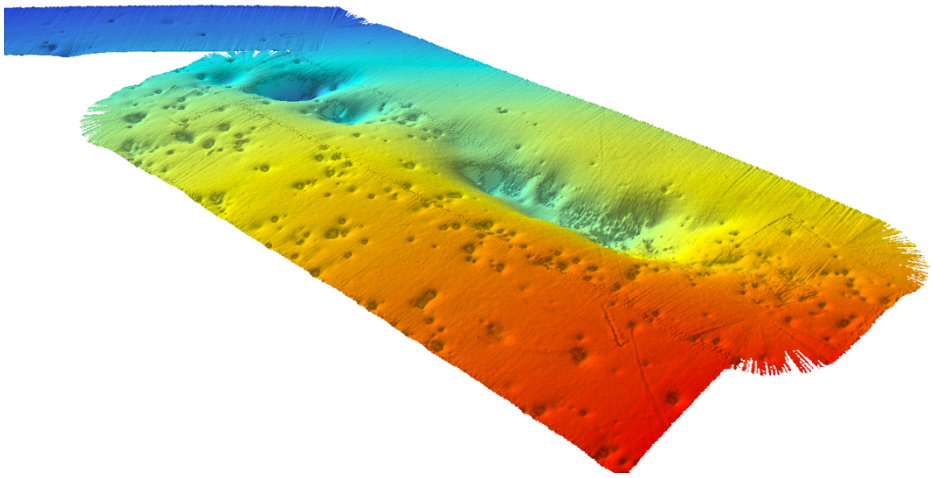

Figure A18-1: Perspective view of block 2 from the south

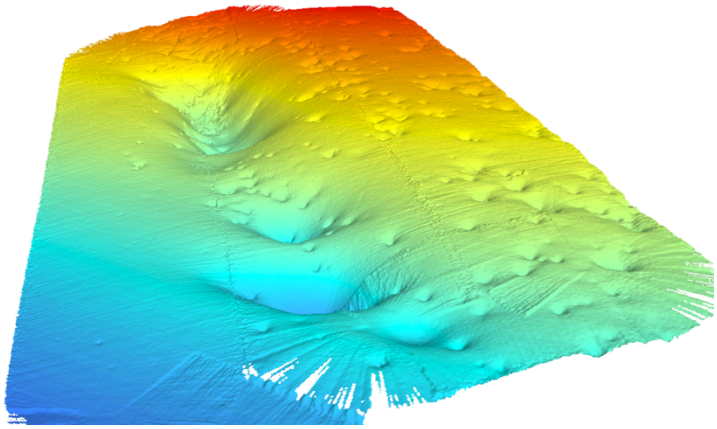

Figure A18-2: Perspective view of block 2 from the northwest

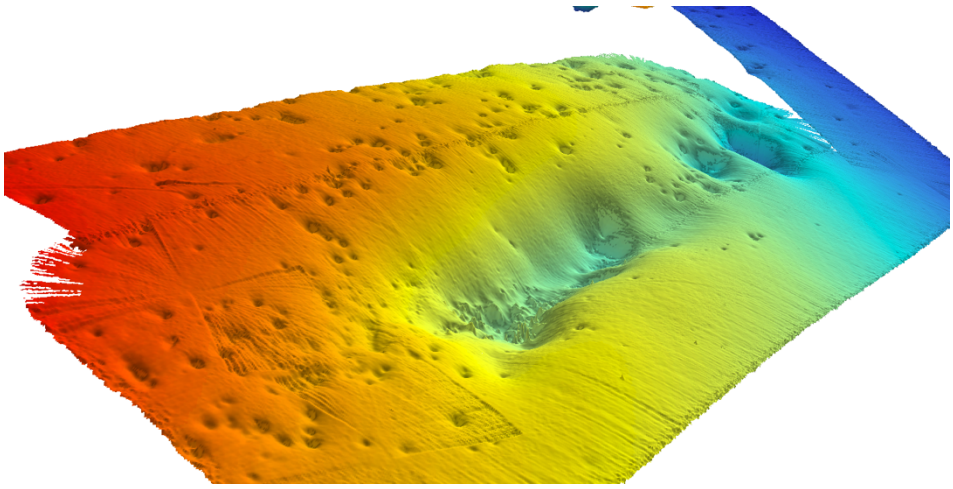

Figure A18-3: Perspective view of block 2 from the southeast

Santa Monica Basin Pits (Sentry 035)

The Santa Monica Basin Puts were surveyed during Sentry 035, conducted on 09/25/09 between 02:22 and 05:54.

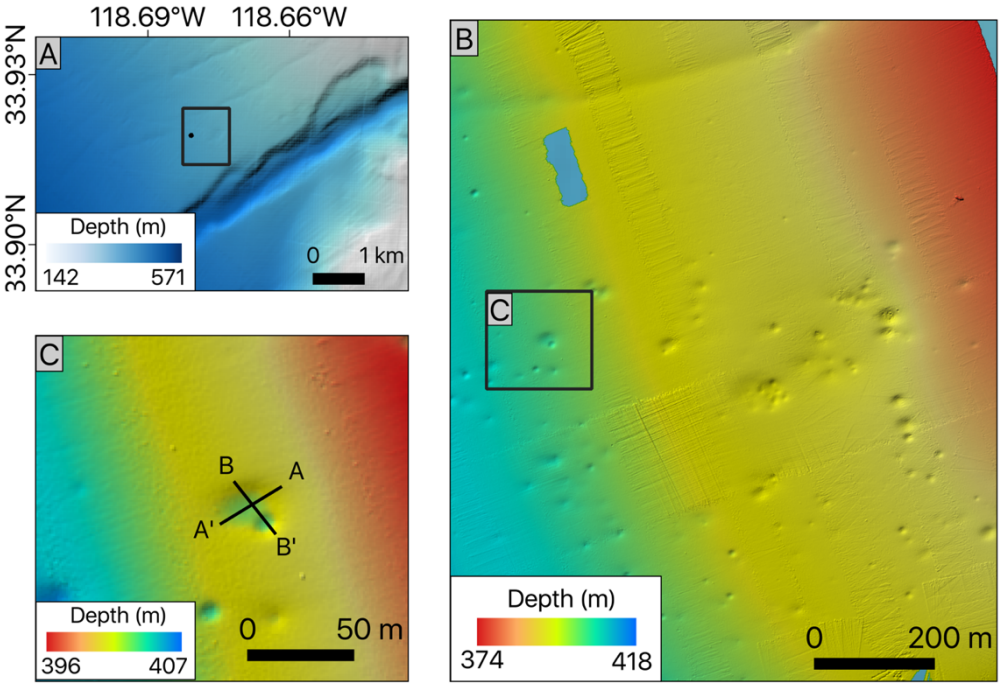

Figure A19-1: An overview of the Santa Monica Basin Pits

Site	Santa Monica Basin Pits (n = 109)
Source*	Methane
Activity	Dormant
Depth (m)	397
Length/Width	1.39 ± 0.26
Relief (m)	1.6 ± 0.7
Basal Area (10^3m^2)	0.504 ± 0.421
Volume (10^3m^3)	0.479 ± 0.746
Slope (°)	4.9 ± 1.6
Area/Relief	0.32 ± 0.6
HI	0.50 ± 0.05

*Source is inferred at this site

2D Maps

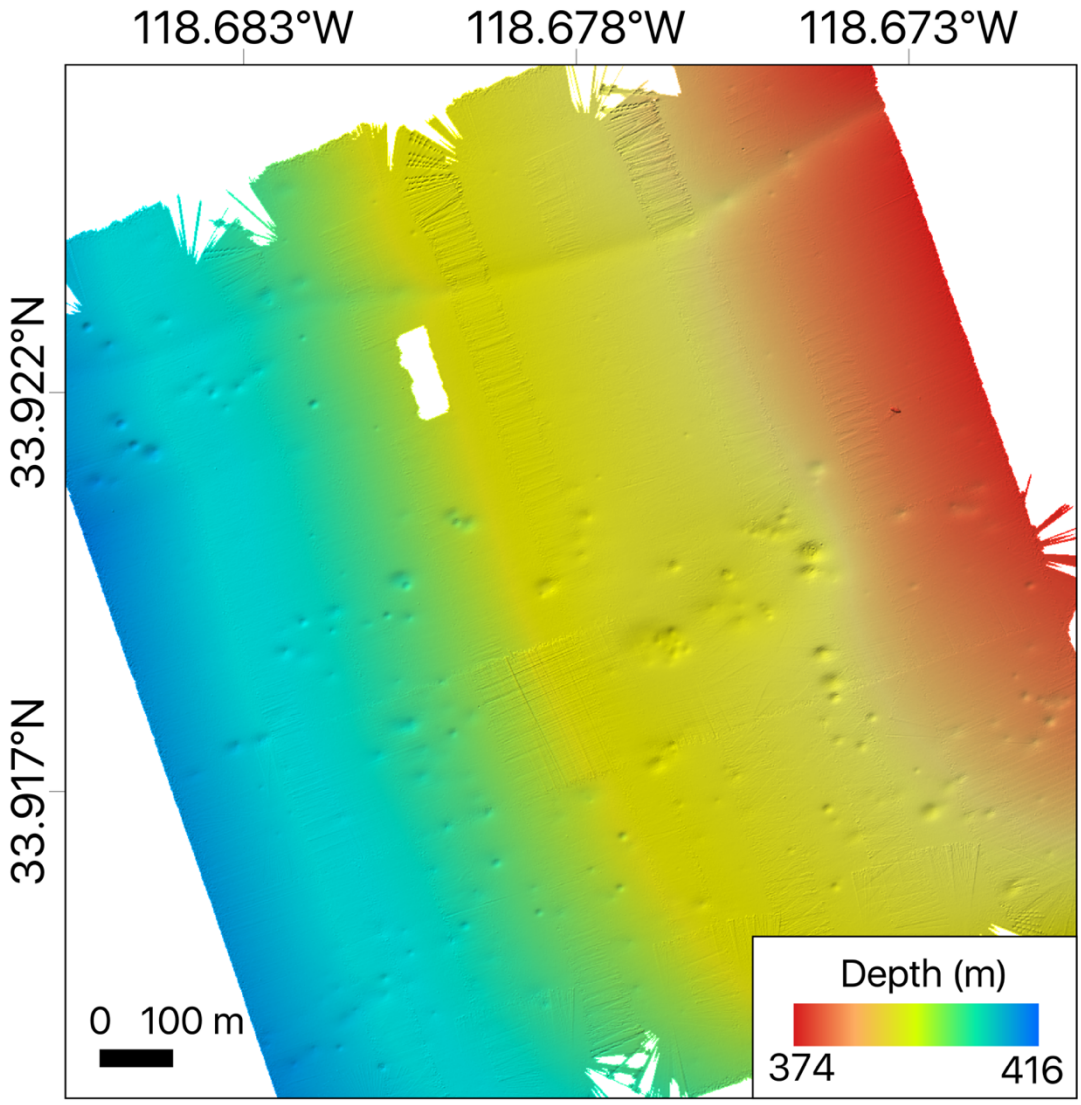

Figure A19-2: An overview of dormant pockmarks in the Santa Monica basin

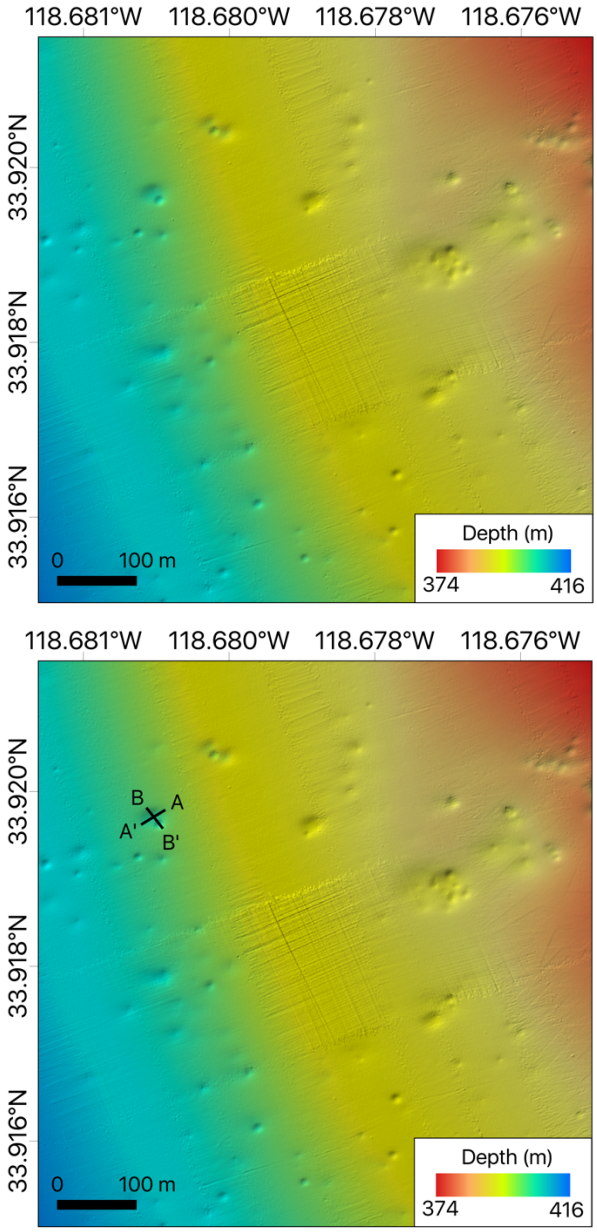

Figure A19-3: Slight zoom of dormant pockmarks in the Santa Monica Basin

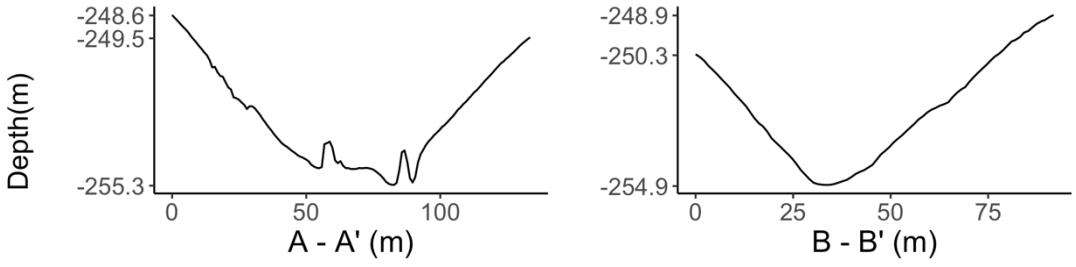

Figure A19-3a: Bathymetric profiles A-A' and B-B'

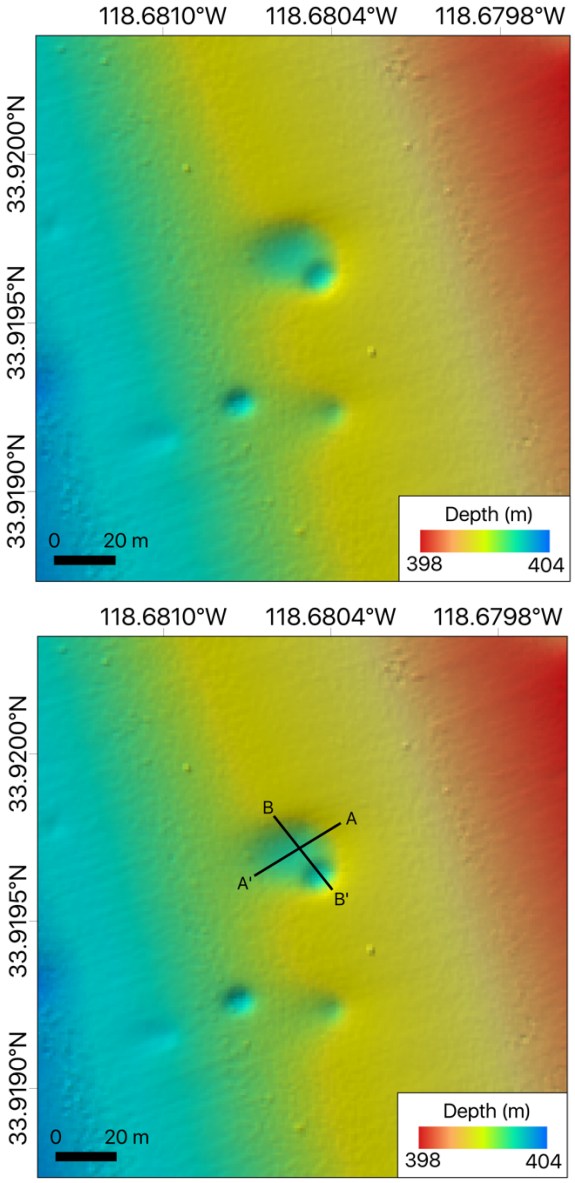

Figure A19-4: Close-up of pockmarks in the Santa Monica Basin

3D Maps

These maps are displayed at 4x vertical exaggeration.

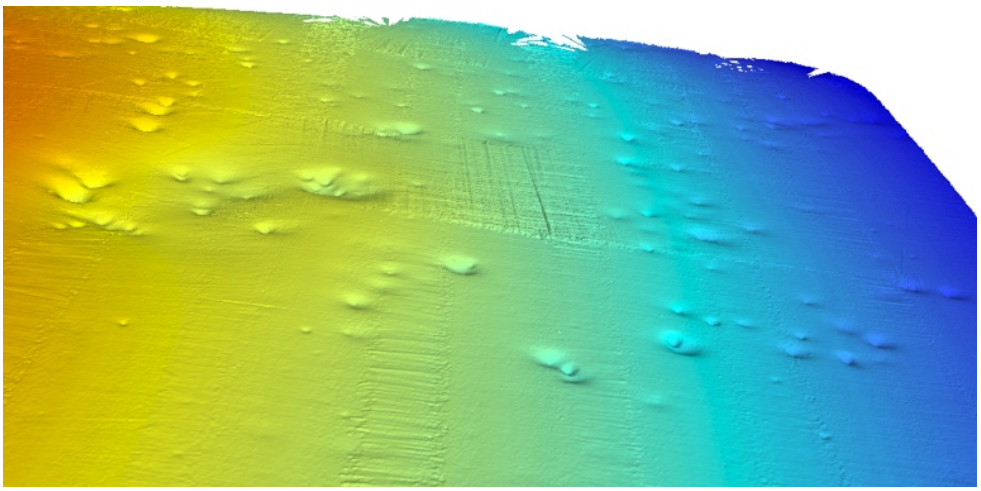

Figure A20-1: Perspective view from north-northwest

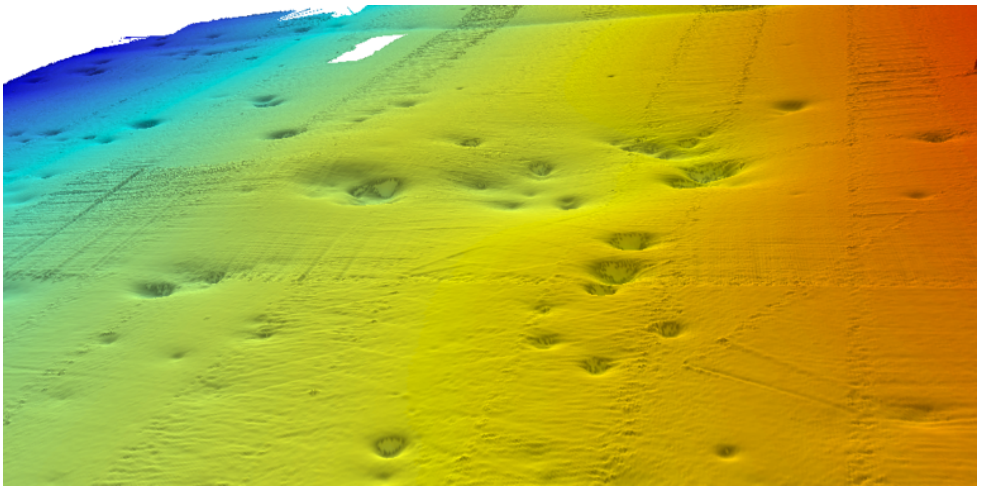

Figure A20-2: Perspective view from south-southeast

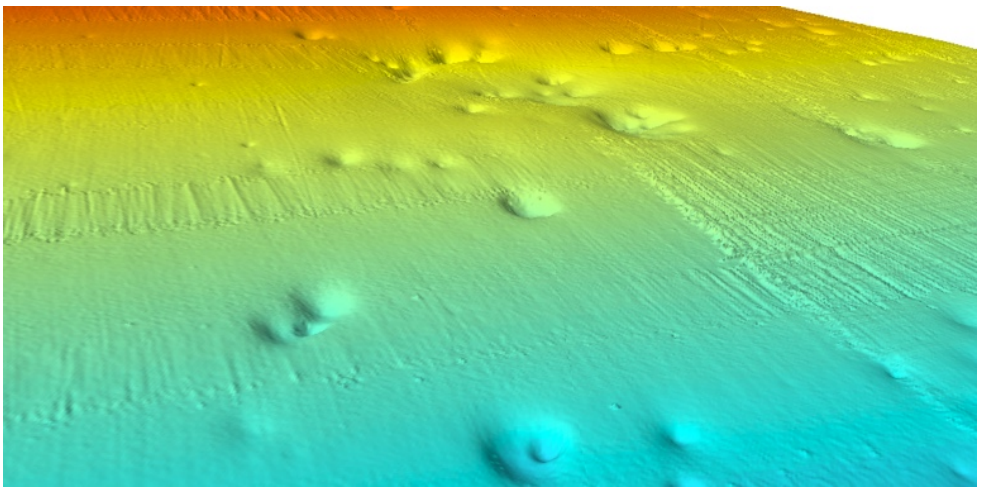

Figure A20-3: Perspective view from the northwest at a lower elevation

Other Sites

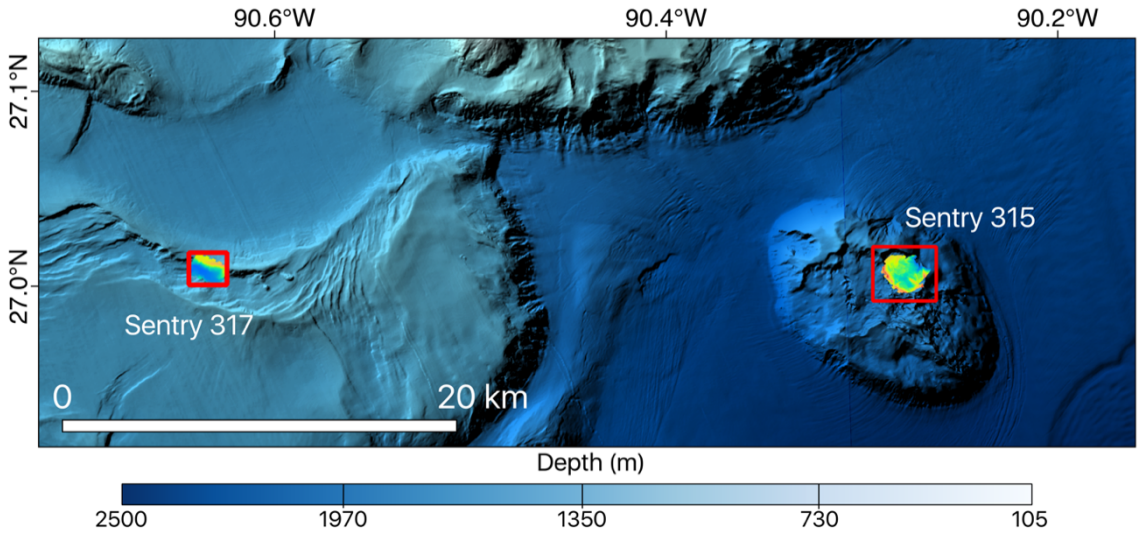

Figure A21-1:Coarse bathymetry for Sentry dives 315 and 317. Finer scale is shown below.

Sentry 315

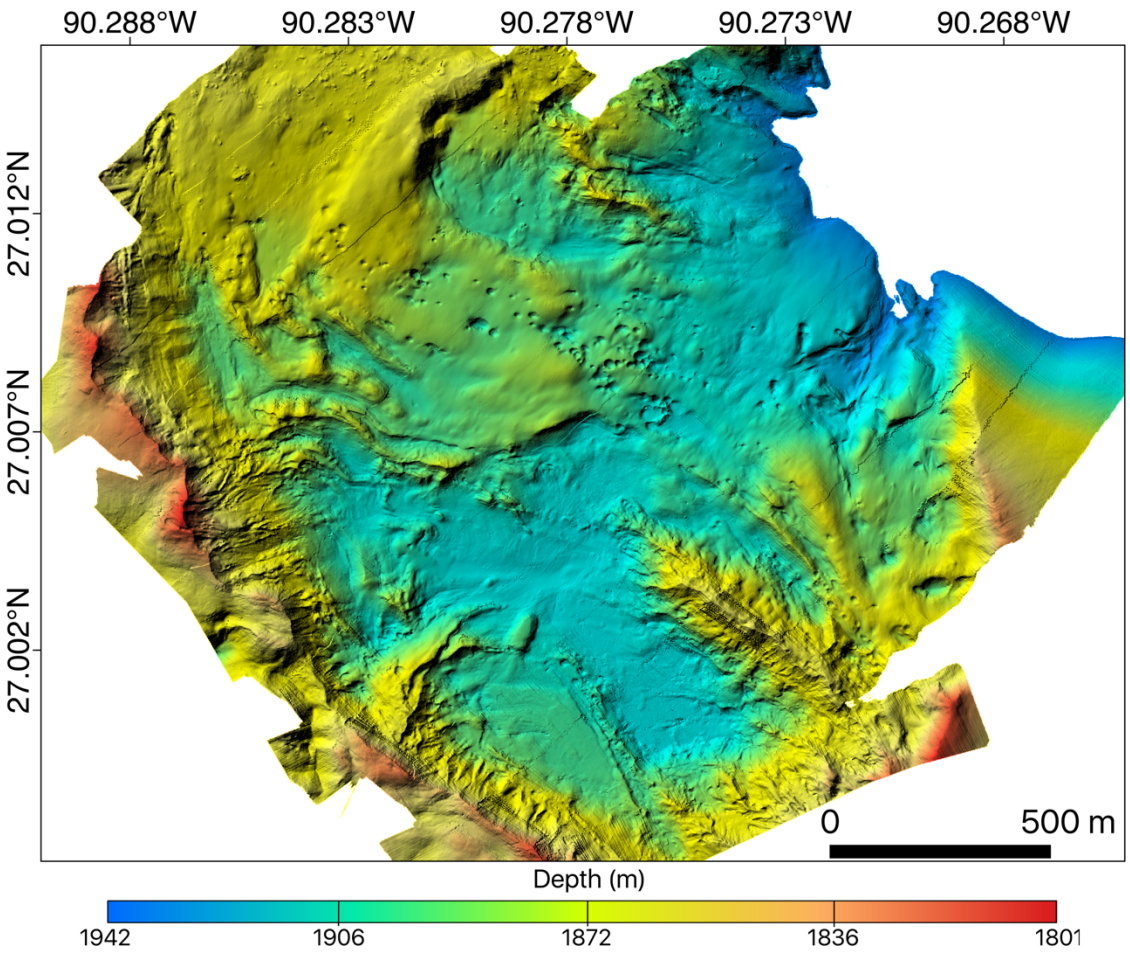

Figure A21-1: An overview of Sentry 315

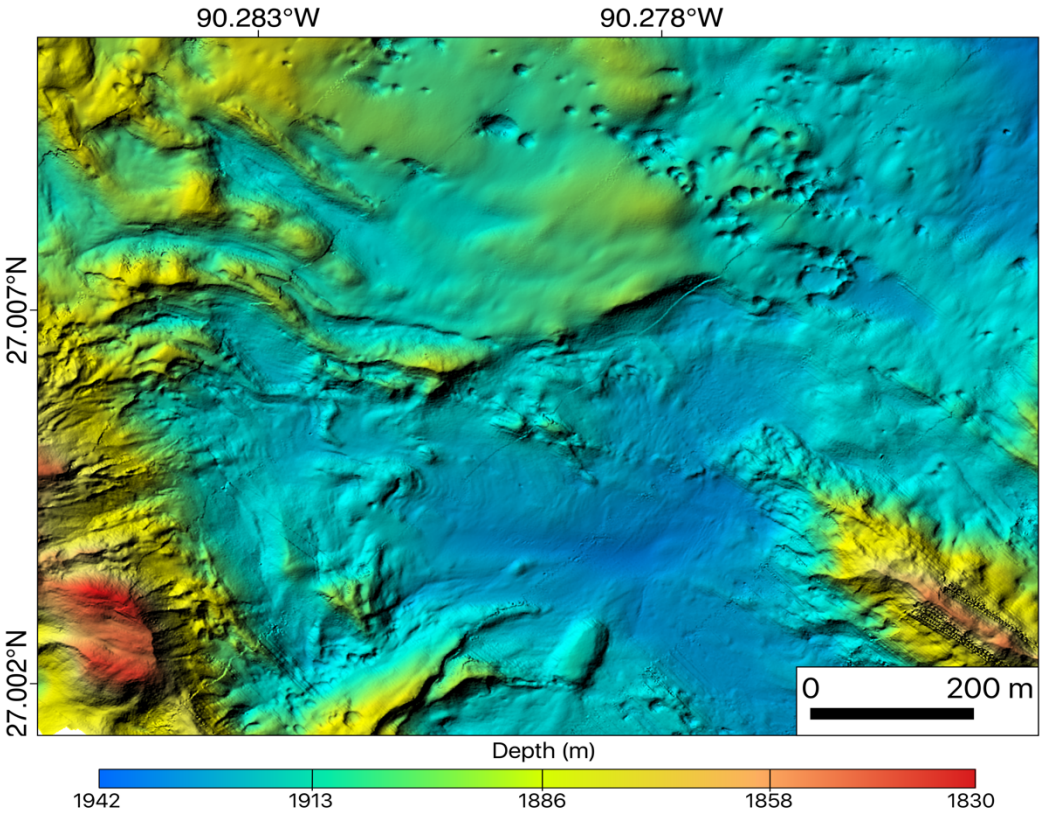

Figure A21-2: Zoomed perspective of Sentry 315. Scour marks are observed in the northern section.

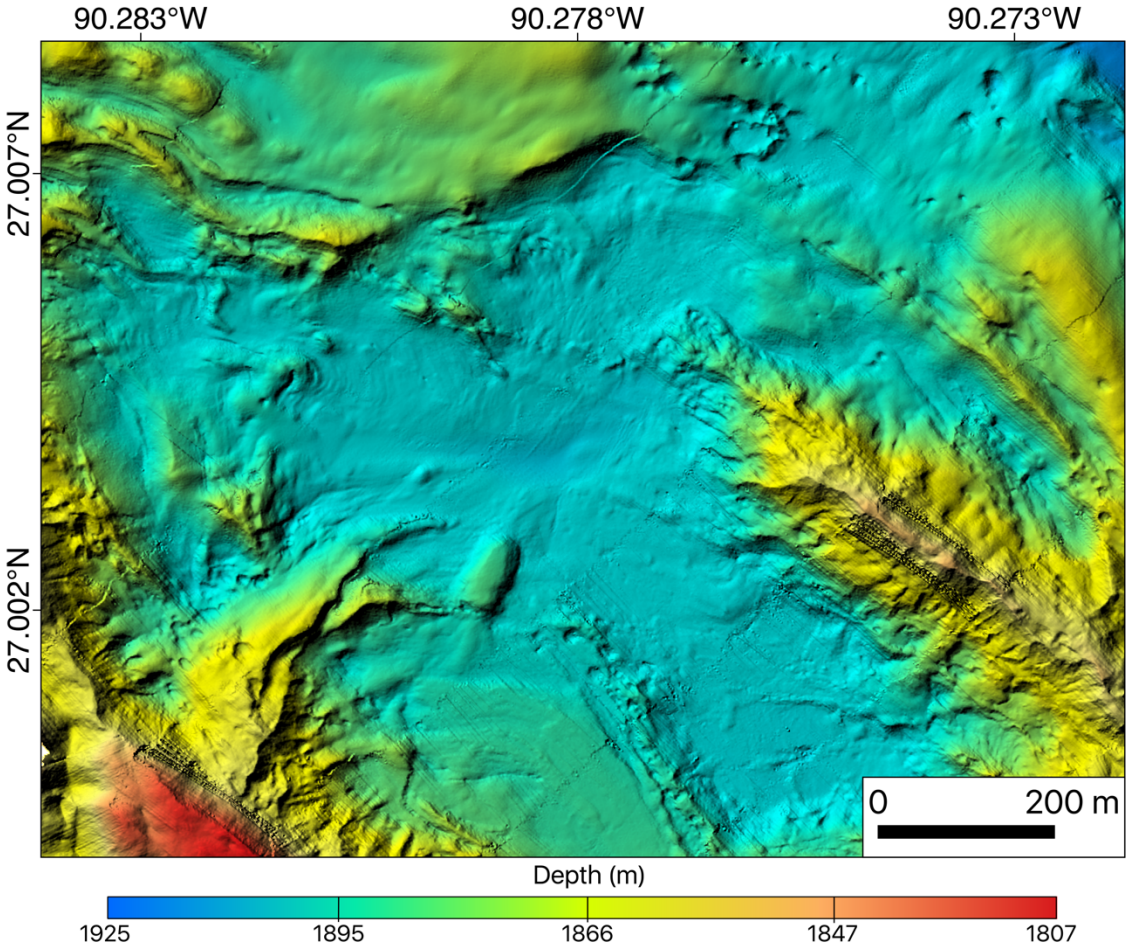

Figure A21-3 Zoomed perspective of lower survey area.

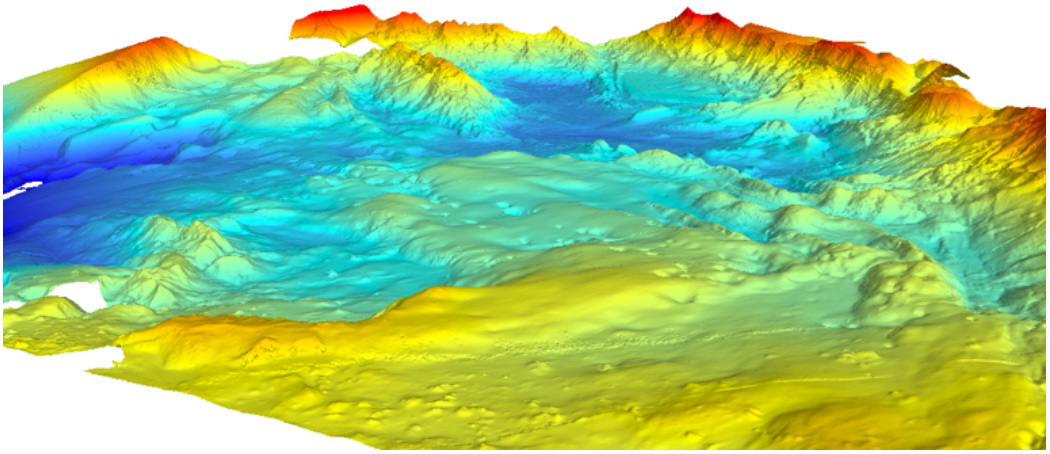

Figure A21-4 3D perspective of Sentry 315 from the north.

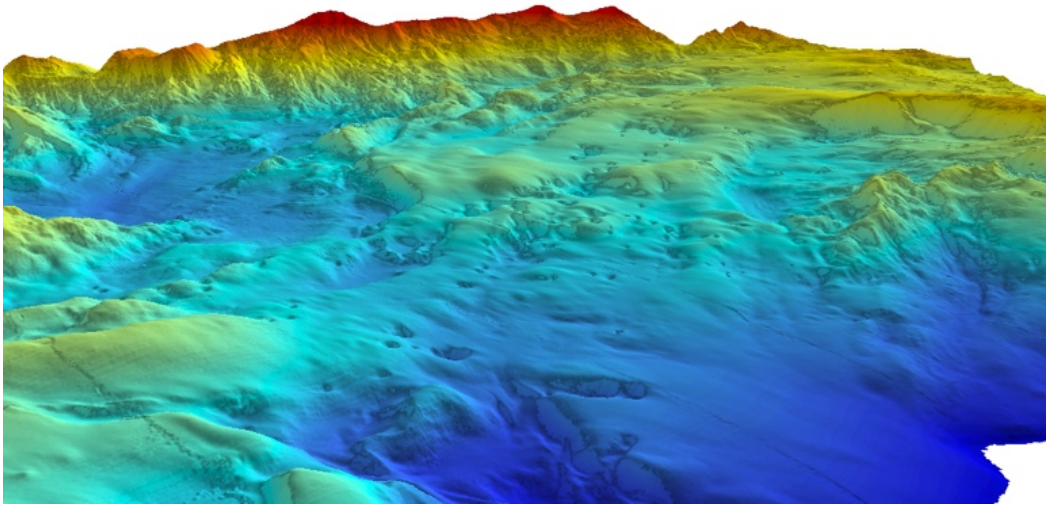

Figure A21-5: 3D perspective of Sentry 315 from the southeast.

Sentry 317

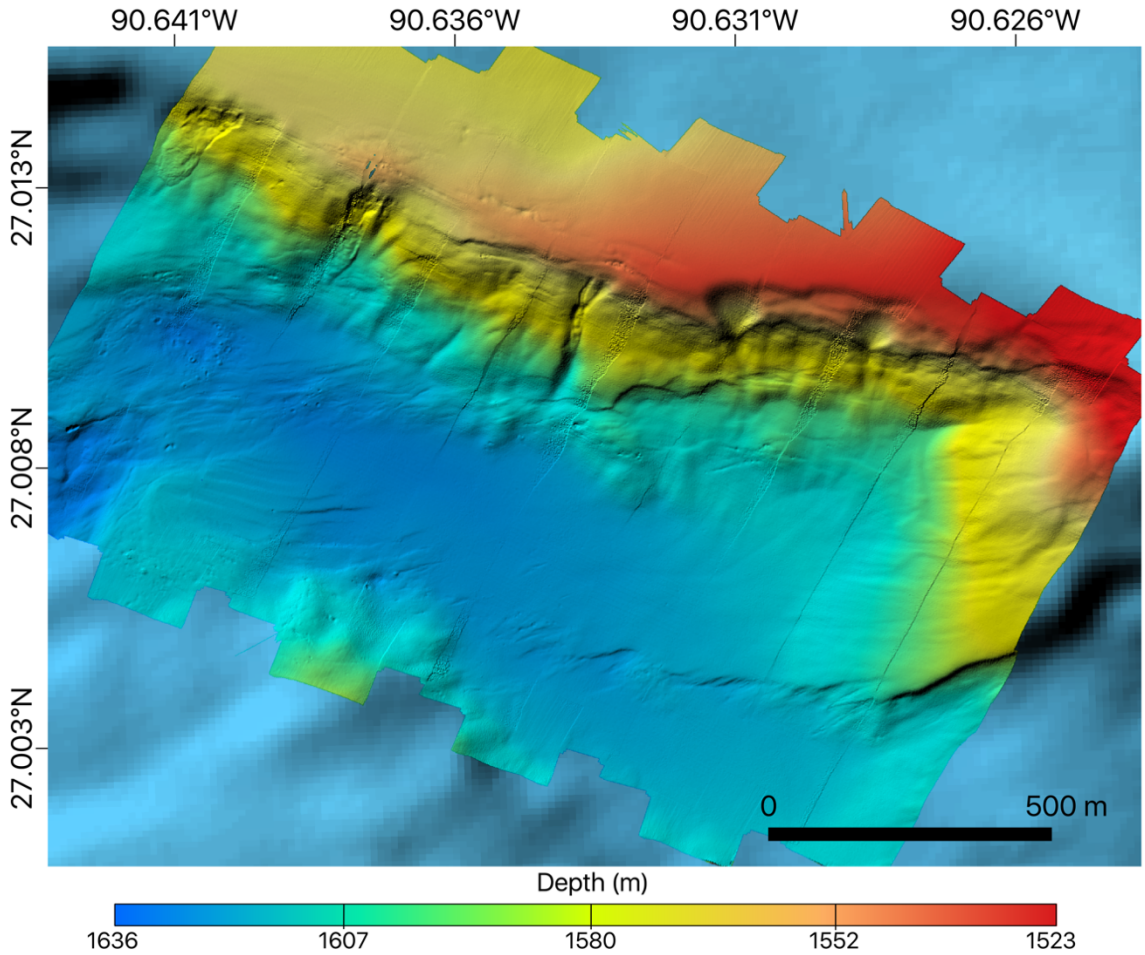

Figure A22-1: An overview of the Sentry 317 survey area.

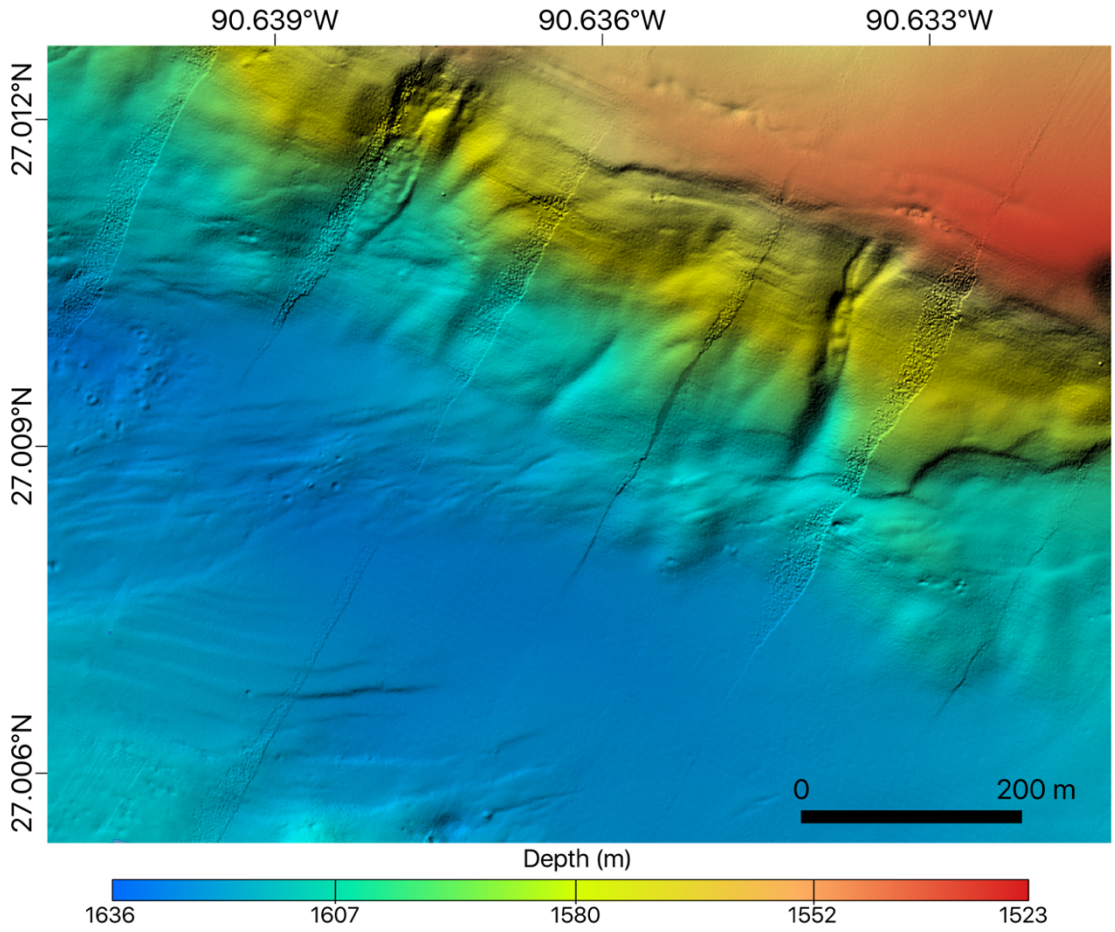

Figure A22-2: A zoomed in perspective of Sentry 317

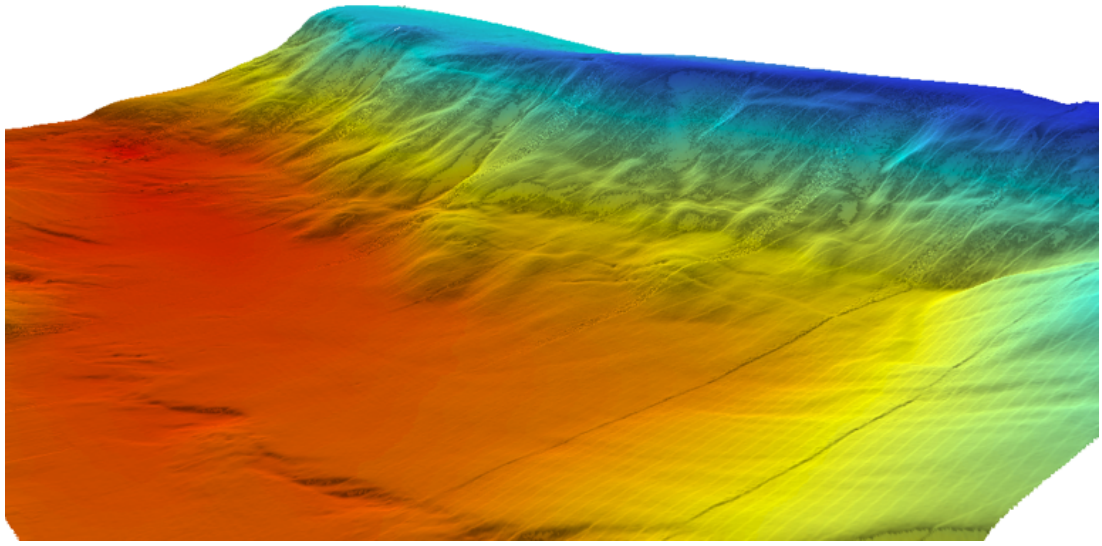

Figure A22-3: A 3D perspective from the east of Sentry 315.

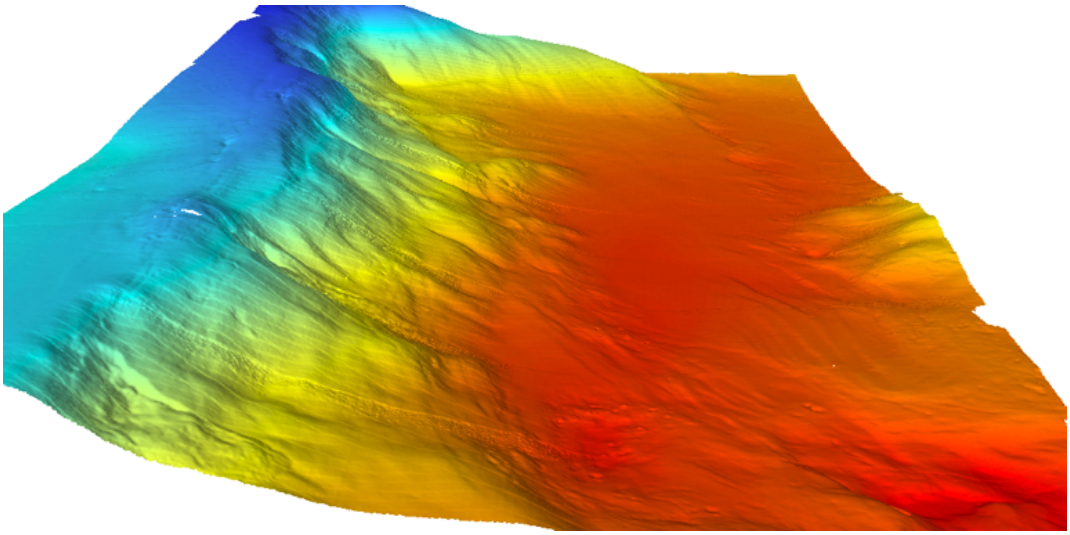

Figure A22-4: A 3D perspective from the northwest of Sentry 315.